DC Solid-State Circuit Breaker Reliability under Ship Power System Stresses

MSc Thesis Report

Y.H.W. Lee BSc

August 2025

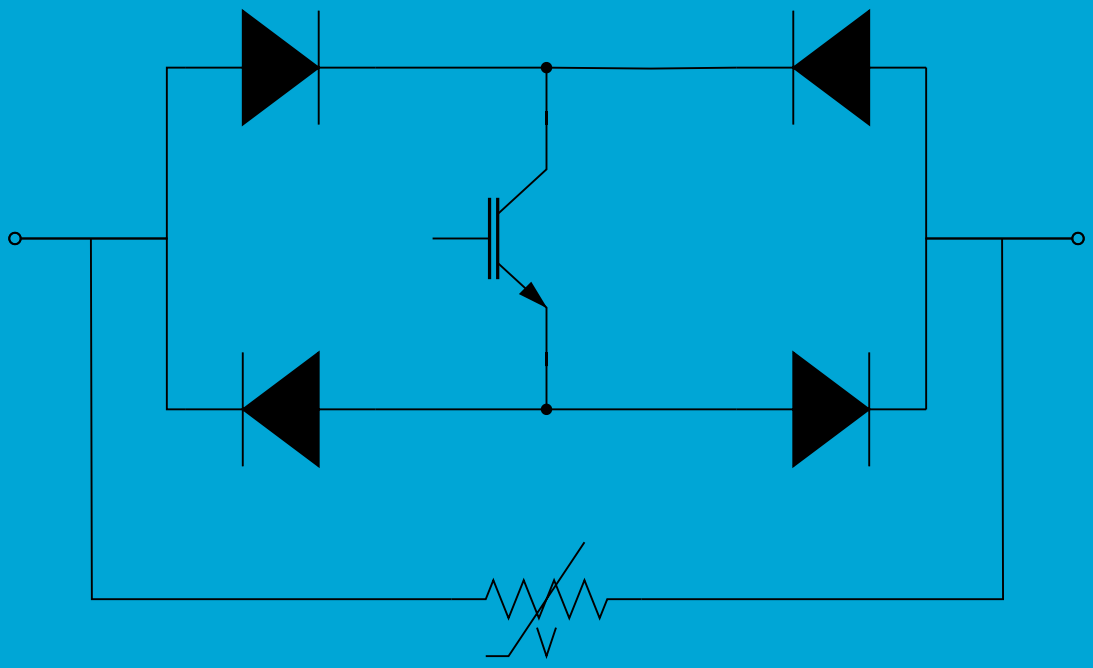

TU Delft Delft University of Technology

DCE&S DC systems, Energy conversion & Storage

DAMEN

DC Solid-State Circuit Breaker Reliability under Ship Power System Stresses

Thesis

by

Y.H.W. Lee BSc 5066247

Delft University of Technology

Faculty of Electrical Engineering,
Mathematics and Computer Science

Submitted in partial fulfilment of the requirements for the degree of

Master of Science

In Electrical Engineering

To be defended in public on 27 Aug 2025 at 10:00 AM

Supervisors:	Prof. dr. ir. P. Bauer	TU Delft, DCE&S
	Dr. ir. A. Shekhar	TU Delft, DCE&S
	Ir. R.P.J. van der Sande	TU Delft, DCE&S
	Dr. E. Sciberras	Damen RD&I B.V.
Thesis committee:	Dr. ir. J. Dong	TU Delft, DCE&S
	Dr. ir. H. Polinder	TU Delft, Transport Engineering and Logistics
	Dr. ir. A. Shekhar	TU Delft, DCE&S

An electronic version of this thesis is available at http://repository.tudelft.nl/.

Abstract

Modern DC power systems consist of a large number of power electronic converters and associated equipment. On a ship, this power system is typically divided into two identical parts on the port and starboard sides. These duplicated power systems are often isolated from each other to prevent a fault on one side from propagating to the other side and affecting the entire system, avoiding a total blackout on the ship. A major drawback of this two-split configuration, though, is that it is impossible to share power between both sides, reducing the functionality of the system. Therefore, to connect both sides while maintaining the safety of an isolated system, a solid-state circuit breaker (SSCB) can be used, which is reusable, unlike a fuse, and is able to interrupt the current much faster than a standard mechanical circuit breaker. However, due to the relative novelty of this component, the impact of mission profile variation and electrical disturbance on the SSCB lifetime is unknown.

To obtain the SSCB lifetime, mission profile analysis was performed, resulting in a lifetime as a consequence of wear-out failure mechanisms due to thermomechanical fatigue that would be used as the base case. Based on the mission profile, an SSCB model was designed following considerations for: Current interrupter topology, rated voltage/current of the components, peak voltage/current of the components, voltage clamping circuit, and the cooling. After choosing suitable components, their junction temperature profiles were obtained via iterative calculations with the power loss and the junction temperature using a Cauer model without thermal capacitance. With the rainflow counting algorithm, information regarding the cycle count, temperature swing, mean temperature, minimum temperature and the power-on-time per class was obtained. These were used in the CIPS with correction lifetime model, which obtained the cycle-to-failure of each relevant component. Transforming them into a reliability curve per component and multiplying them together resulted in the reliability curve of the SSCB. To estimate the impact on the lifetime of the electrical noise through the SSCB in comparison to the mission profile, a dynamic model was designed to take thermal capacitance into account, unlike the iterative model.

To quantify the impact of different stressors on the SSCB lifetime, changes in the mission profile, SSCB configuration and operational parameters compared to the base case are made. It was seen that the charging current, corresponding to changes in the maximum stress within the mission profile, has the most significant impact on the SSCB lifetime, while having a relatively minor drawback of a varying charging period. Bi-directional charging and changes in the coolant temperature were shown to have a relatively low impact on the lifetime. Load sharing between parallel components in a module significantly increased the lifetime, but at a cost of practically investing in a second SSCB. Concerning the impact of noise on SSCB lifetime with respect to the damage done by the mission profile, it can be concluded that high-frequency noise, such as the common-mode and differential-mode noise, has a negligible effect on the lifetime of the SSCB when solely focusing on wear-out mechanisms due to thermomechanical fatigue.

Acknowledgements

I would first like to offer my gratitude to my TU Delft supervisors, Dr. ir. Aditya Shekhar and Ir. R. van der Sande for their guidance and the meaningful discussions throughout the entire master's thesis. I will always keep the importance of critical thinking in mind, and try to keep improving upon it in the future.

Next, I would like to thank my supervisor at Damen Shipyards, Dr. Edward Sciberras, for providing me with a vast amount of ship knowledge and for his great assistance in technical matters. I would also like to thank Ir. Peter Rampen and Damen Shipyards B.V. for accepting me to do an internship and this master's thesis, which resulted in an entertaining year where I have learned a lot.

Furthermore, I want to thank my family for their unconditional support throughout this thesis and my entire study. Their support has helped me to keep motivated.

Lastly, I want to thank all my friends that I have met during my academic journey for making this part of my life a memorable one.

Wesmond Lee
Delft, 27/08/2025

Contents

List of Figures

List of Tables

List of Abbreviations

AC Alternating Current

CM Common-Mode

CTE Coefficient of Thermal Expansion

DC Direct Current

DCB Direct Copper Bonded

DM Differential-Mode

GTO Gate Turn-Off Thyristor

IGBT Insulated-gate Bipolar Transistor

MOV Metal-Oxide Varistor

PMF Probability Mass Function

RB-IGCT Reverse Blocking - Integrated Gate-Commutated Thyristor

SPS Ship Power System

SSCB Solid-State Circuit Breaker

TVS Transient-Voltage-Suppressing

Chapter 1

Introduction

Modern DC power systems consist of a large number of power electronic converters and associated equipment. These interconnected systems form the necessary backbone for energy exchange and conversion between generation, storage and consumption and are thus essential parts of the DC power system. On a ship, this power system is typically divided into two identical parts on the port and starboard sides. These duplicated power systems are often isolated from each other to prevent a fault on one side from propagating to the other side and affecting the entire system, avoiding a total blackout on the ship.

A major drawback of this two-split configuration, though, is that it is impossible to share power between both sides, reducing the functionality of the system. Therefore, to connect both sides while maintaining the safety of an isolated system, a solid-state circuit breaker (SSCB) can be used, which is reusable, unlike a fuse, and is able to interrupt the current much faster than a standard mechanical circuit breaker. However, due to the relative novelty of this component, the impact of mission profile variation and electrical disturbance on the SSCB lifetime is unknown.

With the SSCB constantly exposed to sudden electrical overstresses, it can cause the components to break down prematurely due to random chance failures. However, when they operate under rated conditions with a fixed daily mission profile, the failure mechanisms that are most frequently observed in power devices are due to thermomechanical fatigue stress in the device packaging caused by temperature swings that the device endures during its lifetime [9]. These eventually cause wear-out failure mechanisms such as bond wire lift-off and solder cracks.

In the case of high-frequency disturbances in the power system (in the kHz range), it is unclear whether the consequent thermal fluctuations would have a noticeable impact on the wear-out of the device.

Therefore, the main scope of this thesis is to quantify the thermal impact of a mission profile and electrical disturbances seen on DC shipboard power systems on the reliability of solid-state circuit breakers used as a DC bus tie.

1.1 Research objective

This thesis aims to give an insight into the sensitivity of solid-state circuit breaker reliability when the mission profile is altered, and due to high-frequency disturbances such as Common-Mode (CM) and Differential-Mode (DM) noise present on the DC bus. Therefore, the main research question is:

What is the impact of changes in mission profile and CM/DM noise on the lifetime of a solid-state circuit breaker as a bus tie in a DC ship power system?

To answer this research question, it is divided into several sub-research questions:

1. *Which considerations should be taken into account when designing the SSCB?*

To obtain results that are representative of real applications, a model representing the physical structure of the SSCB has to be made. To do so, suitable topologies and components have to be selected based on a required power rating and given use case. Once obtained, the next question can be answered:

2. *How to obtain a lifetime estimation of the SSCB as a consequence of thermal fatigue?*

To model the impact that thermal fluctuations have on component lifetime, a thermal profile is derived from which the number of thermal cycles can be counted. Using existing lifetime models to analyse a specific mission profile with ideal direct current (DC), the reliability is then obtained. However, not all ships have the same mission profile, SSCB configuration and operational parameters. Such changes will have a certain impact on the SSCB lifetime; thus, the following research question is stated as:

3. *What is the sensitivity of SSCB lifetime due to changes in the mission profile, SSCB configuration and operational parameters?*

By applying different changes compared to the base case separately, the individual effects of each change can be studied to observe their consequences on the lifetime. Still, it is unknown whether high-frequency noise present in the power system will also contribute to the degradation of the SSCB, leading to the last research question:

4. *To what extent does electrical noise have an impact on the solid state circuit breaker reliability compared to the mission profile?*

1.2 Thesis outline

To answer the research questions, this thesis is composed of seven chapters defined as follows:

Chapter 2: Literature review
This chapter is divided into three sections. First, it gives an overview of the current state of solid-state circuit breaker technology, providing information about topologies and the semiconductors available. The second part explains the types of failures electrical components endure and presents models to estimate their lifetimes per type of failure. The third part briefly explains typical electrical disturbances seen on ship power systems.

Chapter 3: SSCB modelling
Explains the base use case for which the SSCB should be designed. Then defines the factors that should be taken into account when sizing the components in the SSCB for the aforementioned use case, after which suitable commercially available components are selected.

Chapter 4: Reliability modelling
Defines the steps taken to obtain the estimated lifetime curve as a consequence of one type of failure, namely wear-out failures. Furthermore, it provides design choices for the used lifetime models and justifies parameter selections.

Chapter 5: Sensitivity analysis
Presents the effects on SSCB lifetime due to changes in mission profile, additional components in parallel, and different operational conditions. These results are then compared with the base reliability model to quantify the impact each adjustment has.

Chapter 6: Electrical disturbances
Investigates the impact that electrical disturbances, such as CM and DM noise current, have on the reliability of the SSCB. By sweeping through the amplitude and frequency of noise current, a graph is made estimating the impact on the lifetime compared to the base case.

Chapter 7: Conclusion & Future work
The final chapter presents the conclusions of the research project, as well as recommendations for future work to enhance and extend this research.

Chapter 2

Literature Review

2.1 Introduction

This literature review aims to present the current knowledge surrounding the Direct Current Solid-State Circuit Breaker (DC-SSCB), and, where applicable, with emphasis on usage as a bus-tie in a DC ship power system. It focuses on components most prone to failure and modelling techniques used to estimate the device lifetime. In this literature review, first, the semiconductor technologies, SSCB topologies, and voltage clamping circuits are discussed. Then, the functioning of reliability estimation methods for random failures: MIL-HDBK-217, IEC 61709, and FIDES is explained. Next, the consequences of wear-out failures due to thermomechanical fatigue and how to model them using lifetime estimation models are discussed. Lastly, the possible effects on the reliability of high-frequency disturbances such as the common-mode (CM) and differential-mode (DM) noise from a ship power system are reviewed.

2.2 Solid-state circuit breaker

To give an insight into the current technologies available for a solid-state circuit breaker, this section aims to give an overview of the types of switches and topologies used in the current interrupter. Furthermore, different types of voltage clamping circuits with their own strengths and drawbacks are presented, which is useful to select optimal components for the current interrupter.

2.2.1 Layout of SSCB

A typical SSCB consists of the following key components [1]:

- Current interrupter: A unidirectional or bidirectional circuit using switches which block the current as fast as possible in case a fault seen by the SSCB occurs.
- Cooling: Keeps the current interrupter within the operating temperature window.
- Voltage clamping circuit: Used to absorb the excessive energy from system inductances during fault interruption.
- Trip sensor: Detects whether a fault current is flowing through the SSCB.
- Gate driver: Controls the current interrupter.
- Mechanical switch: Used to fully disconnect the SSCB after fault current has been cleared, isolating both sides of the SPS from each other.

The interconnection between these components is described in Figure 2.1.

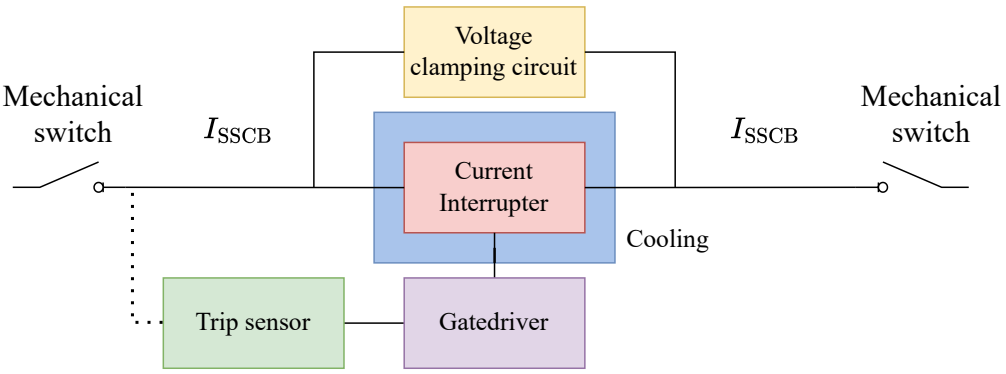

Figure 2.1: Key components typical SSCB [1]

2.2.2 Current interrupter switch

The power semiconductor switch, as part of the current interrupter, is the main component of the SSCB. The component should cut off the current as fast as possible when a fault occurs, and it is the component through which the main power flows during regular operation. In [1], a summary of the power semiconductors used for SSCBs is given. It can be noted that the higher the power rating, the more bipolar devices are used, such as the insulated-gate bipolar transistor (IGBT), the integrated gate-commutated thyristor (IGCT) and the gate turn-off thyristor (GTO). These devices use both the minority and majority carriers as charge carriers during the on-state (conductivity modulation), leading to higher on-state conductivity and, thus, fewer conduction losses. To enable reverse-voltage blocking capabilities, a diode has to be inserted in series with the bipolar device. Except for the special type of IGCT called the Reverse Blocking IGCT (RB-IGCT), which already has built-in reverse-blocking capabilities due to an additional p^- junction in its structure compared to the IGCT [10].

2.2.3 Current interrupter topology

The authors of [1] give a review of the many topologies used for the current interrupter in the SSCB. In this case, the focus is on fully controlled switches due to the simple topologies that can be used to block a large range of voltages and currents. From Figure 2.2, it is seen that these switches are placed in anti-parallel, anti-series, or rectifier-assisted topologies, depending on the semiconductor used. These configurations enable the bidirectional breaking of the current, which will prove to be useful for power sharing when used as a link between power systems.

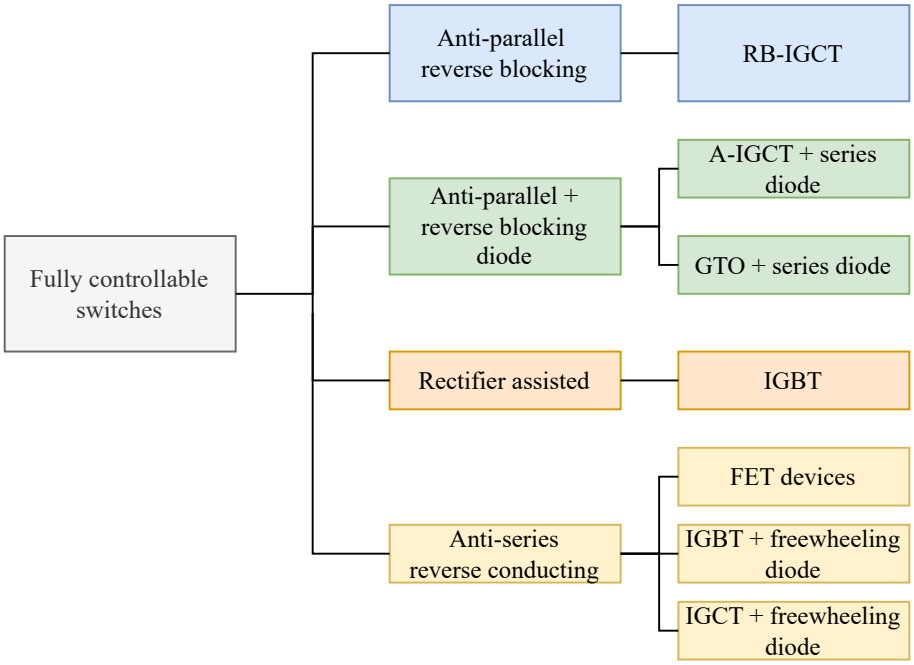

Figure 2.2: SSCB topologies tree for the fully controlled switches and the typical switches per topology [1]

Experimentally validated topologies are summarised in [11] and [1]. From it, the following three are highlighted:

1. Anti-parallel RB-IGCT [12]: An option is using two reverse-blocking IGCTs in anti-parallel configuration to enable bi-directional functionality. IGCTs have lower conduction losses than IGBTs [13] because they conduct like a thyristor in the on-state. Next to that, it has an IGBT's hard switching turn-off capabilities, making it able to withstand switching at high currents. However, a standard IGCT, without an additional diode in series, can only block current in a forward direction. An RB-IGCT solves that issue by having inherent diode properties in a single device. This reduces the number of components needed in the topologies, reducing failure probability. To reduce the voltage overshoots, a metal-oxide varistor (MOV) is placed in parallel with the RB-IGCT as a voltage clamp, resulting in a topology like Figure 2.3a. To increase the nominal current handling of the SSCB, a second branch can be added in parallel without creating instability [13].
   However, the main drawback of using RB-IGCTs is that, due to the novelty of the device (first introduction by ABB in 2015 [14]), not many variations in power rating are commercially available yet.

2. Rectifier assisted IGBT [15]: This second type of SSCB uses a singular or multiple IGBTs in parallel, dependent on the current rating, in conjunction with a full bridge rectifier to enable bi-directionality. The main benefit of this topology is that it uses common components and that it is a simple topology that can easily be expanded to increase the current rating. However, the main drawback is that the current has to flow through at least 3 components at all times, namely two diodes and one IGBT, meaning more components are subjected to thermal stresses compared to the RB-IGCT topology.

3. Anti-series IGBT [16]: This topology is also based on reverse-conducting IGBTs with a freewheeling diode. A choke is placed between the IGBTs to limit the current during an event of a short-circuit and to measure whether a fault has occurred to trigger the switch. This topology of-

fers a good balance between conductivity efficiency due to the current having to pass just an IGBT and a diode to flow, and affordability with the usage of two simple IGBTs.

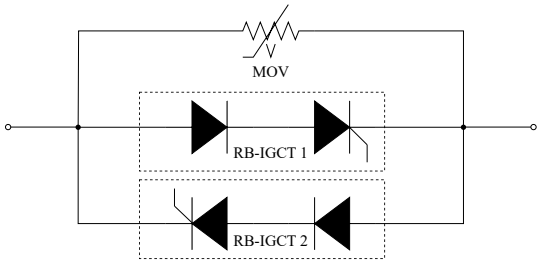

(a) Anti-parallel RB-IGCT SSCB topology

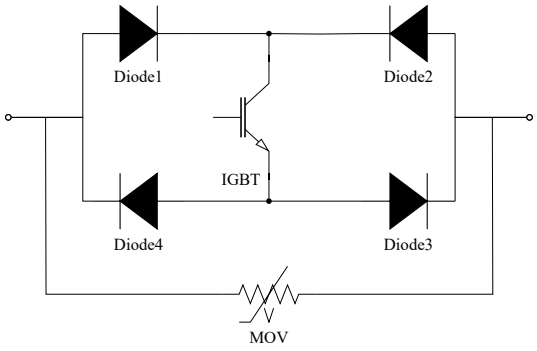

(b) Rectifier assisted IGBT topology

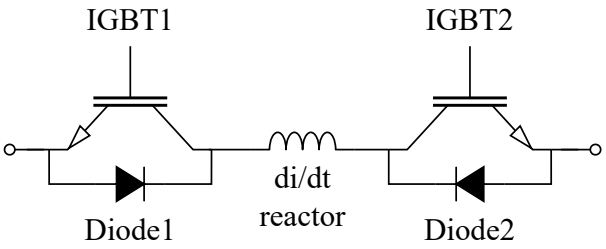

(c) Anti-series IGBT topology

Figure 2.3: Simplified topologies of selected SSCBs

In an application where the SSCB is used as a bus tie between two DC buses and is expected to be opened only in a rare event of a fault, the main focus should be on conduction efficiency. Moreover, to be used in cramped switchboard rooms of ships, the size and number of components also play a role. However, it is to be noted that it is unclear how changes in topologies, e.g., using a different semiconductor in the same topology or putting separate SSCBs in parallel to increase the nominal current, might affect the performance of each individual component. Further research has to be done to ensure the actual optimised topology is chosen for each individual application.

2.2.4 Voltage clamping circuit

The last part that should be investigated is the voltage clamping circuit across the current interruption part of the SSCB. Following [1], three main types of clamping circuits exist. The first are RC(D) snubbers, the second consists of metal-oxide varistors (MOV), and the final one uses transient-voltage-suppressing (TVS) diodes. This voltage clamping circuit must prevent the IGBT from reaching its maximum rated peak voltage during turn-off by absorbing the energy from parasitic (or externally inserted) inductances and releasing it back into the power system gradually. Each voltage clamping circuit will clamp the maximum voltage at a different level. Nominally, the TVS diode will clamp the voltage at the lowest level of around 1.5 times its rated nominal voltage, the RC(D) will clamp it at 1.75 times nominal voltage, and the MOV generally around twice its rated nominal voltage [1].

RC(D) snubber

The RC or RCD snubber consists of a resistor and a capacitor in series, and optionally a diode across the resistor. After turning off the IGBT during a fault, the capacitor in the snubber will absorb the energy and

release it back into the power system. However, doing so will result in electrical oscillations in the system due to resonance between the inductance and the capacitance. To combat this, a snubber resistor is placed in series with the capacitor as a damper. The bigger the resistor, the faster the absorbed energy from the capacitor is dissipated into it. A drawback, however, is that during turn-off, the redirected current from the switch to the snubber must pass through the snubber resistor, which can counterproductively increase the voltage across the IGBT. To solve this, a diode can be placed across the resistor to give the current a seemingly resistance-less path to the capacitor, while maintaining the dampening effect of it during the release of the absorbed energy. A major drawback of this type of snubber, though, is that it only works unidirectionally, meaning that it is unsuitable to be used in a bidirectional SSCB functioning as a bus-tie.

MOV

The second option would be to use a metal-oxide varistor. This is a bidirectional component which functions as a nonlinear resistor. [17] gives an in-depth explanation of the physics of the MOV. It consists of many small metal grains, mostly zinc oxide (ZnO), surrounded by intergranular material. This material has insulating properties under nominal voltage, creating a boundary through which very little current can pass. This means that the MOV behaves as an open circuit during standard operation under nominal voltage. When the voltage passes a threshold during the opening of the current interrupter, the intergranular boundary breaks down, similarly to a p-n junction of a diode while forward biased. Consequently, its resistance decreased, and current is able to pass through it, dissipating the energy from the system's inductance. It stays conducting until the voltage eventually drops below the threshold again and returns to an open-circuit state.

A drawback of the MOV is its limited lifetime due to the degradation of the insulating material inside each time the clamping circuit is used. However, when used as part of an SSCB as a bus tie on a ship power system, emergency turn-offs are a rare case, which means that the MOV would not have to be stressed often, making this drawback acceptable.

TVS

Lastly, there is the transient-voltage-suppressing (TVS) diode. This diode behaves similarly to the MOV, but has a faster response time at a higher cost [1]. Whereas regular diodes would be destroyed by avalanche breakdown if the blocking voltage exceeded their rating, the TVS diodes are specifically designed to make use of that overvoltage (to a certain degree) and let current flow in a reverse-bias direction, after which they return to their regular reverse blocking state.

2.3 Reliability Estimation

This section aims to find the components in devices most prone to failure. Next, it summarises the existing reliability modelling techniques for the random chance failures. Furthermore, the cause of wear-out failures is explained, and the models to estimate the lifetime of the components as a consequence of thermal-mechanical fatigue are presented.

2.3.1 Components prone to failure

From a 2011 survey [18], it can be noted that the most vulnerable components are the power semiconductors in a device, followed by capacitors, gate drives, connectors, inductors and resistors. Since no capacitors are present in the highlighted SSCB topologies, only the power semiconductors inside the current interrupter are considered in this reliability research. Considering the power from the power system to the SSCB will flow through them, they are the most susceptible to main failure stressors such as electrical loading and temperature cycling [3]. On the other hand, the gate driver does not experience the same electrical loading nor temperature cycling as it is being powered by an auxiliary power supply

and is expected to always keep the switch in the on-state unless a fault occurs. Thus, together with the low failure probabilities of the connector, inductor and resistor [18], none of the components except the power semiconductors are taken into account for reliability research.

Although there is always a possibility of some failure due to human and software errors, this literature review focuses on random hardware failures, which can be divided into constant failures, wear-out failures, and early "infant mortality" failures due to fabrication faults. Together, these failures produce the characteristic "bath-tub" shown in Figure A.1. However, the latter is omitted, since it is assumed the components are past their infant mortality phase.

2.3.2 Random chance failures

The failure probability of random chance failures is assumed to be constant throughout the entire lifetime of the component. Random chance failures are described as catastrophic failures, mostly due to high bursts of temperature, voltage, or current causing extrinsic faults such as break-downs and bond wire ruptures [9] [19] [20]. The failure mechanisms for the power device can be found in Table A.1. Different methods have been devised to model random chance failures, and the most relevant ones are highlighted in the following sections.

MIL-HDBK-217

First is the MIL-HDBK-217. This reliability prediction method is the oldest and was devised by the United States military to estimate the lifetime of standard components. The main principle of this method is to take an empirically derived base failure rate of a component and multiply it by all kinds of different stress factors to obtain the failure rate (in failures/10^6 hours). For a low frequency($<$200MHz), bipolar transistor such as the IGBT, it is derived as (2.1) [21]

$$\lambda_{\text{IGBT}} = \lambda_{\text{b}} \cdot \pi_{\text{T}} \cdot \pi_{\text{A}} \cdot \pi_{\text{R}} \cdot \pi_{\text{S}} \cdot \pi_{\text{Q}} \cdot \pi_{\text{E}} \tag{2.1}$$

with λ_{b} the base failure rate of the component, π_{T} the temperature factor, π_{A} the application factor, π_{R} the power rating factor, π_{S} the voltage stress factor, π_{E} the environment factor and lastly π_{Q} as the quality factor. These values are not calculated, but selected via look-up tables in the MIL-HDBK-217. Although this method is often used for simplicity, the main drawback is that the component is assumed to operate continuously with the same constant stress values. It does not consider the thermal cycling of the component due to the mission profile. Next to that, it has not been updated since 1995, and with the rapid advancements in electrical technology, it gives an underestimation of the component lifetime [22].

IEC 61709

Due to the inaccuracy of the MIL-HDBK-217, updated versions with adjusted handbook data and methodologies are devised by companies such as the Telcordia SR-332 (by Telcordia) and SN 29500 (by Siemens). Although these methods give a more representative failure rate estimation of a component compared to the MIL [23] [24], the problem of not taking the mission profile and thus the thermal cycling into account persists, which makes the method unsuitable to be used in operations with high fluctuations in power or thermal conditions. Thus, the International Electrotechnical Commission (IEC) released IEC TR-62380 in 2006, which considers failure mechanisms for failure rate prediction throughout an annual mission profile [25]. Later, in 2017, the provided data and the method in IEC TR-62380 were updated and replaced by the IEC 61709, which uses reference conditions and operating conditions derived from a mission profile to estimate a component's failure rate better. The main principle is still the same as the MIL. A reference failure from the component manufacturer or field data from the IEC datasheets "IEC 60300-3-3" and "IEC 60300-3-5" is used as the base failure rate and multiplied by factors that will affect the reliability of the component. The main formula is described as [26]:

$$\lambda_{\text{61709-2017}} = \lambda_{\text{ref}} \cdot \pi_{\text{U}} \cdot \pi_{\text{T}} \cdot \pi_{\text{I}} \cdot \pi_{\text{E}} \cdot \pi_{\text{S}} \cdot \pi_{\text{ES}} \tag{2.2}$$

With voltage dependence factor π_{U}:

$$\pi_{\mathrm{U}} = \exp\left\{C_3 \cdot \left[\left(\frac{U_{\mathrm{op}}}{U_{\mathrm{rat}}}\right)^{C_2} - \left(\frac{U_{\mathrm{ref}}}{U_{\mathrm{rat}}}\right)^{C_2}\right]\right\} \tag{2.3}$$

current dependence factor π_{I}:

$$\pi_{\mathrm{I}} = \exp\left\{C_4 \cdot \left[\left(\frac{I_{\mathrm{op}}}{I_{\mathrm{rat}}}\right)^{C_5} - \left(\frac{I_{\mathrm{ref}}}{I_{\mathrm{rat}}}\right)^{C_5}\right]\right\} \tag{2.4}$$

and temperature dependence factor π_{T}:

$$\pi_{\mathrm{T}} = \exp\left[\frac{E_a}{k_0} \cdot \left(\frac{1}{T_{\mathrm{ref}}} - \frac{1}{T_{\mathrm{op}}}\right)\right] \tag{2.5}$$

The C_x values are constants depending on the component obtained from data sheets. π_{E} is the environmental application factor, π_{S} is the switching rate dependence factor and lastly π_{ES} is the electrical stress dependence factor. In the case of a bipolar power semiconductor, such as the IGBT, only the temperature dependence factor is deemed important enough to be considered according to the method [26].

$$\lambda_{\mathrm{IGBT}} = \lambda_{\mathrm{ref}} \cdot \pi_{\mathrm{T}} \tag{2.6}$$

When the calculations are repeated for different levels of stress in the mission profile, the weighted average can be taken of the different failure rates with

$$\lambda_{\mathrm{as}} = \frac{1}{t_{\mathrm{f}} + \sum_{i=1}^{N} t_{\mathrm{p,i}} + t_{\mathrm{d}}} \left(t_{\mathrm{f}}\lambda_{\mathrm{f}} + \sum_{i=1}^{N} t_{\mathrm{p,i}}\lambda_{\mathrm{p,i}} + t_{\mathrm{d}}\lambda_{\mathrm{d}}\right) \tag{2.7}$$

with

$$\lambda_{\mathrm{d}} = \rho \cdot \lambda_{\mathrm{f}} \tag{2.8}$$

where t is time, λ is the failure rate, subscript f, p, d representing full-stress, partial stress, and dormant state, respectively, N is the number of partial stress states, and ρ a factor to determine failure rate when in a dormant state; which is stated as a factor of 0.1.

FIDES

The last option is called FIDES(2022). Compared to the IEC 61709, this method encapsulates more factors contributing to the random hardware failures and looks to model each individually rather than grouping them into one environmental factor [27]. Also, the difference in reliability between the solder joints and the case of an IGBT is modelled differently, thus trying to take the physics of failure into account. This is all done using data obtained from a more detailed mission profile. Next to the physical data, the effect on the component's reliability is considered based on the quality assurance (maintenance) factors Π_{PM} and the system developer's processes factors Π_{process}. Together they form the general formula in (2.9) [27]

$$\lambda = \lambda_{\mathrm{physical}} \cdot \Pi_{\mathrm{PM}} \cdot \Pi_{\mathrm{process}} \tag{2.9}$$

For a power IGBT, an extra Π_{PW} term representing an extra weight term to the manufacturing process is inserted with a default value of 10:

$$\lambda = \lambda_{\mathrm{physical}} \cdot \Pi_{\mathrm{PM}} \cdot \Pi_{\mathrm{PW}} \cdot \Pi_{\mathrm{process}} \tag{2.10}$$

with

$$\lambda_{\mathrm{physical}} = \sum_{i=1}^{Phases} \left(\frac{T_{\mathrm{phase}}}{T_{\mathrm{Total}}} \cdot \begin{pmatrix} \lambda_{0\mathrm{TH}} \cdot \Pi_{\mathrm{Thermal}} + \\ \lambda_{0\mathrm{TCCase}} \cdot \Pi_{\mathrm{TCyCase}} + \\ \lambda_{0\mathrm{TCSolderJoints}} \cdot \Pi_{\mathrm{TCySolderJoints}} + \\ \lambda_{0\mathrm{RH}} \cdot \Pi_{\mathrm{RH}} + \\ \lambda_{0\mathrm{Mech}} \cdot \Pi_{\mathrm{Mech}} \end{pmatrix} \cdot \Pi_{\mathrm{Induced}}\right)_{\mathrm{i}} \tag{2.11}$$

Each individual multiplier of the base λ values can be calculated by the calculations given in the FIDES guide.

However, research supported by NASA in 2023 [28] argues that the FIDES method is not physics of failure-based due to the lack of coverage of the geometry of the component as well as the failure modes, mechanisms, sites, and the eventual wear-out failures. Next, it argues that the values of the manufacturing factors and the process factors are too subjective while having a major impact on the result, which led to their dismissal of FIDES as a reliable failure estimation tool. On the other hand, it was already stated in the FIDES manual that it is assumed that the component remains in its useful lifetime, thus creating a constant failure rate. FIDES and other constant failure estimation tools should thus not be the sole measure of component reliability, but wear-out failures should be modelled separately.

Comparison

Summarised in the following table is the comparison between the most common constant failure models with their relation to mission profile, physics of failure, complexity and general target audience:

Table 2.1: Comparison of prediction methods for constant failure rate

Prediction method	**Takes mission profile into account**	**Takes physics of failure into account**	**Complexity**	**Use-case**	**Requirement**
MIL-HDBK-217	No	No	Low	Rough but simple lifetime estimation	Stable environmental and power conditions
Telcordia SR-332	No	No	Low	Telecom	Stable environmental and power conditions
SN 29500	No	No	Low	Industrial applications	Stable environmental and power conditions
IEC 61709	Yes	No	Mid	Components with varying operations	Mission profile of component
FIDES	Yes	Yes[1]	High	Extensive failure rate estimation	Mission profile of component, manufacturing data

[1] Dismissed by NASA [28]

2.3.3 Wear-out failures

Wear-out failures are a type of failure whose likelihood increases as a device undergoes repeated cycles of operation. To understand why this happens, a cross-section of a generic power device is shown in Figure 2.4.

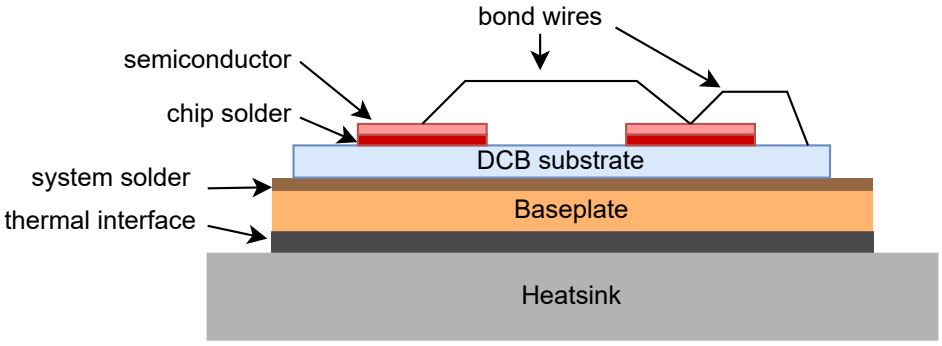

Figure 2.4: Cross-section of generic power device

A power device is made up of multiple layers: First are the semiconductors connected by bondwires, attached on top of a Direct Copper Bonded (DCB) substrate by solder. This substrate is, in turn, soldered to the module baseplate, also called "case", for mechanical stability and efficient heat transfer to the final layer, which is the heatsink attached with a thermal interface in between, which is mostly thermal grease. When the semiconductors go through their power cycles, varying losses are incurred. These losses will result in temperature swings over the entire device. As the device heats and cools, the different layers and materials will expand and contract at varying rates, leading to mechanical stresses [9]. These can eventually cause wear-out failures such as cracks in the solder joints and bond wires or the bond wires lifting off the chip, as summarised in Table A.1.

Mission profile analysis is commonly used to model this failure, as described in [3]. It consists of three parts from which an eventual wear-out failure plot is created: Electrothermal stress mapping, power semiconductor reliability modelling, and converter reliability calculation. The required models to obtain the results of each of these parts are described in the following subsections.

Thermal model topologies

For electrothermal stress mapping, the thermal behaviour of power semiconductor devices can be predicted using thermal electrical analogies. By representing the thermal performance as an RC network, the thermal impedance can be expressed as a combination of resistance and capacitance [29]. These respectively represent the power loss converted into heat in Kelvin per Watt (K/W) and the thermal inertia of the power device in Joule per Kelvin (J/K), which result in the Cauer and Foster models as shown in Figure 2.5.

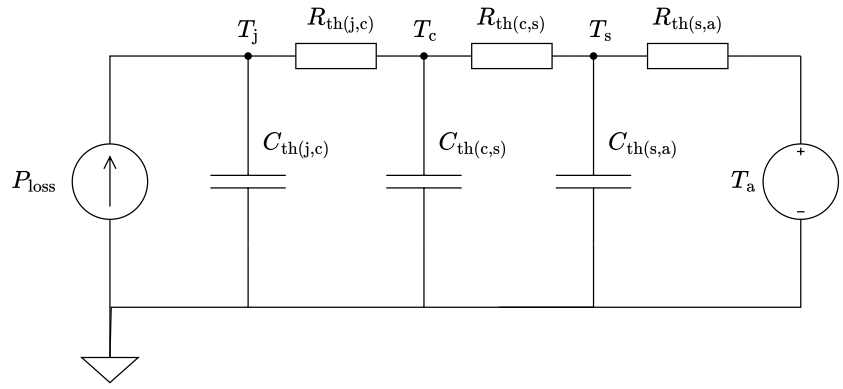

(a) Cauer thermal model

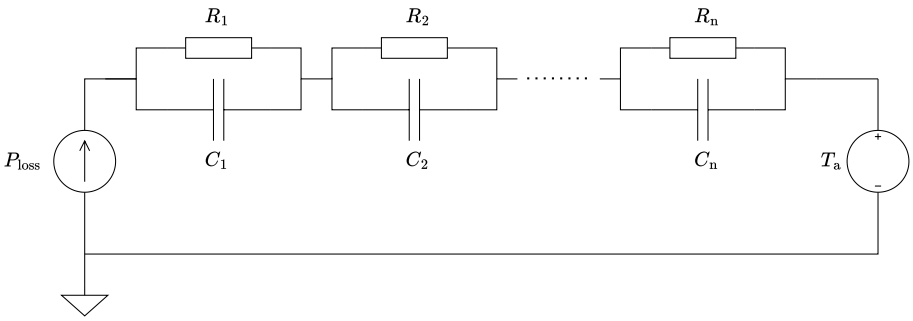

(b) Foster thermal model

Figure 2.5: Topologies of the Cauer and Foster thermal models. The Cauer thermal model represents the temperatures in the structure of the device, whereas the Foster thermal model represents the thermal transients.

Both thermal models look similar, but are used for different purposes. The Cauer thermal model has all the thermal resistances in series, like the Foster model. However, the thermal capacitances are connected directly to the thermal ground. This leads to the model being able to represent physical parts within the structure of the power device by assigning each RC pair to a layer in a power device as described in Figure 2.4. These layers are located between:

- semiconductor junction and the case, noted with subscript j,c
- case and (heat)sink, noted with subscript c,s
- (heat)sink and ambient(or coolant), noted with subscript s,a

If the complementary thermal resistances and capacitances between each internal layer of the device are known, the temperature of its internal parts can be calculated [29], which are the junction temperature (T_j), the case temperature (T_c) and the sink temperature (T_s). To calculate the junction temperature, the power loss is multiplied by the aforementioned thermal impedances and added to the ambient or coolant temperature, resulting in (2.12)

$$T_\mathrm{j} = P_\mathrm{loss}\left(Z_\mathrm{th(j,c)} + Z_\mathrm{th(c,s)} + Z_\mathrm{th(s,a)}\right) + T_\mathrm{a} \tag{2.12}$$

The Foster model has all thermal capacitances in series with each other, just like the series connection of the thermal resistance. This leads to the thermal components losing their physical meaning. Instead, they now represent the thermal transients of the whole device, or a part thereof. This means that the amount of power loss converted into heat has become a function of time. In datasheets, the time constant τ_i is

given per RC pair. The thermal impedance is then calculated as a multiplication of the given RC pair values as described by (2.13) [30].

$$Z_{\text{th(j, a)}}(t) = \sum_{i=1}^{n} R_{\text{i}} \left\{ 1 - \exp\left(\frac{-t}{\tau_{\text{i}}} \right) \right\} \tag{2.13}$$

To obtain the temperature rise over the entire Foster model, the power loss is convoluted by the derivative of the total impedance as described in (2.14) [29] and [30]

$$T_{\text{j}}(t) = T_{\text{a}}(t) + \left(P_{\text{loss}}(t) * \frac{d}{dt} Z_{\text{th(j, a)}}(t) \right) \tag{2.14}$$

Lifetime estimation

To obtain semiconductor reliability, the mission profile is first segmented into separate classes, from which the number of cycles per class is counted using a counting algorithm. Then, using a lifetime model, the number of cycles to failure per class is estimated. Different models exist to obtain this value; one of the most well-known ones is called LESIT [31] [7], described in (2.15)

$$N_{f_{\text{LESIT}}} = A \Delta T_{\text{j}}^{a} e^{\left(\frac{E_{\text{a}}}{k_{\text{B}} T_{\text{jmean}}} \right)} \tag{2.15}$$

The LESIT is a simple lifetime estimation, which only considers the peak-to-peak and average junction temperature in Kelvin. The activation energy E_{a}, Boltzmann's constant k_{b} and constant A are summarised in Table A.2. However, this simplicity leads to inaccurate estimations due to it not taking the heating time into account, which causes different types of failure modes. Low-magnitude thermal cycles at lower time scales tend to lead to bond wire fatigue, whereas high-magnitude temperature variation over longer periods of time stresses the solder joint of the base plate, leading to solder cracking [32]. Moreover, the period during which LESIT was developed used older chip packages from the 1990s, which have become outdated.

To update the lifetime estimation to more modern semiconductors, a second lifetime model called CIPS 08 was developed and published in 2008 by Bayerer [8], described by the following formula in (2.16)

$$N_{f_{\text{CIPS}}} = A \Delta T_{\text{j}}^{\beta_1} t_{on}^{\beta_3} I_{\text{bond}}^{\beta_4} V_{\text{class}}^{\beta_5} D_{\text{bond}}^{\beta_6} e^{\left(\frac{\beta_2}{T_{\text{min}}} \right)} \tag{2.16}$$

CIPS considers more variables, such as heating time t_{on}, bond wire current I_{bond}, voltage class V_{class} (blocking voltage/100 [33]), and bond wire diameter D_{bond}, with each its own constant beta values that skew their impact on the lifetime, which can be found in Table A.3. However, there is an inaccuracy in the lifetime estimation when the heating time is shorter than 0.1 or longer than 60 seconds. For short on-times (in ms), the CIPS method overestimates the cycles to failure because it does not take into account that the thermal inertia of the physical layers inside a semiconductor is similar to each other for on-times lower than 0.1 s [32]. This means that solder layers do not see significant enough temperature swings for different on-times in the milliseconds range to have significantly different cycles to failure. For longer on-times above 60 seconds, it is expected that all layers inside the component have reached steady-state temperature and thus should retain the same cycles to failure as the point in time at which they reached it [32]. The CIPS does not take this variable into account due to the t_{on}^{β} term, which drastically reduces in significance with a bigger t_{on} value and therefore underestimates the cycles to failure for long on-times. Thus, following [32], CIPS with correction is best suited for use cases involving longer periods of current conduction through the device, such as charging applications. Based on the heating time, the correct number of cycles until failure is calculated by applying a varying correction factor to the

calculated number of cycles if the on-time was 1.5s as described in (2.17):

$$\frac{N_{\mathrm{f}}(t_{on})}{N_{\mathrm{f}}(1.5)} = \begin{cases} 2.25 & t_{\mathrm{on}} \leq 0.1s \\ \left(\frac{t_{\mathrm{on}}}{1.5}\right)^{-0.3} & 0.1s \leq t_{\mathrm{on}} \leq 60s \\ 0.33 & t_{\mathrm{on}} \geq 60s \end{cases} \tag{2.17}$$

The LESIT and CIPS were both empirically derived from power cycling tests on semiconductors with an aluminium-oxide (Al_2O_3) substrate and a copper baseplate. However, as the voltage and current requirements of the semiconductors increased, they had to endure higher temperatures, which can cause the relatively soft copper to bend. A higher temperature swing also led to higher mismatch in expansion and contraction between the device layers, consequently leading to higher mechanical stresses and reducing their lifetimes [34]. Therefore, new materials had to be found to prevent the bending of the baseplate and with a better matching coefficient of thermal expansion (CTE) between the substrate and the baseplate. The selected materials were aluminium nitride (AlN) for the substrate and aluminium silicon carbide ($AlSiC$) for the baseplate, due to their matching CTE and the stiffness of ($AlSiC$) preventing bending, while maintaining a similar thermal performance as the copper baseplate [34]. The increase in the measured lifetime of modern high voltage IGBTs utilising the AlN substrate and $AlSiC$ baseplate compared to the estimations given by CIPS is shown to be consistently higher [35]. To give a lifetime estimation of more modern semiconductor technology, albeit not specifically mentioning the $AlSiC$ baseplate, [4] has empirically derived a lifetime estimation by sampling large quantities of lifetime data from packaging technologies from 2010 to the present. This lifetime estimation also takes two specific improvements to the packaging of semiconductors into account: attaching the IGBT die by silver sintering instead of standard soldering using tin and changing standard aluminium bondwires for copper or copper alloy bondwires to increase their strength [36]. Using these sampled data, three different lifetime estimations were deduced in [4].

- Standard packaging technology since 2010 without the aforementioned improvements.
- "Model 1" lifetime estimation representing modern packaging technology with **either one** of the aforementioned improvements.
- "Model 2" lifetime estimation representing modern packaging technology with **both** of the aforementioned improvements. In this specific model, the dependency on the t_{on} and the Arrhenius term $e^{\left(\frac{\beta_2}{T_{\mathrm{jmax}}}\right)}$ are omitted.

All of them are described by (2.18), but are fitted with different constant parameters in Table A.4

$$N_{\mathrm{f}} = A\,\Delta T_{\mathrm{j}}^{\beta_1} t_{\mathrm{on}}^{\beta_3} e^{\left(\frac{\beta_2}{T_{\mathrm{jmax}}}\right)} ar^{(\beta_4 \Delta T_{\mathrm{j}} + \beta_5)} \tag{2.18}$$

with T_{jmax} the maximum junction temperature in Kelvin, and ar the ratio of loop height to the distance between the stitches of the bond wire from DBC to the chip.

After having obtained a cycle to failure using one of the aforementioned lifetime estimation models, following Miner's rule, which states that the damage from each class can be summed together, the accumulated damage can then be obtained on the component. By doing a Monte-Carlo analysis with the damage values, a failure density function Q is derived. From it, the reliability function can be obtained using $R = 1 - Q$

Device Reliability

Assuming every component in the device is critical, the device reliability can be easily obtained by multiplying all the component reliability curves. If there is redundancy of components, a reliability block diagram can be used to derive the device's reliability.

2.4 Disturbances

High-frequency Common-Mode (CM) and Differential-Mode (DM) noise is another aspect to consider in power electronic systems. DM noise is defined as the noise that is conducted line-to-line in opposite directions, which is dominated by current ripple. CM noise is defined as the noise that is conducted on the positive and negative lines in the same direction to the ground or, in the case of a ship, to the hull via parasitic capacitances. When noise current flows through the SSCB, either as a consequence of CM or DM, the additional rms current of the noise can cause additional temperature increases and thermal fluctuations, depending on the amplitude of the current ripple, which could potentially increase wear-out failures. Since CM noise flows through parasitic capacitances, the additional effect of CM noise is that at a high frequency and with high dV/dt, unwanted currents are excited that can also potentially flow into more sensitive control systems in the environment [37], which can cause sensing errors and nuisance trips.

To observe at which frequencies the CM noise is mostly concentrated, the CM V_{rms} measurement on the 700V DC-bus of a ship provided by Damen Shipyards B.V. is used [2]. The red line is the CM noise rms voltage on a system without a filter capacitor, while the green line is the CM noise rms voltage on a system with a filter capacitor. Neglecting the DC component, it is seen that most of the noise voltage is concentrated around multiples of 4000 Hz and peaks at 100 V_{rms} at 4000 Hz in the case of unfiltered CM noise.

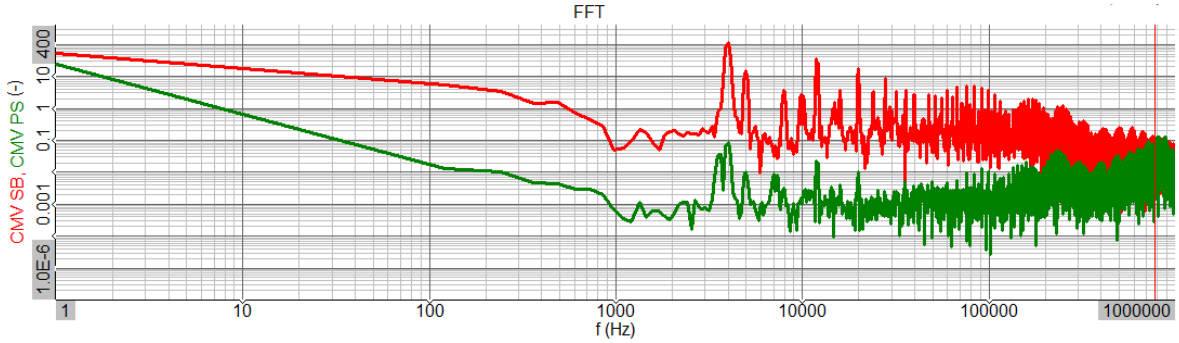

Figure 2.6: Common-mode V_{rms} measurement on DC-bus of ship [2]

Figure 2.7 [2] represents the measurement of DM noise rms voltage on a ship on the DC-bus. When neglecting the DC component, most of the voltage is concentrated again around the kHz range.

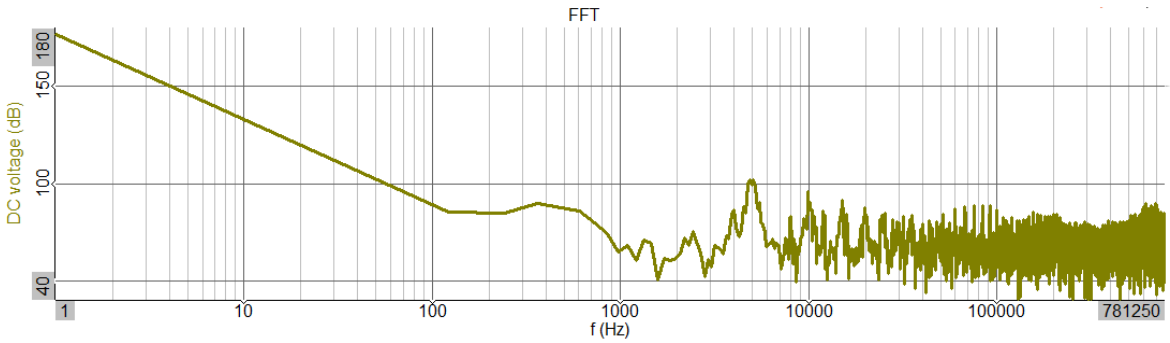

Figure 2.7: Differential mode V_{rms} measurement on DC-bus of ship [2]

Chapter 3

SSCB Model

In this chapter, the considerations revolving around the design of the use-case dependent parts (current interrupter, voltage clamping circuit, and cooling) of the SSCB are discussed, while designing it for the given specific use case.

In the first section, the use case and the function of the SSCB are explained. Next, the design choices of the current interrupter and the voltage clamping circuit are described. Then, the power losses can be calculated from the selected components, after which a heatsink is selected that keeps the components below their maximum operational temperature.

3.1 Use case

This research uses the SSCB as a DC bus breaker in the simplified radial ship power system (SPS) illustrated in Figure 3.1 with system parameters described as in Table 3.1, which are typical values on real ships obtained from measurements conducted by Damen Shipyards B.V. [2]. The components in the blue box are part of the battery system charged by the shore charger in the purple box. The green box contains the grid converter as a connection to the AC bus, which provides power for the essential equipment onboard, such as lighting and ventilation systems. Finally, the red box encapsulates the propulsion motor and motor drive.

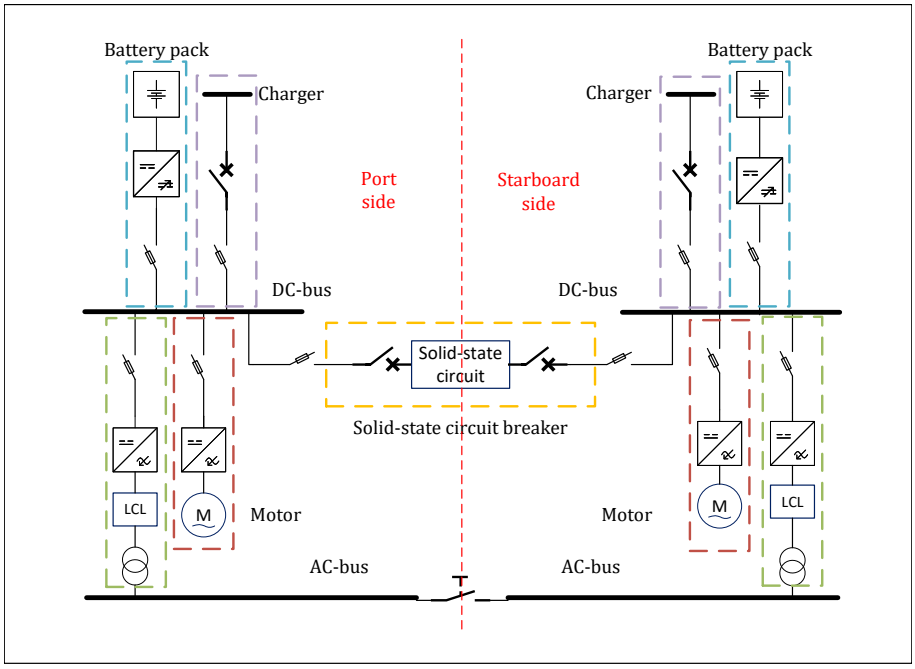

Figure 3.1: Single line diagram - Radial SPS system

Table 3.1: Ship power system parameters [2].

Description	Value	Description	Value
DC-bus voltage	1 kV	Battery capacity	300 kWh
eq. DC-bus inductance	0.22 μH	Charging power	2 MW
eq. DC-bus resistance	3.62 $m\Omega$	Motor power	150 kW
Current rating Fuses	10kA		

On ships without a DC bus tie in this radial SPS configuration, both DC buses are isolated to prevent fault current from propagating throughout the entire SPS if one side fails. This means the batteries on each side are charged with their respective charging connections, and extra cabling must be used on shore to accommodate that. Furthermore, another drawback is that power cannot be shared between the two DC bus sides, meaning that if one side needs more or less power, the other cannot compensate for it. To connect both sides while maintaining the safety of an isolated system, a solid-state circuit breaker can be used, which is reusable, unlike a fuse, and much faster than a standard mechanical circuit breaker, preventing arcing.

To build a base reliability model, it is assumed that **no faults** happen during the lifetime of the SPS and that there is no power sharing between both sides while the ship is sailing. The mission profile of the SSCB will thus only increase in power during the moments that the ship is charging. Next, it is assumed that the current flowing through it is an **ideal DC current** without any disturbances and that only half of the shore charging current flows through the SSCB to the other side. This mission profile will be based on the charging profile of actual electric vessels used as ferries with the following specifications:

- Charger voltage: 1 kV
- Charging current: 2 kA
- Current through SSCB during charging: 1kA
- Charging cycles a day: 16
- Time charging: 10 min
- Time sailing: 50 min

This results in the following daily mission profile, seen in Figure 3.2

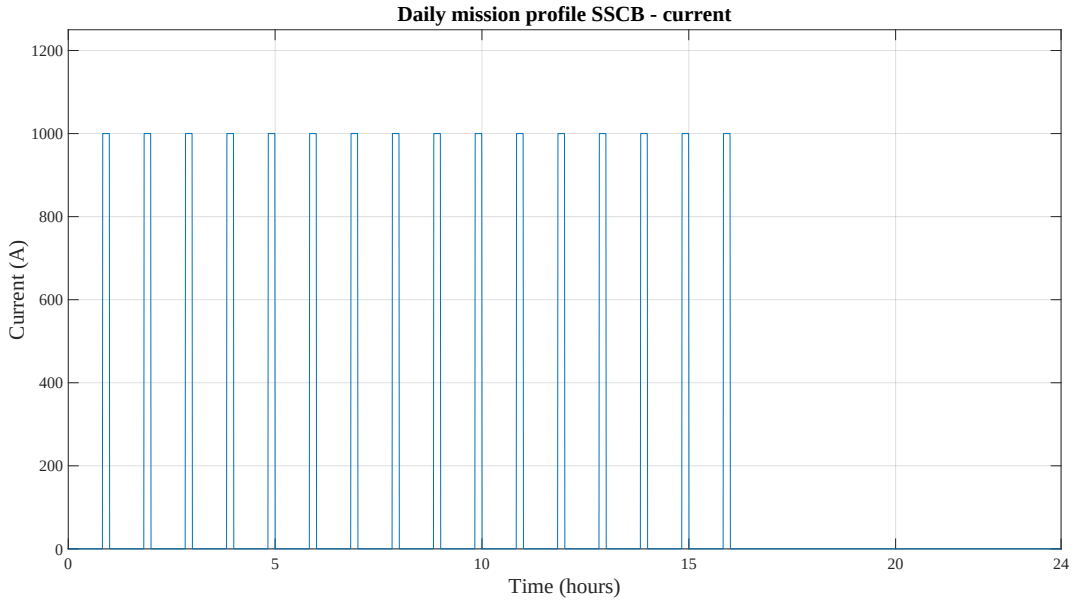

Figure 3.2: Basic daily current mission profile of SSCB with a 30s sampling time - 1kA during charging, 0 A during sailing

The SSCB is usually placed on a switchboard in a controlled environment. Following the standard classification of steel ships in [38], the following constant factors are obtained:

- Ambient temperature: 25°C
- Water coolant temperature: 40°C
- Humidity: 50%
- Vibration - displacement amplitude at 2.0 to 13.2 Hz: 1.0 mm
- Vibration - acceleration amplitude at 13.2 to 100 Hz: 0.7 m/s^2

In the case of low-frequency vibration, the maximum displacement is the main contributor to damage. With higher frequency vibrations, the acceleration is of importance.

3.2 SSCB design

Different SSCB topologies were discussed in subsection 2.2.3. The anti-parallel RB-IGCT was deemed the most suitable for this DC bus tie application due to its high on-state efficiency and voltage-blocking capabilities. However, since the RB-IGCT is a relatively new component, only a few variants are on the market, making it harder to find suitable ones to model. Thus, it was decided to model either the rectifier-assisted IGBT topology or the anti-series IGBT topology. Considering the conduction losses, the anti-series topology would fit the use case better. However, the rectifier-assisted topology reflects commercially available SSCBs, which have been on the market for some years, leading to more reference data available to build a reliable model.

This topology uses one IGBT and four diodes in a full-bridge configuration. For simplicity during referencing in this thesis, the diodes that conduct from port side to starboard side are referred to as **forward** facing diodes. The diodes that conduct from starboard side to port side are referred to as **backward** facing diodes. These are respectively denoted as D_{fw} and D_{bw} in the SSCB simulation model in Figure 3.3.

3.2.1 Power semiconductor sizing

The selection of suitable power semiconductor components depends on many factors. First, the rated operational voltages and currents should be designed for the nominal power of the application, which is 1 kV and 1 kA. Following [39], the rated voltage for half-bridge devices should be at least a factor $\frac{1}{0.65}$ higher than the operational voltage to have it switch safely, meaning that the components should already be rated for at least 1.54 kV. For the rated current, there is no specific guideline; thus, in this research, a 10% margin in the current rating has been assumed, leading to a minimum current rating of 1.1 kA.

Next, even though it is assumed that the SSCB never has to trip in the base reliability model, the transients through the SSCB during emergency turn-off of the switch should still be studied to select the appropriate peak voltage and current rating of the semiconductors. To do so, a simulation model has been made in PLECS, show in Figure 3.3.

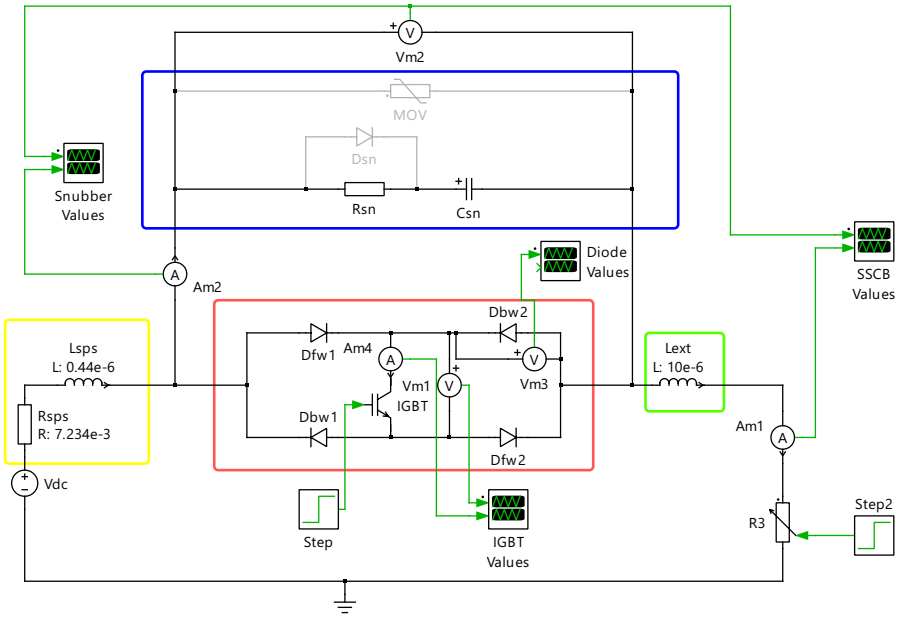

Figure 3.3: PLECS SSCB simulation model

The model consists of 4 main factors important for the correct sizing of the SSCB components:

- The opening time of the **IGBT**, in addition to the processing delay of the current sensing system in the current interruption circuit(red).
- The arbitrary external inductance L_{ext} to limit the di/dt during SPS faults (green).
- The maximum clamping voltage of the over-voltage protection circuit using a resistor-capacitor (RC), resistor-capacitor-diode (RCD) or a metal oxide varistor (MOV) configuration(blue).
- The inherent power system resistance and inductance from the port side and the starboard side of the DC busses of the given system are described in Figure 3.1(yellow).

Peak current sizing

The peak current through the IGBT is dependent on the first two of the aforementioned factors, which are the total opening time of the SSCB and the external inductance. In case the system inductance is large enough that the IGBT has enough time to fully open before reaching the maximum rated peak current, no external inductance is needed. It was observed from several datasheets that IGBTs mostly have peak currents which are twice the rated nominal current, which in this case would be around 2 kA. In this

particular use case as a 1 kV DC bus tie, it was seen that with just the system inductance of 0.44 µH and a total opening time of 8µs (4µs fault sensing delay + 4µs opening time) [2], a peak current of 15 kA was observed through the IGBT (Figure 3.4), which is significantly higher than the maximum peak current rating of a switch.

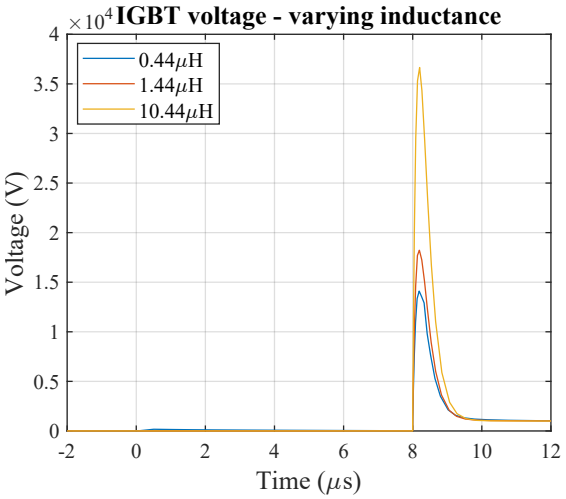

(a) Difference in peak voltage over IGBT with varying inductance

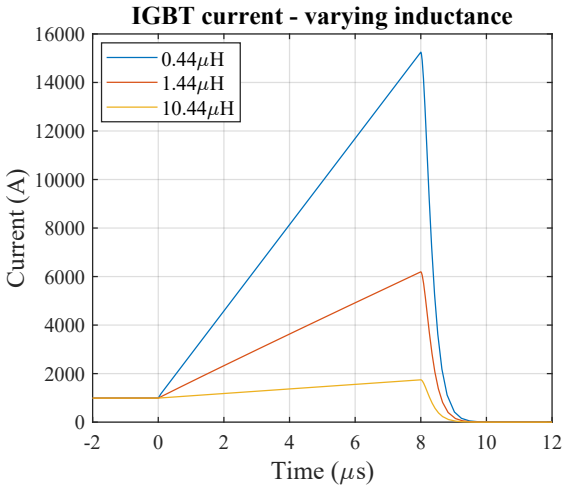

(b) Difference in peak current over IGBT with varying inductance

Figure 3.4: Showcase of importance in inductance to limit the peak current through the IGBT and, in turn, reduce the voltage over the IGBT in an SSCB without any energy absorption circuit. A fault is simulated at the 0-second mark.

Consequently, an external inductance of 10 µH was chosen to limit the current through the IGBT to a maximum of 1.74 kA, well below the theoretical limit of 2kA, taking into account potential extra delays in the total opening time of the switch.

Although the IGBT is then protected from high surge currents, a result of the external inductance is that the peak voltage over the IGBT increases drastically due to $V = L\frac{di}{dt}$. From Figure 3.4a, it can be seen that the increase in inductance has a larger effect on the voltage over the IGBT than the reduction of the $\frac{di}{dt}$ due to it.

Peak voltage sizing

To protect the IGBT from overvoltage during the turn-off period, voltage clamping circuitry has to be used as described in subsection 2.2.4. For this system, the impact of the two most common voltage clamping circuits, the RC(D) and MOV, is investigated. The measurements for this investigation are obtained from the "SSCB Values" probe in Figure 3.3, meaning that the voltage values over the snubber and IGBT are identical over time due to their parallel placement, whereas the current that went through the IGBT is always cut off at 8µs and redirected to the voltage clamping circuit, which results in a current plot like Figure 3.5:

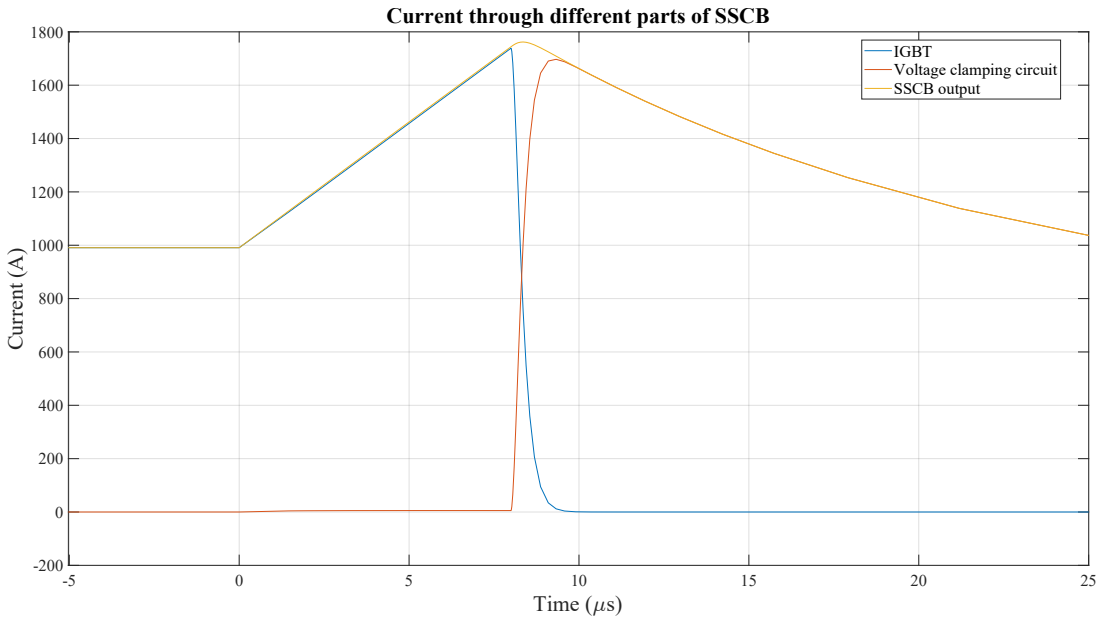

Figure 3.5: Current through IGBT and voltage clamping circuit parts of the SSCB. Future plots will only show the SSCB voltage/curent outputs.

To compare the voltage clamping circuits and to see the effects of the individual components on each circuit, simulations have been run:

- In case of the RC circuit, the peak clamping voltage and clamping time are dependent on the values of the capacitor and resistor as seen in Figure B.1 and Figure B.2. From the plots, it is concluded that the peak voltage depends heavily on the snubber resistor, which was expected due to the redirected current through the R_{snub}. The size of the snubber resistor also affects the rate at which the energy dissipates from the capacitor. Another thing to note is that the smaller the resistor, the higher the possibility of voltage or current resonance between the capacitor and system inductance. Selection of the resistor thus depends mainly on a trade-off between maximum allowable overvoltage and (stable) energy dissipation speed. The capacitor has no effect on the peak voltage. Instead, it only has an impact on the energy dissipation speed.

- The RCD snubber has the solution to the increase in voltage during IGBT turn-off, which is to place a diode in parallel with the snubber resistor, creating a low resistance path to the capacitor. The effect of the RCD snubber on the SSCB can be seen in subsection B.1.2. Compared to the RC snubber, the resistor does not impact the peak voltage anymore and only affects the energy dissipation speed. However, it is seen in Figure 3.6 that for the small snubber resistance of 1 Ω, the clamping voltage is still a bit higher than the RC snubber counterpart. Unlike the resistor, the capacitor does impact the peak voltage in the RCD snubber, but not as much as the resistor would in an RC snubber. As the capacitance increases, however, the maximum current through the snubber, and thus the SSCB, does increase substantially. A major drawback of this snubber is that it is unidirectional, which means that it is unsuitable for use in this bus tie configuration.

- The MOV is just a single component with a clamping voltage of around two times the nominal rated voltage [1], depending on the current flowing through it during IGBT turn-off. Unlike the RC(D) snubber, which peaks at a certain voltage and drops gradually thereafter, the MOV will hold the voltage at a relatively steady level before immediately dropping to 1 kV when the energy is dissipated. A comparison in SSCB voltage and current behaviour between a 1.15 kV rated MOV and a typical RC and RCD snubber is given in Figure 3.6. From it, it can be seen that the MOV will cut the current off much faster than the RC snubbers, albeit at a higher peak voltage. Another benefit of the MOV is that there is no chance of oscillations due to the lack of a capacitor. This

greatly simplifies the selection of suitable MOVs, unlike the RC snubbers, where multiple trade-offs have to be considered. Lastly, this component is bidirectional, which makes it the optimal voltage clamping circuit in this use case.

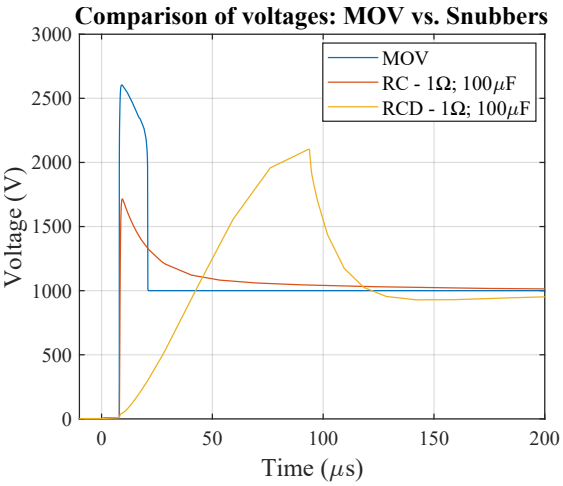

(a) Difference in peak voltage over SSCB with different voltage clamping circuits

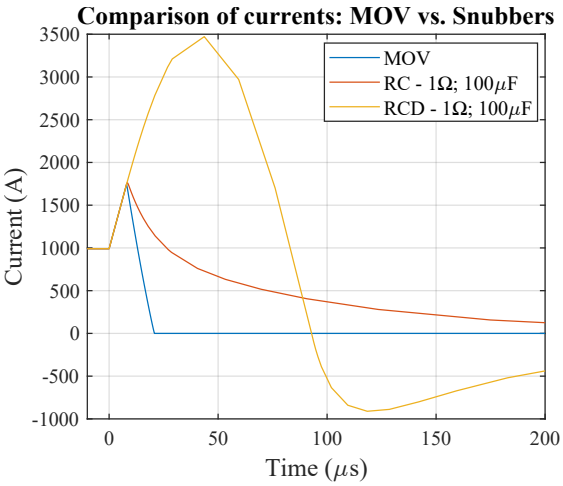

(b) Difference in peak current through SSCB with different voltage clamping circuits

Figure 3.6: Comparison between MOV, RC and RCD voltage clamping circuit effects on the behaviour of the SSCB during fault interruption.

List of used components

Considering the system values and the selection of MOV as the voltage clamping circuit, the following components in Table 3.2 have been chosen for the reliability research. The rated voltages and currents were selected based on the availability of commercially available components.

Table 3.2: Selected components for SSCB

Power component	Name	rated DC voltage(V)	rated DC current(A)	clamping voltage MOV at 200 A (V)	peak surge current(A)	Max. junction temperature ($°C$)
IGBT	CM1200HC-66X	3300	1200	N/A	2400	150
Diode	RM1200DC-66X	3300	1200	N/A	10600	150
MOV	V881BA60	1150	N/A	2340	70000	85[1]

3.3 Power loss model

Following the selection of components, the power loss has to be calculated for each of them in order to obtain a thermal profile. Since the SSCB is not expected to switch often due to its functionality as an emergency circuit breaker, only the conduction losses have to be taken into account. To obtain the conduction loss for the bipolar semiconductor components in the current interruption part of the SSCB,

[1]Maximum storage temperature

the following formula is used from [22] for the IGBT and diode, respectively

$$\begin{cases} P_{\text{cond,T}}(T_j) = \frac{1}{T}\int_0^T V_{CE}(T_j) I_{\text{T}}\, dt \\ \quad = V_T(T_j)|I_{\text{ave,T}}| + R_{CE}(T_j) I^2_{\text{RMS,T}}. \\ P_{\text{cond,D}}(T_j) = \frac{1}{T}\int_0^T V_D(T_j) I_{\text{D}}\, dt \\ \quad = V_D(T_j)|I_{\text{ave,D}}| + R_D(T_j) I^2_{\text{RMS,D}}. \end{cases} \tag{3.1}$$

For the IGBT, the variables are: V_{CE} the collector-emitter (forward) voltage, T_{j} the junction temperatures, I_{T} the IGBT current, R_{CE} the on-resistance. For the diode, the variables are: V_{D} the forward voltage, I_{D} the diode current, R_{D} the on-resistance. In case of frequent switching, such as the case in the reference paper [22] with multi-level converters or when noise is introduced into the power flow, (3.1) takes the average power loss during the switching period of the IGBT as the conduction losses. This can be expressed as an addition of a term taking into account the threshold voltage V_{T} of bipolar devices and the average current $I_{\text{ave,T}}$, and another term considering the on-resistance of the semiconductor R_{D} and the RMS current squared.

In the case of obtaining the simplest base reliability model, it is assumed that the SSCB will never have to trip and that the current flowing through it is an ideal DC. Then the conduction loss calculation can be simplified to (3.2)

$$\begin{cases} P_{\text{cond,T}}(T_j) = V_{\text{CE}}(T_{\text{j}}) I_{\text{T}} \\ P_{\text{cond,D}}(T_j) = V_{\text{D}}(T_{\text{j}}) I_{\text{D}} \end{cases} \tag{3.2}$$

where the conduction loss is just the forward voltage V_{CE} multiplied by the current going through the component.

3.3.1 Data extraction

To get the necessary data for power loss calculation, the V-I curves as seen in Figure B.5 from the component datasheets are digitised for the different junction temperatures specified. Then, the resolution of the digitised plot can be improved by linearly interpolating the datapoints on each curve to a set number of 1000 datapoints. This also ensures that all the digitised curves will have the same length, which is important for interpolating **between** the different junction temperature V-I curves. In this case, $((T_{\text{max}} - T_{\text{min}}) \cdot 10 = 1250)$ curves have been interpolated for the minimum and maximum junction temperature data given in the datasheet. Doing so and calculating the power losses over each individually interpolated curve results in a look-up table that obtains the power losses per given current at a moment. Example of a power loss curve with three junction temperatures of the IGBT and diode would look like Figure 3.7

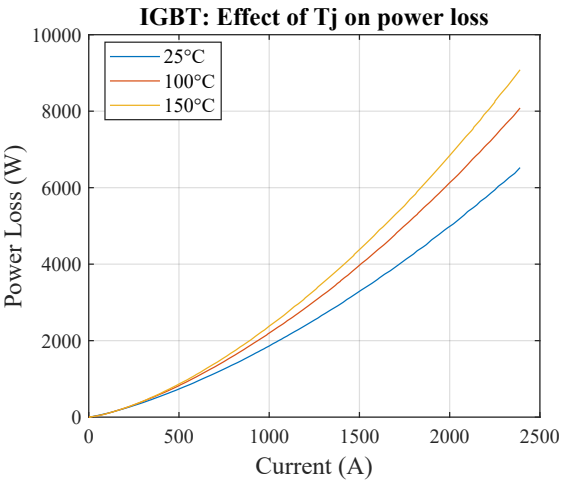

(a) Curves of IGBT of three junction temperatures as power loss vs. current

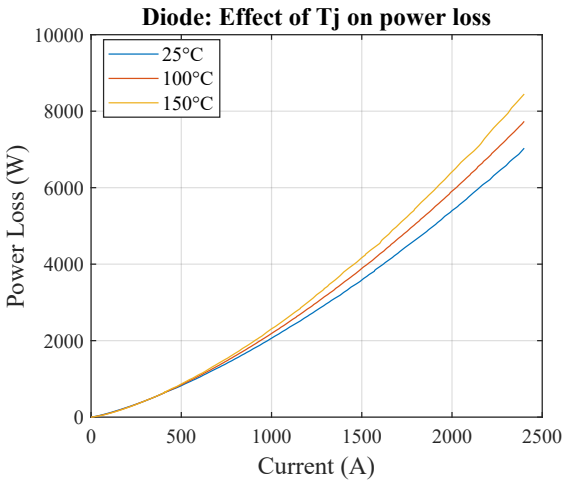

(b) Curves of the diode of three junction temperatures as power loss vs. current

Figure 3.7: Power loss curves of IGBT and diode as a function of current and the junction temperature

From the plot, it is noted that the higher the junction temperature inside a power device, the higher the power losses become due to an increase in internal resistance, with a maximum difference of 27.9% for the IGBT and 11.9% for the diode at 1 kA between 25°C and 150 °C. In the case of the base mission profile during a charge current of 1 kA and a junction temperature equal to a coolant temperature of 40°C the losses amount to 1931 W and 2088 W for the IGBT and diode, respectively.

3.4 Cooling

Using the obtained power loss model, the changes in temperature of the power device can be modelled. In this section, decisions that had to be made considering the cooling of the SSCB are presented.

3.4.1 Thermal RC network

According to [29], a power semiconductor subjected to a power pulse longer than $\sim$1 second is considered to have reached steady state and thus thermal equilibrium. Since the power-on durations in the base mission profile are on the order of minutes, it is reasonable to assume that the thermal inertia of the power device does not affect the amplitude of the thermal swings in said mission profile. Furthermore, the junction temperature is needed for the lifetime calculation models as described in subsubsection 2.3.3. Therefore, in case only the impact of the mission profile on device lifetime is being investigated, such as the case with the base mission profile, modelling the Cauer thermal model discussed in subsubsection 2.3.3 with just the thermal resistances is sufficient. If there is only one device per heatsink, this results in the junction temperature as described in (3.3)

$$T_{\mathrm{j}} = P_{\mathrm{loss}} \left(R_{\mathrm{th(j,c)}} + R_{\mathrm{th(c,s)}} + R_{\mathrm{th(s,a)}} \right) + T_{\mathrm{a}} \tag{3.3}$$

To reduce cost and total size of the cooling system, multiple power devices could be attached to a single heatsink. However, in the case of the rectifier-assisted bidirectional SSCB, the diodes which are forward-bias at a certain moment need to be thermally isolated from the ones which are reverse-bias to prevent thermal coupling and thus a reduction of the lifetime of the diodes which are not loaded. This means that only the "forward" facing diodes or the "reverse" facing diodes can be put together on the same heatsink. The junction temperature per power device is then calculated using Equation 3.4 with subscript x the individual devices, n the total devices on the heatsink and ΔT_{sa} the difference in temperature between the sink and coolant

$$\begin{cases} \Delta T_{\text{sa}} = (\sum_{x=1}^{n} P_{\text{loss},x}) \cdot R_{\text{th(s,a)}} \\ T_{\text{sink}} = \Delta T_{\text{sa}} + T_{\text{a}} \\ T_{\text{j,x}} = P_{\text{loss,x}}(R_{\text{th(c,s)}} + R_{\text{th(j,c)}}) + T_{\text{sink}} \end{cases} \tag{3.4}$$

3.4.2 Thermal components

The required thermal resistances are found in the datasheets [40] [41] of the chosen components. The RM1200DC-66X diode module consists of two separate diodes in parallel connected to the same baseplate, meaning an option is given to just utilise one diode and thus half a module, which is what is needed for the base reliability modelling. From the datasheet, it is then found that the thermal junction-to-case resistance $R_{\text{th(j,c)}}$ is 16.5 K/W and the thermal case-to-sink resistance $R_{\text{th(c,s)}}$ for a half module is 15.0 K/W.

Thermal components IGBT

The chosen CM1200HC-66X IGBT module from the same manufacturer also has two components in parallel, although not entirely isolated from each other, since the emitter and gate are pre-connected to each other. Still, it should be possible to use them individually if the collector of one of them were not to be connected. Moreover, it has exactly the same baseplate dimensions (140 x 130 mm) as the diode module. Therefore, it was expected that although the $R_{\text{th(j,c)}}$ might differ due to the usage of different semiconductors, the $R_{\text{th(c,s)}}$ would remain the same as the diode module. However, the IGBT module datasheet specified a $R_{\text{th(c,s)}}$ of 7.5 K/W, which led to a significant difference in calculated junction temperatures and eventual lifetime calculations in the initial testing phase, even though both modules have similar power losses and are loaded with the same number of power cycles in a year.

To explain this mismatch in $R_{\text{th(c,s)}}$ for both modules, a datasheet with a similar IGBT module from Infineon [42] is used. Herein, it is specified that the collectors should be connected externally. Hence, the entire area of the baseplate is used to dissipate the heat, lowering the thermal resistance between the case and sink. Therefore, it is possible that the halving of the thermal case to sink resistance in the IGBT module compared to the diode module is due to Mitsubishi assuming that the entire module will always be used instead of half of it. However, since only one side of the module is used for this thermal model, the $R_{\text{th(c,s)}}$ will be set to match the thermal resistance of 15.0 K/W from (half) the diode module.

Heatsink

The heatsink design plays a vital role in managing the temperature of the chosen power devices. Depending on the power losses and the thermal resistances of the device, a suitable heatsink is fitted.

There are two types of cooling that can be used: forced air cooling and liquid cooling. For the case area (140 x 130 mm) of the selected power devices, the commercially available forced air cooling solutions can only provide a thermal resistance as low as 0.05 K/W with a maximum airflow of $120 m^3/hr$ [43]. Calculating the junction temperature with (3.3) of the individual IGBT and diodes with the obtained heatsink thermal resistance at 1kA, would give a result of 185.9 $°C$ and 210.2$°C$ respectively. Severely exceeding the maximum allowable temperature of the components. Therefore, liquid cooling needs to be used due to its lower thermal resistance. From [44], it is found that modern liquid-cooled heatsinks, also called cold plates, can reach a low thermal resistance of up to 0.005 K/W depending on the coolant flow rate. From commercially available cold plates, the ATS-CP-1002 [45] fits the selected power device size. Furthermore, it has a thermal resistance range from around 0.014 to 0.0064 K/W, depending on the coolant flow rate from 0.74 to 7.4 L per minute, which provides a suitable range of thermal resistances to keep the junction temperatures below the maximum temperature of the semiconductors. By using one

heatsink per device and a thermal resistance of 0.0075 K/W (coolant flow rate 4L/min), the initial estimation of the junction temperatures for the IGBT and diodes are 103.7°C and 121.4°C respectively, well below the maximum of 150 °C. However, there is an emphasis on "initial estimation" due to the power loss being dependent on the junction temperature and vice versa, creating a feedback loop. Therefore, iterative modelling should be used.

Iterative modelling

To get a more accurate junction temperature estimation, iterative modelling is used. The iterative modelling method calculates the final junction temperature per instance in time in iterative steps. In the first cycle, it calculates the junction temperature assuming the minimum junction temperature starts at the coolant temperature of 40°C. From the power loss model, the power losses are obtained for the minimum junction temperature, which are then multiplied by the thermal resistances as described in (3.3) leading to the aforementioned junction temperature of 103.7 °C for the IGBT and 121.4 °C for the diode in subsection 3.4.2. This result is then fed back into the iterative calculation loop, recalculating the junction temperature with the new junction temperature. The iterative model will keep doing so until it finds that the old and new junction temperatures do not differ more than 0.01 °C. This causes the final power loss to be 2248 W for the IGBT and 2228 W for the diode, an increase of 16.4% and 6.7% respectively compared to the initial calculation, well within the limits of the maximum power difference at 1 kA in Figure 3.7. As a result, the final junction temperatures for a 1 kA operation increase to 114.2°C for the IGBT and 126.9°C for the diode.

The final values after iterative modelling to be used in the mission profile are thus as such in Table 3.3

Table 3.3: (Thermal) Values after iterative modelling

Component	$R_{\text{th(j,c)}}$(K/W)	$R_{\text{th(c,s)}}$(K/W)	$R_{\text{th(s,a)}}$(K/W)	P_{loss} at 1 kA (W)	T_{j} at 1 kA (°C)
IGBT	0.0105	0.015	0.0075	2248.6	114.2
Diode	0.0165	0.015	0.0075	2228.1	126.9

Chapter 4

Reliability Modeling

In this chapter, the lifetime of the designed SSCB in chapter 3 is calculated based solely on the wear-out failure mechanisms due to thermomechanical fatigue. This is because during regular operation under rated conditions, these failures are most observed in power devices [9]. Furthermore, it is of interest in this thesis to observe the eventual effects of mission profile changes and the impact of electrical noise on the total lifetime of the SSCB, meaning that the focus is on the gradual wear-out of the SSCB and not the spontaneous overvoltage and overcurrents, which can happen anytime during the entire lifetime of the SSCB. To do so, a similar method as described in Figure 4.1 from [3] is followed to calculate the individual power semiconductor component lifetimes inside the SSCB.

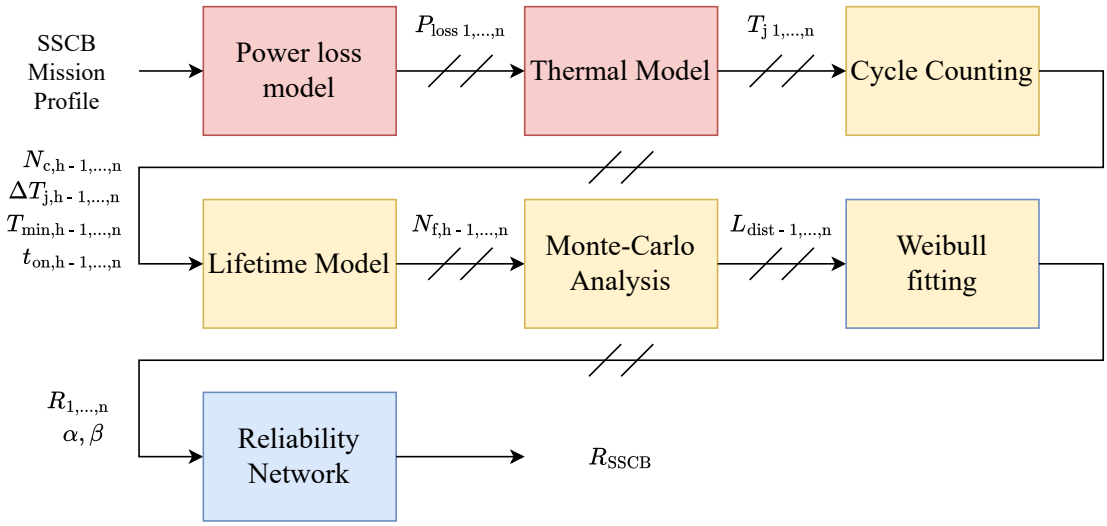

Figure 4.1: Steps taken for individual power semiconductor component reliably modelling following [3].

With the definitions described in Table 4.1:

Table 4.1: Variable definitions of Figure 4.1

Variable	Definition	Variable	Definition
P_{loss}	Power loss	L_{dist}	Lifetime distribution
T_{j}	Junction temperature	R	Reliability function
N_{c}	Profile cycles	α	Scale parameter
ΔT_{j}	Junction temperature swing	β	Shape parameter
T_{min}	Minimum temperature	Subscript n	Per component definition
t_{on}	Power-on time	Subscript h	Per class definition
N_{f}	Cycles to failure		

The colours of each block relate to the layout of this chapter. In the first section, the profiles obtained from the power loss model and thermal models are presented. In the second section, the steps taken

to obtain the damage distribution of a component and its reliability curve are explained. Lastly, the reliability curve for the entire SSCB is acquired.

4.1 Mission profiles

The first two steps seen in Figure 4.1 have already been covered in chapter 3 and are coloured in red. To generate a daily power loss profile of the different components in the current interrupter part of the SSCB, each data point in the current mission profile is put through the power loss model, resulting in a power loss profile as seen in Figure 4.2 with the obtained power losses at 1kA in Table 3.3

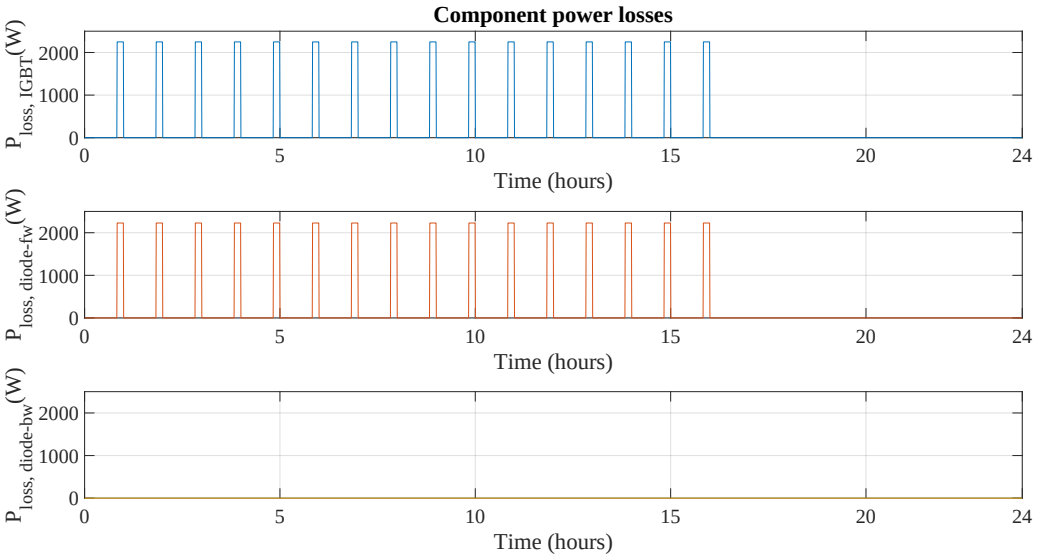

Figure 4.2: Daily power loss profile of each component in the current interrupter of the SSCB

It is clear that the power losses only occur in the IGBT and the forward (see section 3.2 for forward-backwards explanation) facing diodes. This is due to the defined use case in chapter 3 only describing current to flow from port to starboard side, meaning no current will go through the backwards-facing diodes. This in turn leads to the following thermal profiles shown in Figure 4.3 with the junction temperatures described in Table 3.3

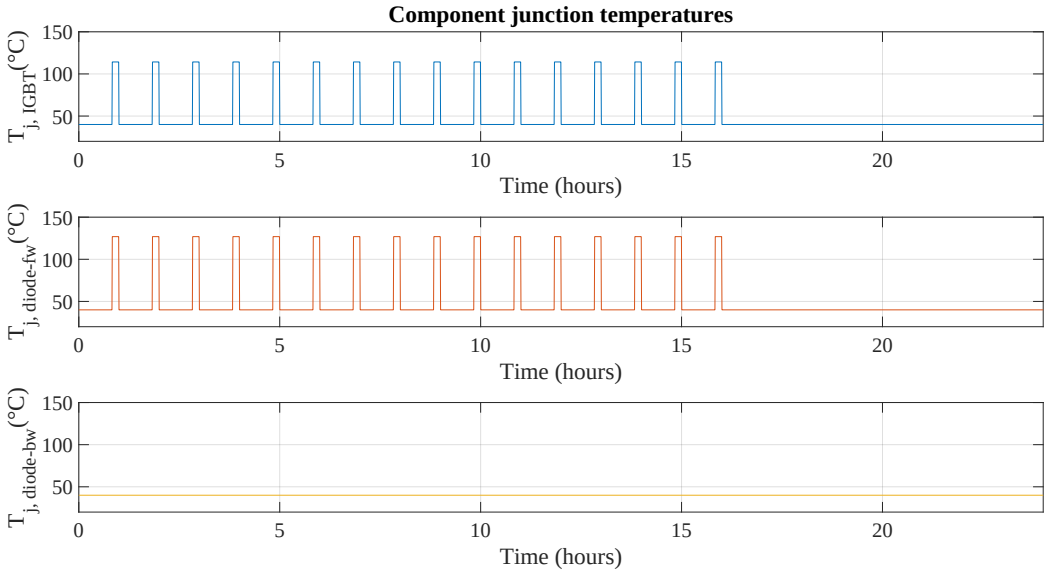

Figure 4.3: Daily junction temperature profile of each component in the current interrupter of the SSCB

4.2 Component reliability

Having obtained the thermal profile of the junction temperature of the individual components, the reliability model can be designed. As described in Figure 4.1, this section describes the method to obtain the number of different temperature cycles. After which, a lifetime estimation model is selected, and the number of cycles to failure is calculated. Then, by using Monte Carlo analysis to insert modelling uncertainties, a probability mass function (PMF) is acquired for the estimated lifetimes. Lastly, utilising Weibull fitting, the scale parameter α and shape parameter β are estimated and used to fit a continuous Weibull curve, which, once integrated and subtracted from 1, yields the reliability curve of a component.

4.2.1 Rainflow counting

The first step is to count the number of thermal cycles the component endures during the duration of the mission profile, in this case, one single day. A thermal cycle is defined as the cycle wherein the temperature goes up a certain amount and afterwards drops back to the same starting temperature. A thermal profile can have large amounts of different cycles overlapping each other, which makes it difficult to count each individual thermal cycle. Therefore, to count these cycles, the rainflow counting method is used, which separates these different cycles into h classes and counts them individually. The working principle of the rainflow counting method is described as the following four steps [46] [47]: Hysteresis filtering, peak-valley filtering, discretisation, and counting using the rainflow counting algorithm.

Hysteresis filtering

As the first step, temperature fluctuations that are deemed to be too small to affect the lifetime calculations of a profile are filtered out to save on processing time. The amplitude threshold for filtering is determined based on the required sensitivity margin for each analysis. In case of the ideal thermal profile without any minor thermal fluctuations as described in the previous section, this step is unnecessary and has been omitted.

Peak-Valley filtering

In this step, only the points where the reversals in direction of the temperature change occur are saved. In the case of a sine wave, these reversal points can be detected as the points where the derivative is zero.

In the thermal profile described in Figure 4.3, the shape of a block wave leads to some complications due to the presence of a longer period during which the temperature stays at a steady value. Thus, a point has to be selected that indicates the correct reversal points. In this case, due to the CIPS lifetime model requiring only the heating time, also called the "power-on-time" of the component [8], it was chosen to count the first rising edge of the junction temperature as the first reversal point and the falling edge as the second reversal point. By doing so, the power-on-time of each cycle can then be obtained by subtracting the time of the low value from the time of the high value. This results in the reversal points as shown in Figure 4.4. Please note that the line in between points is to clarify the position of the reversal points and is not used in the lifetime calculations.

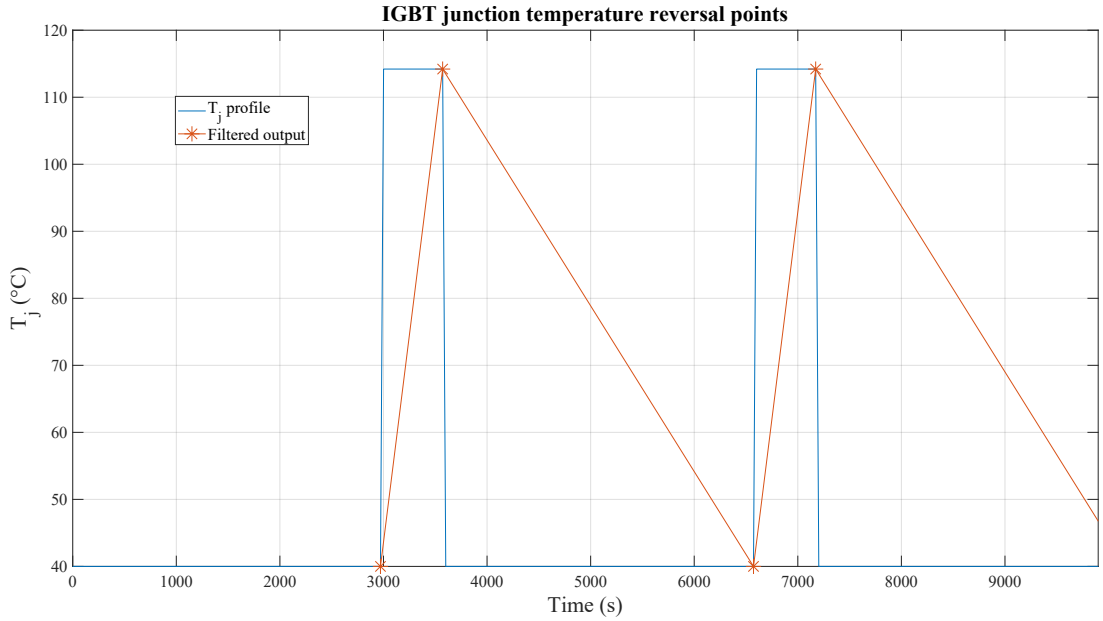

Figure 4.4: First two cycles showing the IGBT junction temperature reversal points marked with asterisks. Note that the line between points is for clarity purposes and is not used for calculations.

Discretisation

To create sets of data, the reversal points which have a similar range of junction temperature, are sorted into bins. The higher the number of bins, the smaller the range of temperatures and thus the higher the resolution of the dataset will be. However, that also results in a larger dataset and thus longer computational times. In this case, the bin sizes are in sizes of 1 $°C$.

Counting algorithm

Lastly, the actual cycle counting is done following a counting algorithm described as in [47] and [6]. The algorithm counts cycles by considering a moving reference point of the sequence called **Z**, and a three-point subset which moves with **Z** and can either include **Z** or exclude it. The first and middle points in the subset are defined together as **Y**, and the middle and last points in the subset are called **X**. Furthermore, in both **Y** and **X**, the points are always sorted chronologically from earlier to later in time, but are not necessarily always consecutive reversal points. Lastly, the range of **Y** and **X** are denoted as **r(Y)** and **r(X)**, respectively and is defined as the difference in amplitude between their own two points. Following these characteristics, the counting algorithm works as follows:

1. Set reference point **Z** as the first reversal point.

2. Keep reading the next reversal points until at least three points are gathered. If no more data points are left, count each remaining range as half a cycle.

3. Check whether **r(X) < r(Y)**

   (a) If yes, add another reversal list to the subset and use the latest three added values in the subset to form a new **Y** and **X** and redo step 3.

   (b) If not, proceed to step 4

4. Check whether **Y** includes **Z**

5. If yes, count **Y** as a half cycle. Then remove the first reversal point from **Y** and shift the reference point **Z** to the second reversal point in **Y** and repeat the process from step 2.

6. If not, **Y** is counted as 1 full cycle and discarded, after which the algorithm starts at step 2 again.

Figure C.1 visualizes this process in a flowchart.

MATLAB provides a built-in function named "rainflow" which automatically executes the discretisation, differentiation and counting when a thermal profile is provided. After dividing the thermal profile into cycle classes, it outputs per class the number of cycles, the temperature swing bin, and the mean temperature bin, and additionally, the begin and end times of each (half) cycle per cycle class. To use these values for the lifetime models, some of them have to be further processed into the following:

- Amount of cycles per cycle class $N_{\mathrm{c,h}}$, obtained from the output as it is.
- Junction temperature swing per cycle class $\Delta T_{\mathrm{j,h}}$, obtained from taking the centre value of each bin.
- Minimum junction temperature per cycle class $T_{\mathrm{jmin,h}}$, obtained by subtracting half the temperature swing from the mean temperature.
- Power-on-time per cycle class $t_{\mathrm{on,h}}$, obtained by subtracting the time of the reversal point at a rising edge from the time of the reversal point at a falling edge, as mentioned in the "Peak-Valley filtering" section.

When applied to the obtained reversal points of the IGBT and the diodes, the output is as described in Table 4.2:

Table 4.2: Output of the rainflow counting, with a number h defining a cycle class.

	$N_{\mathrm{c,h}}$	$\Delta T_{\mathrm{j,h}}(^{\circ}C)$	$T_{\mathrm{jmean,h}}(^{\circ}C)$	$T_{\mathrm{jmin,h}}(^{\circ}C)$	$t_{\mathrm{on,h}}(s)$
IGBT (h = 1)	16	74	77	40	600
Forward Diode (h = 1)	16	87	83.5	40	600

4.2.2 Lifetime calculation

The next step would be to obtain the lifetime of the component by calculating the number of cycles to failure and the subsequent damage that the components in the SSCB can endure before the lifetime estimation predicts a failure, as a consequence of wear-out failure mechanisms, such as bond-wire lift-off and solder cracking.

Miner's rule

Before the lifetime calculation, it needs to be clarified what "damage" to the component means. Damage is a variable representing the state of health of a component, where D = 1 reflects a broken component. To calculate the damage done per time interval by one class of thermal cycles, obtained from the rainflow

counting, the number of cycles in that time period is divided by the number of cycles to failure due to that one specific class as described in (4.1) [3]:

$$D_{\mathrm{h}} = \frac{N_{\mathrm{c,h}}}{N_{\mathrm{f,h}}} \tag{4.1}$$

Assuming that the Miner's rule is applicable, the individual damages as a consequence of each individual thermal cycle class obtained can be added up to obtain the accumulated damage (D_{acc}) per time interval [33] expressed as:

$$D_{\mathrm{acc}} = \sum D_{\mathrm{h}} \tag{4.2}$$

In this case, since the mission profile entails the period of one day, D_{acc} would represent the accumulated damage that the component endures in one day.

Lifetime model

To obtain the $N_{\mathrm{f,h}}$, one of the empirically derived lifetime estimation models described in chapter 2 can be used, which were the LESIT [7], CIPS with correction [8] [32] and the recent Zhou "model 2" [4] and are described for each cycle as in (4.3). (4.4) and (4.6) respectively

$$N_{\mathrm{f,h}} = A\Delta T_{\mathrm{j,h}}^{a} e^{\left(\frac{E_{\mathrm{a}}}{k_{\mathrm{B}} T_{\mathrm{jmean,h}}}\right)} \tag{4.3}$$

$$N_{\mathrm{f,h}} = A\Delta T_{\mathrm{j,h}}^{\beta_1} t_{\mathrm{on,h}}^{\beta_3} I_{\mathrm{bond}}^{\beta_4} V_{\mathrm{class}}^{\beta_5} D_{\mathrm{bond}}^{\beta_6} e^{\left(\frac{\beta_2}{T_{\mathrm{min,h}}}\right)} \tag{4.4}$$

With a correction factor

$$\frac{N_{\mathrm{f,h}}(t_{\mathrm{on,h}})}{N_{\mathrm{f}}(1.5)} = \begin{cases} 2.25 & t_{\mathrm{on,h}} \leq 0.1s \\ \left(\frac{t_{\mathrm{on,h}}}{1.5}\right)^{-0.3} & 0.1s \leq t_{\mathrm{on,h}} \leq 60s \\ 0.33 & t_{\mathrm{on,h}} \geq 60s \end{cases} \tag{4.5}$$

$$N_{\mathrm{f,h}} = A\,\Delta T_{\mathrm{j,h}}^{\beta_1} t_{\mathrm{on,h}}^{\beta_3} e^{\left(\frac{\beta_2}{T_{\mathrm{jmax,h}}}\right)} ar^{(\beta_4 \Delta T_{\mathrm{j,h}} + \beta_5)} \tag{4.6}$$

The "model 2" is taken into consideration from [4], due to the assumption that due to the novelty of the selected components, that they have the silver sintering and bond wire improvements applied in their packaging.

To validate the correct output of the generated lifetime models in MATLAB, the obtained results are compared to their respective papers. As can be seen in Figure C.2, the outputs of the tested LESIT and CIPS model are equal to the example outputs in their respective papers. To further validate the obtained models, the aforementioned models are then verified together with the Zhou "model 2" and the CIPS with correction model in Figure 4.5a. The obtained outputs for the LESIT, CIPS and "model 2" are as expected from the output in [4]. The CIPS with correction is also shown in Figure 4.5a. However, due to the t_{on} being just two seconds, the correction factor does not change the output of the CIPS much, since it only alters the values obtained outside the 0.1 and 60-second t_{on} range. By changing the on time to 60 seconds, a bigger difference between the CIPS and CIPS with correction can be seen in Figure 4.5b. [8] [31].

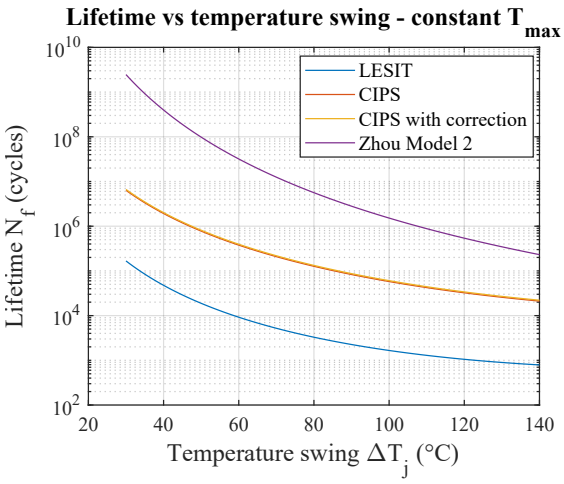

(a) Validation of different lifetime models using $t_{on} = 2\,s$

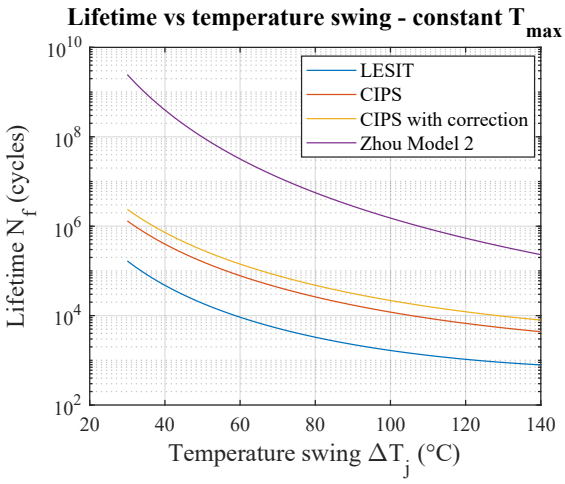

(b) Validation of different lifetime models using $t_{on} = 60\,s$

Figure 4.5: Validation of the cycles to failure of the selected lifetime estimations by comparison with [4] using a constant T_{max} and a changing T_{mean} and T_{min} due to a varying ΔT_j. Common parameters used are: $V_{class} = 12V$, $I_{bond} = 10A$, $D = 400\,\mu m$ and $ar = 0.3$

From Figure 4.5, the comparison shows that by setting a fixed T_{max}, the LESIT model will always predict the lowest cycles to failure independent of the ΔT_j, followed by both CIPS model versions and lastly the "Model 2". With the on-time nearing 60 seconds, the regular CIPS model is seen to show differences in cycle to failure estimation from the CIPS with correction model.

To relate the lifetime estimation models with the mission profile in the base case, the chip-related values are filled in the models where applicable. For the CIPS (with correction), the V_{rated} for both the IGBT and diodes are obtained from their respective datasheets [40] and [41] as 3300 V. The voltage class V_{class} is defined as $V_{rated}/100$ [33], which results in $V_{class} = 33V$. However, the rated bondwire current I_{bond} and bondwire diameter D_{bond} are not specified in the datasheets. Therefore, values had to be assumed using the tested values from the original CIPS paper [8], leading to a bondwire current of 15 A and a bondwire diameter of 300 µm. For the "model 2" of Zhou, the ar value is taken $0.19 \leq ar \leq 0.42$ to represent aluminium bonding wire failure [48], for this thesis, a value of $ar = 0.31$ is chosen following [49]. In summary, the constant values which are not dependent on the mission profile are represented in Table 4.3

Table 4.3: Constant parameters in the presented lifetime estimation models for the selected semiconductor devices

	$I_{bond}(A)$	$V_{class}(V)$	$D_{bond}(\mu m)$	ar
IGBT/Diodes	15	33	300	0.31

To give an overview of the cycle to failure estimations representative of the mission profile, the lifetime estimations are plotted in Figure 4.6a. The values from Table 4.3 are used, and a fixed minimum junction temperature of 40 $°C$ is set, representing the coolant temperature. Then, the thermal swing is set to be a maximum of 110$°C$ to not exceed the maximum junction temperature of 150$°C$ of the selected devices, simulating the increase in power loss through the device. Due to the CIPS being sensitive to the long on-time, it is observed that the CIPS will always predict the lowest number of cycles to failure compared to the other models in this specific scenario with the minimum junction temperature a constant value.

To analyse the sensitivity of the different lifetime estimation models to different thermal swings in the mission profile, the output in Figure 4.6a is normalised with the result at $\Delta T_j = 30K$ as the base value, which resulted in Figure 4.6b. It is seen that the LESIT and "Model 2" are the most sensitive to changes

in temperature swing, with both the CIPS variations having an estimated 10 times difference in lifetime prediction compared to the other two. A reason for this difference is that the CIPS is dependent on the T_{min}, which is fixed in this comparison. The other models are dependent on the mean and maximum temperature, which will gradually increase as the thermal swing increases and thus have a greater effect on the degradation term in their respective equations.

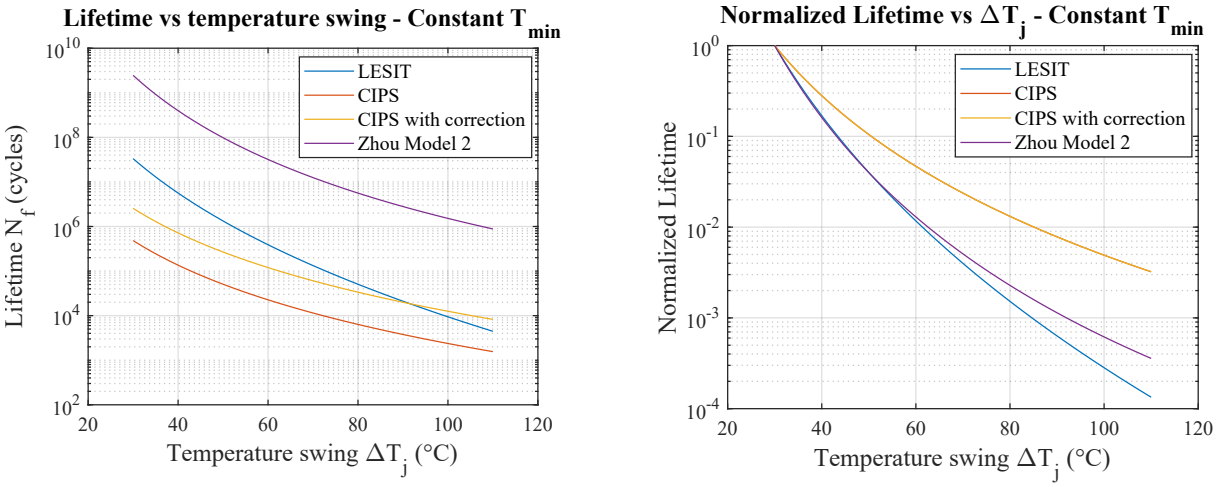

(a) Lifetime estimation output using mission profile parameters

(b) Normalised lifetime estimation output using mission profile parameters

Figure 4.6: Comparison of lifetime estimation differences using mission profile parameters with a variable temperature swing and a fixed T_{min}. Common parameters used are: $V_{\text{class}} = 33V$, $I_{\text{bond}} = 15A$, $D = 300\,\mu\text{m}$, $t_{\text{on}} = 600\,s$ and $ar = 0.3$.

With these results, the CIPS model is overall the more conservative option due to its consistently low cycle to failure prediction at high on-times above 600 seconds in Figure 4.6a and lower sensitivity to temperature swings when a constant minimum temperature is taken. These properties make it such that the obtained results can reflect the worst-case lifetime a component can endure as a consequence of thermal fatigue. Furthermore, it reflects the minimum sensitivity that the lifetime of a component will have on different changes in the mission profile. To decide between the CIPS or CIPS with correction, the CIPS with correction factor is able to reduce the unrealistic impact of long (>60 s) and very short (<0.1 s) power-on times [32]. With these additional properties, the CIPS with correction was used as a low baseline for the absolute cycle to failure prediction and the sensitivity analysis.

It should be taken into account that the empirically derived lifetime estimation models were obtained by stress test cycling components in a range of around 30 to 100 K. So, to estimate lifetimes of components which experience thermal cycles outside of this range, a margin of error should be taken into account. For the CIPS, the output of the lifetime prediction of the model for thermal swings lower than $30°C$ has been stated to be lower than what a component is able to endure in practice [50]. Consequently, the CIPS will give the worst-case scenario estimations when applied to low thermal swings. The CIPS with correction, even more so, since low power-on-times are related to lower thermal swings when taking thermal capacitance into account. Unlike the regular CIPS model, the CIPS with correction will keep increasing in lifetime as the power-on-time goes lower, and will thus predict lower cycles to failure than the regular CIPS in that scenario.

Having only one class of thermal cycle in the mission profile in Table 4.2, the cycles to failure, the damage a day and the estimated lifetime until certain failure for the IGBT and diodes are presented in Table 4.4

Table 4.4: Results from the CIPS with correction per component

	$N_{\mathrm{f}}(cycles)$	$D_{\text{acc-day}}(-)$	$L(years)$
IGBT	$4.985 \cdot 10^4$	$3.210 \cdot 10^{-4}$	8.55
Forward diode	$2.439 \cdot 10^4$	$6.559 \cdot 10^{-4}$	4.18

4.2.3 Monte Carlo analysis

A limitation in the estimation of lifetime in Table 4.4 is that it is based on fixed beta values. However, the beta values are empirically obtained in [8], meaning that there is always some variation between each individual component. To get a more representative lifetime estimation, variation in the beta values has to be applied to get a damage distribution. From [51] and [52], the variation should follow a normal distribution with a 5% variation in the beta values, meaning that three standard deviations should be equal to 0.05 as described with $3\sigma = 0.05$ and thus $\sigma = \frac{0.05}{3}$, leading to the beta values distribution in Figure C.3. Next, the Monte Carlo method was used to simulate 10^5 lifetime estimations with the applied variations, resulting in a lifetime distribution in the form of a probability mass function describing the chance of how long the IGBT and diode can survive before a guaranteed failure, as shown in Figure 4.7

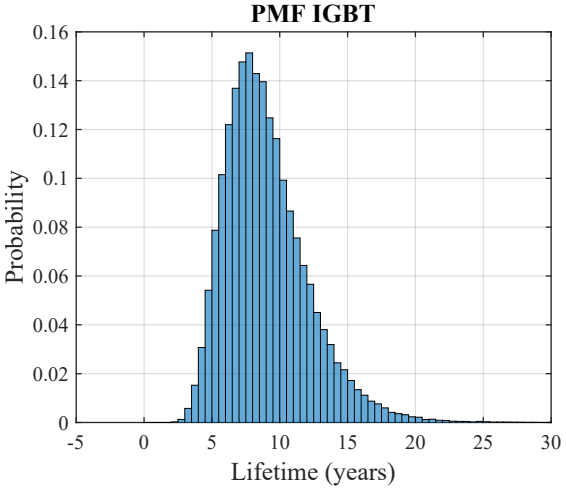

(a) Lifetime probability mass function of IGBT.

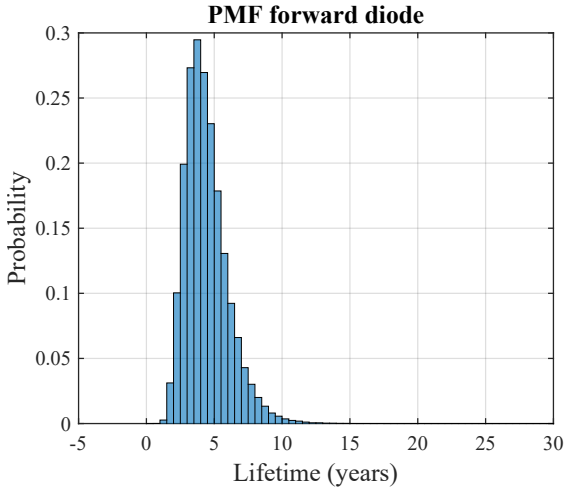

(b) Lifetime probability mass function of forward diode

Figure 4.7: Lifetime distribution of the IGBT and forward diode obtained from 100,000 Monte Carlo simulations with normally distributed beta values $\sigma = \frac{0.05}{3}$.

Since the backwards-facing diode is not loaded in the considered mission profile and not connected to a mutual heatsink with the other components, there is no thermal swing. Therefore, it can be concluded that the backwards-facing diode does not endure any stress and thus is irrelevant for the lifetime calculation under the considered mission profile.

4.2.4 Reliability curve

With the obtained lifetime distribution, the next step would be to fit a Weibull probability density curve over the discretely distributed data to obtain a continuous curve. The most general form of the classical Weibull distribution is the three-parameter probability density function [53] in (4.7).

$$f_X(x \mid a,b,c) = \frac{c}{b}\left(\frac{x-a}{b}\right)^{c-1} \exp\left\{-\left(\frac{x-a}{b}\right)^{c}\right\}, \quad x \geq a. \tag{4.7}$$

With x a unit of time, a the location parameter, b the scale parameter, and c the shape parameter. The location parameter sets the beginning of the Weibull curve, but since components only start to fail after

the age of $x = 0$, the a can be set to 0 [53]. To clarify the equation for lifetime estimation, x, b, c are renamed into t, α, β respectively, resulting in (4.8).

$$f(t \mid \alpha, \beta) = \frac{\beta}{\alpha}\left(\frac{t}{\alpha}\right)^{\beta-1} \exp\left\{-\left(\frac{t}{\alpha}\right)^{\beta}\right\}, \quad t \geq 0. \tag{4.8}$$

with t the time in years, α the scale parameter, and β the shape parameter. The part of the equation before the exponent can be described as the amount of failures per unit time λ in (4.9).

$$\lambda(t \mid \alpha, \beta) = \frac{\beta}{\alpha}\left(\frac{t}{\alpha}\right)^{\beta-1} \tag{4.9}$$

The cumulative distribution function (CDF), describing the percentage of devices that have failed already compared to the total number of devices, is obtained as (4.10) after calculating the integral of $f(t \mid \alpha, \beta)$:

$$F(t \mid \alpha, \beta) = 1 - \exp\left\{-\left(\frac{t}{\alpha}\right)^{\beta}\right\}, \quad t \geq 0. \tag{4.10}$$

The scale parameter α determines the spread of the lifetime distribution and represents the time at which 63.2% of components are expected to have failed. This specific percentage arises because, regardless of the value of β, when $t = \alpha$, the cumulative distribution function results in $F(t) = 1 - e^{-1} \approx 63.2\%$. The shape parameter β determines whether the failure rate λ will decrease over time, stay constant or rather increases over time depending on whether $\beta < 1$, $\beta = 1$ or $\beta > 1$ respectively, due to the $\beta - 1$ exponent on the t in (4.9), which leads to the characteristic failure rate curves in Figure A.1.

MATLAB provides the "wblfit" function to estimate these parameters, resulting in the results in Table 4.5

Table 4.5: α and β obtained from "wblfit" function in MATLAB.

	α	β
IGBT	10.07	3.02
Forward diode	4.96	2.91

Which leads to the Weibull curve as seen in Figure 4.8, plotted over the previously obtained probability density function of each of the relevant components.

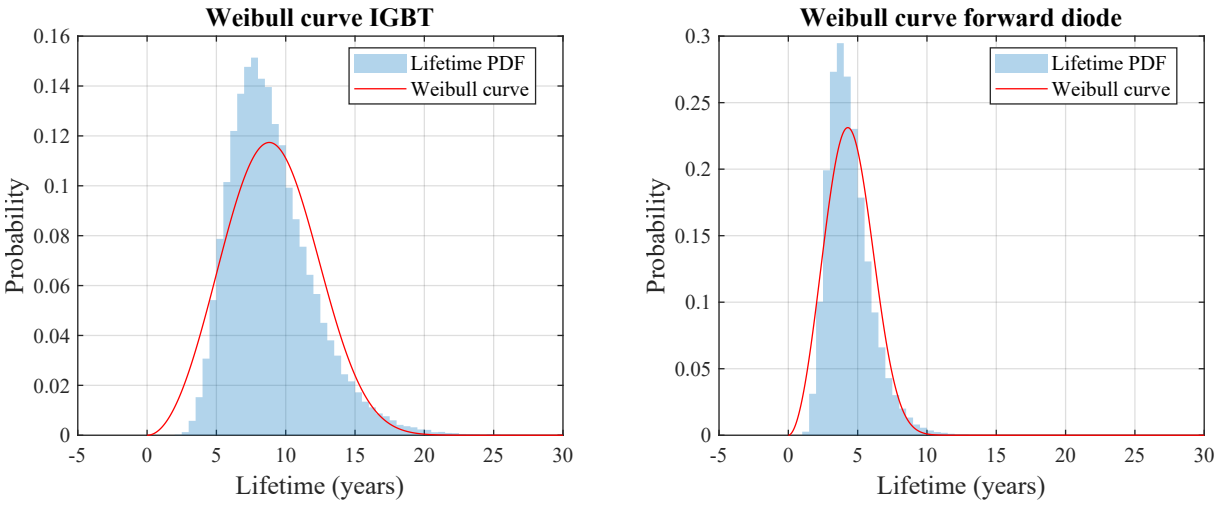

(a) Weibull curve of IGBT

(b) Weibull curve of forward diode

Figure 4.8: The Weibull curve plotted with α and β values obtained from the "wblfit" function in MATLAB. Note that the lifetime can never be smaller than 0 years.

By integrating over the Weibull curve, a curve is obtained, which will represent the percentage of the components in the Monte Carlo sample size that have failed as a function of time. To get the reliability curve $R(t \mid \alpha, \beta)$, the complement of this curve is taken to obtain:

$$R(t \mid \alpha, \beta) = \exp\left\{-\left(\frac{t}{\alpha}\right)^{\beta}\right\}, \quad t \geq 0. \tag{4.11}$$

and the consequent plots like Figure 4.9

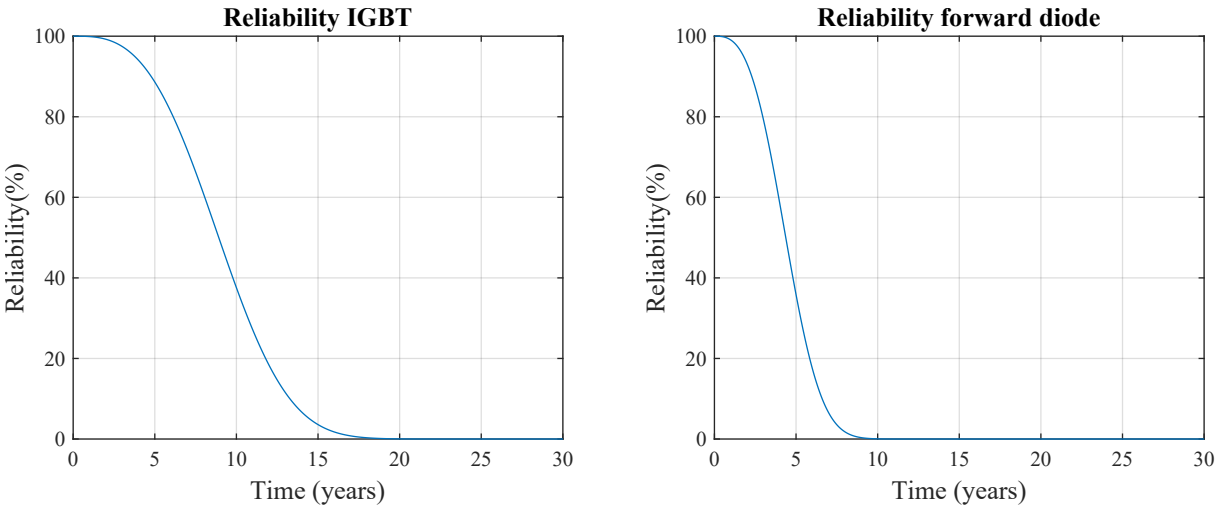

(a) Reliability of the IGBT

(b) Reliability of the forward diode

Figure 4.9: The reliability of the relevant components.

4.3 Device reliability

Finally, after having obtained the individual component reliabilities, the overall SSCB reliability curve can be obtained. In this case, it is assumed that every component inside the SSCB is necessary, meaning that there are zero redundant components. By expressing that in terms of reliability network modelling, the reliabilities per component of the reliability block diagram are in all series, as described in Figure 4.10.

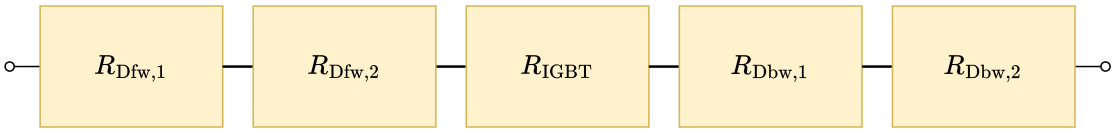

Figure 4.10: Reliability block diagram of the SSCB describing a series reliability network.

This means that in order to obtain the total SSCB reliability, all of the reliabilities just have to be multiplied by each other, resulting in (4.12)

$$R_{\text{SSCB}} = R_{Dfw,1}R_{Dfw,2}R_{IGBT,1}R_{Dbw,1}R_{Dbw,2} \tag{4.12}$$

With $R_{Dfw,n}$ the reliability of the forward-facing diodes, $R_{IGBT,n}$ the reliability of the IGBT and $R_{Dbw,n}$ the reliability of the backwards-facing diodes. Since both identical forward-facing diodes have exactly the same mission profile and are thus equally loaded, their reliability curves are the same, just like the case with both identical backwards-facing diodes. Therefore, to obtain the SSCB reliability curve, the reliability curves are squared and then multiplied, resulting in (4.13)

$$R_{\text{SSCB}} = R_{Dfw}^2 R_{IGBT} R_{Dbw}^2 \tag{4.13}$$

and obtaining the following reliability curve in Figure 4.11

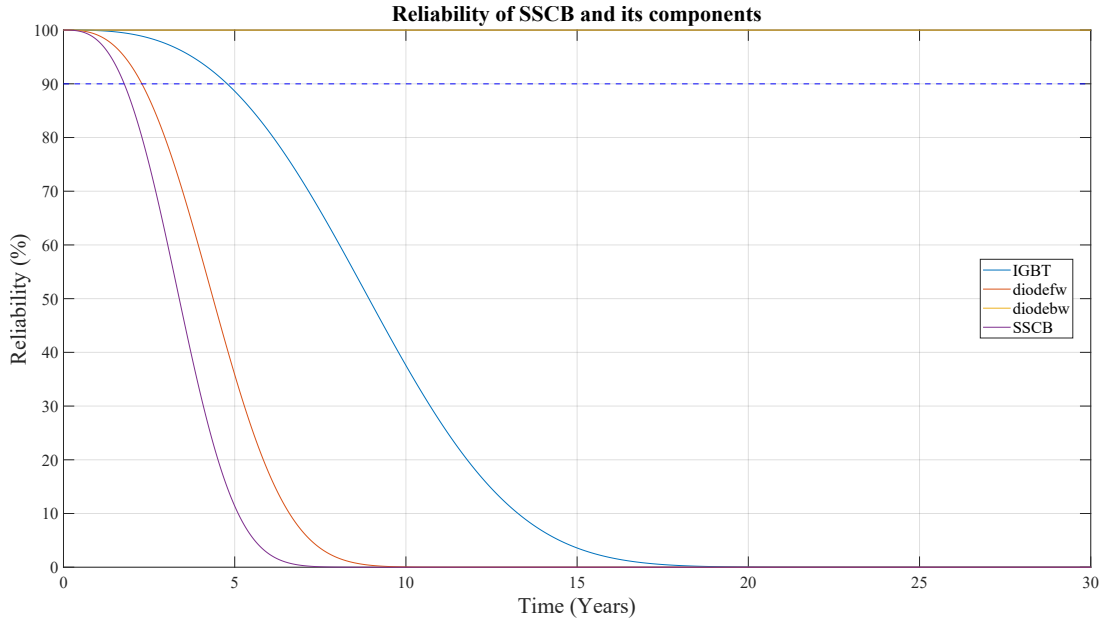

Figure 4.11: Reliability of the SSCB and its components as a consequence of purely the wear-out failure mechanisms.

To better interpret the results of the reliability calculation, only the times at which the lifetime of each component crosses the 90% reliability mark are noted, called the B-10 lifetime. The B-10 lifetime denotes the point in time by which 10% of the components in the sample size are expected to have failed, implying a 90% probability that a randomly selected component is operational at that instance in time. The results of the B-10 lifetimes are shown in Table 4.6.

Table 4.6: B-10 lifetimes due to thermal fatigue

	SSCB	Forward diode	IGBT
B-10 liftime (years)	1.78	2.29	4.78

It is to be noted that the obtained B-10 lifetime does not necessarily guarantee that 90% of the samples are actually operational by then. This number is merely an estimation done by the CIPS with correction, which only takes into account the wear-out failure mechanisms. Many other factors, which are harder to estimate, such as catastrophic failures (sudden overcurrents, cosmic rays, etc.) and environmental factors (humidity, vibration), can play a role in reducing a component's lifetime.

Chapter 5

Sensitivity Analysis

With the developed SSCB model in chapter 3 and the reliability model in chapter 4, the sensitivity analysis can be carried out. In this chapter, the main goal is to see the impact on the SSCB lifetime due to changes in the mission profile, SSCB configuration, and operational parameters in comparison with the base configuration from the previous chapters. This chapter is thus divided into four sections: The first one containing the impact on lifetime as a consequence of the mission profile changes. The second section contains the lifetime changes due to the addition of parallel components in the SSCB. Thirdly, the parameters regarding the operation of the SSCB are changed, for example, the coolant temperature. Lastly, the final section gives an overview of the quantified benefit and relative drawbacks of each change made.

5.1 Mission profile sensitivity

To observe the changes due to the mission profile, multiple changes compared to the base model made in chapter 4 can be implemented, such as:

- Bidirectional charging: Instead of charging through the SSCB 16 times from one side, divide the charging direction into **x** times from one side and (**16 - x**) times from the other side.
- Changing the charging power: Change the power at which the batteries are getting charged while obtaining the same amount of energy per charging cycle.

5.1.1 Bi-directional charging

One of the options to potentially improve the lifetime of the SSCB is to make use of its bidirectionality to reduce the stress on the diodes. However, in doing so, instead of making use of just 2 diodes and 1 IGBT, now 4 diodes and 1 IGBT are utilised. The bi-directionality will thus be a trade-off between increasing the number of failure points in the system and reducing the stress on each individual diode.

To do so, the mission profile is split into a positive charging current, indicating a current flow from port side to starboard side and a negative charging current, indicating a current flow in the reverse direction. Since the current cycles are still separated from each other in the minutes domain, it is safe to assume that the positive and negative current cycles will not affect each other's junction thermal cycle due to the low thermal inertia of the junction. Furthermore, following Miner's rule, the daily accumulated damage is independent of the charge current sequence. Thus, mission profiles in which the charging power goes through the SSCB from the starboard side at the end of the day, like in Figure 5.1, are used to carry out the sensitivity analysis of this section.

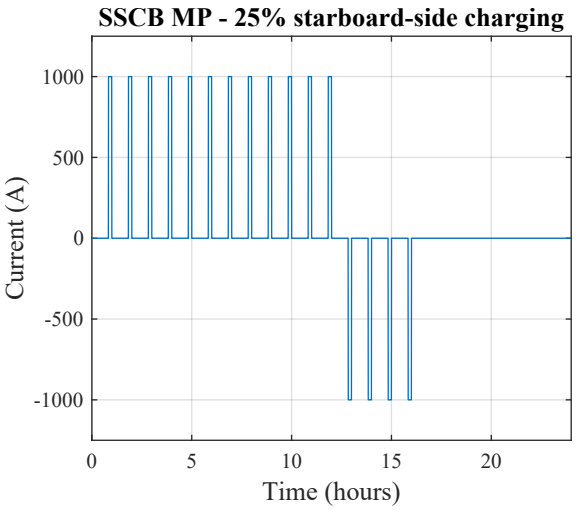

(a) Mission profile of SSCB where 25% of the time the charging power flows from the starboard side to the port side.

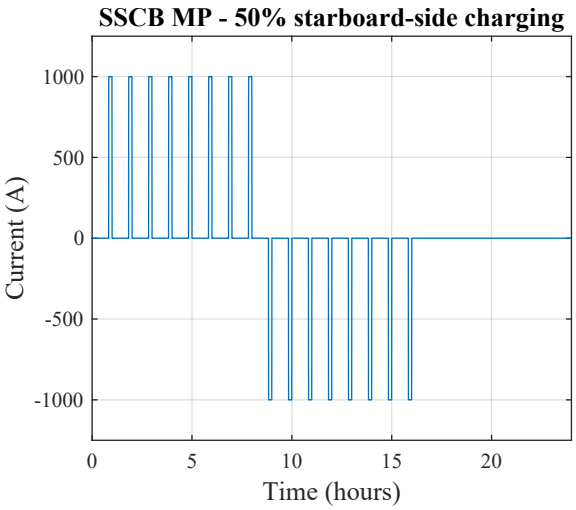

(b) Mission profile of SSCB where 50% of the time the charging power flows from starboard side to the port side.

Figure 5.1: Mission profile of SSCB where 25% and 50% of the time the charging power flows from the starboard side to the port side.

To give a clear comparison between the effects on lifetime due to the changes in charging sides, the results of the SSCB, IGBT and the forward diode are all normalised to the value obtained when charging only from the port side. For the backwards diode, the results are normalised to the B-10 lifetime obtained when only charged from the starboard side. Running the model yields the following result in Figure 5.2.

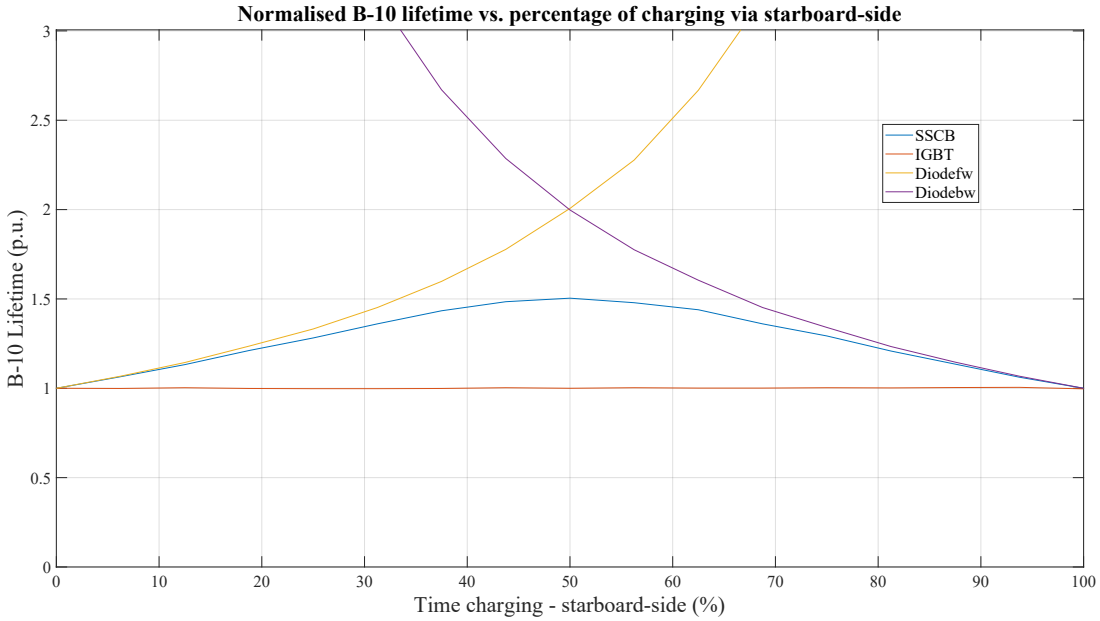

Figure 5.2: Impact on the B-10 lifetime of the SSCB and its components due to the effect of the time spent charging on either side of a ship.

As can be seen, by loading the SSCB equally from the starboard and the port side during charging, a B-10 lifetime increase of 1.5 times for the SSCB and an increase of 2 times for the diodes can be achieved compared to the case wherein the SSCB is only loaded from one side. This means that the lifetime can be improved when the components are less thermally cycled, even though more components are affected by degradation. Although the underlying strategy is conceptually straightforward, it is required that the

vessel be equipped to support charging from both sides. Specifically, this means installing a second shore charging inlet on the starboard side or integrating an internal switching mechanism capable of selecting the side of the vessel through which the charging current flows through the SSCB first.

5.1.2 Changing charging power

The second mission profile-oriented option to influence the lifetime of the SSCB is to alter the stresses on each component by either reducing or increasing the amount of power during charging. This change in power is done by altering the current through the SSCB, which in turn will result in different power losses and thus heat. This relation in heat generated versus the current through the SSCB and its components is shown in Figure 5.3.

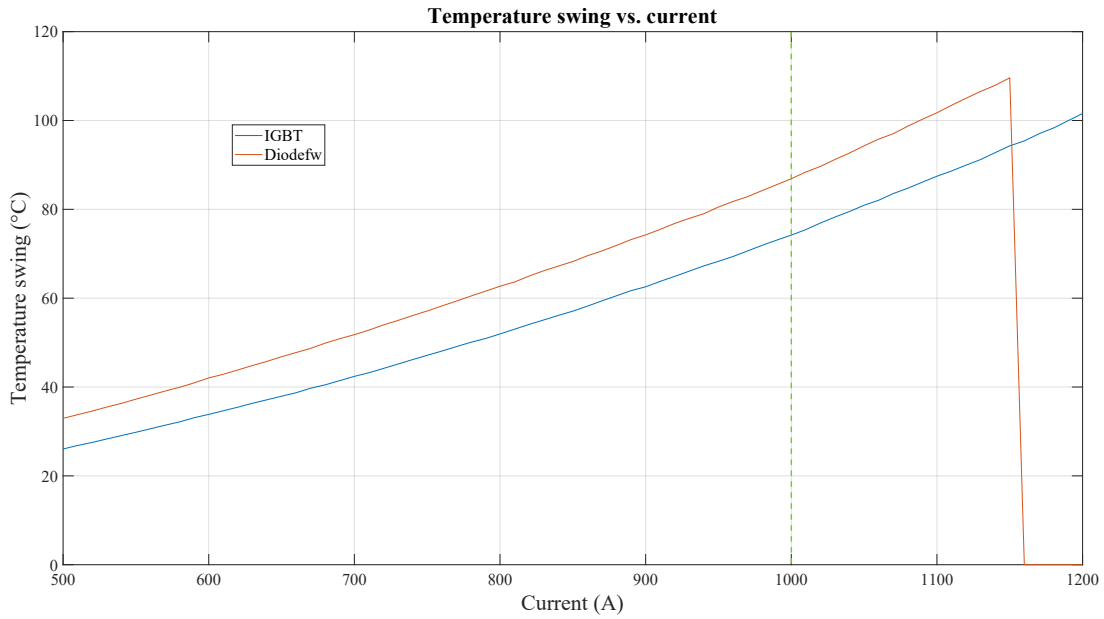

Figure 5.3: Change in junction temperature swing as a function of the current through the SSCB with the "base" case at 1000 A shown as the green dashed line.

From this chart, it can be concluded that by halving the current through the SSCB from 1000 A to 500 A, the junction temperature swing reduces by more than two times from 87°C and 74°C to 33°C and 26°C for the forward diode and the IGBT respectively. By increasing the current, the temperature swings get approximately linearly larger until the forward diode junction reaches the maximum temperature swing of 110°C and thus the maximum junction temperature of 150°C. For this analysis, it is assumed that once it reaches this maximum temperature, the component is considered broken. As a consequence, it is seen that at 1150 A the forward diode fails due to the temperature exceeding the maximum junction temperature of 150°C.

To maintain the same energy transferred to the batteries, the charging should also take longer, namely, inversely proportional to the reduction in charging power. Since the charging time is always above 60 seconds, the on-time will have no effect on the lifetime estimation in this analysis due to the nature of the CIPS with correction model. The resulting change in B-10 lifetime of the SSCB as a consequence of changing the charging power is shown in Figure 5.4 on a logarithmic scale.

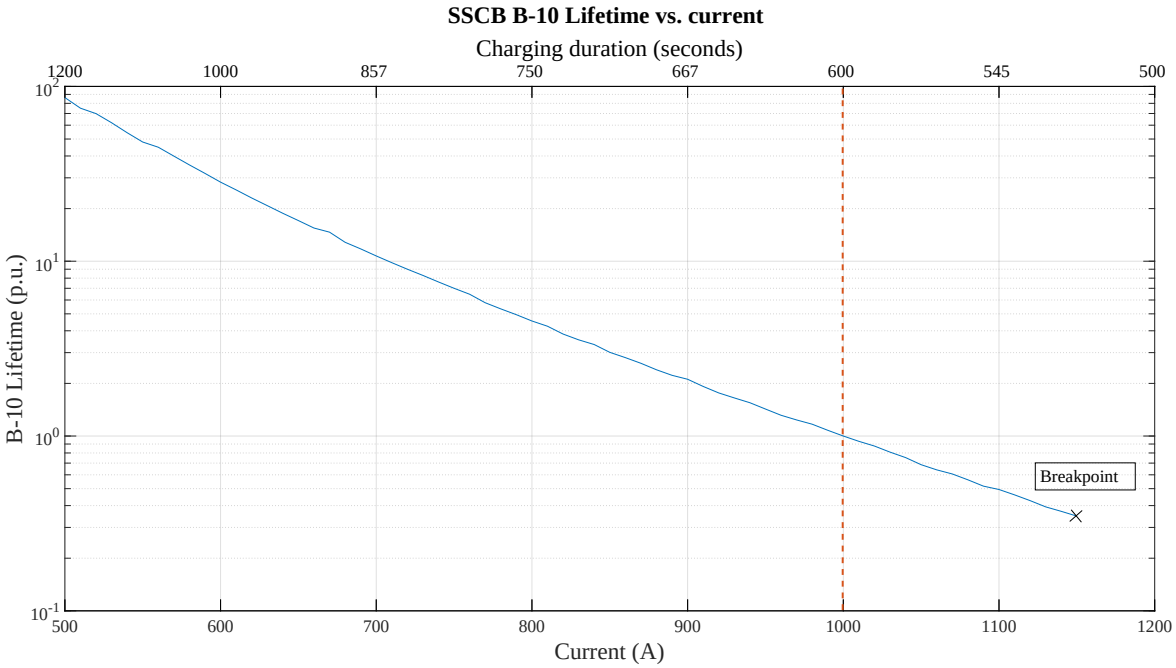

Figure 5.4: SSCB B-10 lifetime as a function of the charging current and the charging time while maintaining the same amount of energy transfer through the SSCB as in the base case (orange line).

From it, it is observed that by reducing the current through the SSCB by 100 A and increasing the charging time by about a minute, the B-10 lifetime already doubles. By halving the charging current and doubling the charging time, the B-10 lifetime improves roughly 85 times. At 1150 A, the maximum temperature of a component is reached, and the model is set to break down.

Although the on-time will have no effect on the lifetime of the SSCB, it does have an impact on the operation of the vessel used as a ferry. By doubling the charging time, the vessel spends less time sailing, meaning fewer people can be transported over time, or it needs to sail faster, which in turn consumes more energy.

5.2 Configuration sensitivity

An important design consideration that has an impact on the B-10 lifetime of the SSCB is the number of components installed on each heatsink. In the base case from the previous chapters, there was only one component per heatsink enduring the full 1000 A charging current through it, which led to relatively high mean temperatures and temperature swings. In reality, mostly modules are used, consisting of multiple identically rated components in parallel to scale up the rating of the module. In this case, identical parallel components are used to evenly distribute the load as described in the Cauer model in Figure 5.5.

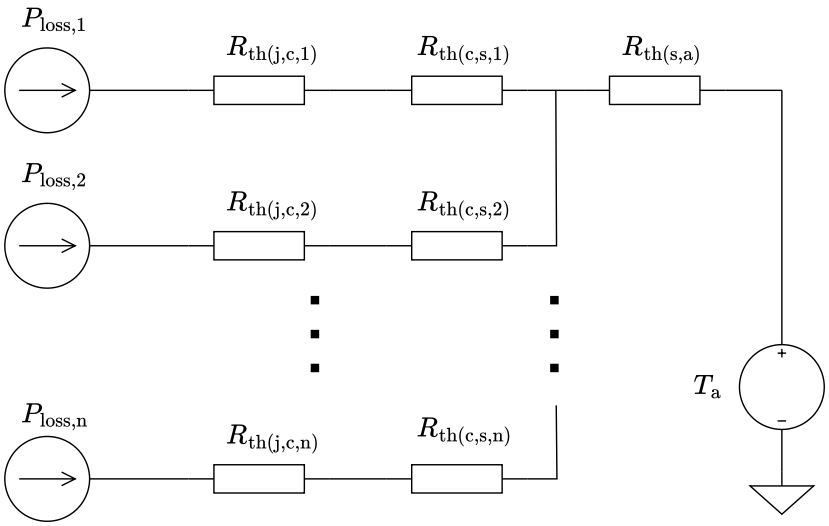

Figure 5.5: Cauer model with additional components n (per module) on a heatsink.

Doing so reduces the thermal stresses experienced by each individual component, which can, in turn, reduce the chance of wear-out failures of each component. The reduction in the junction temperature swing of each individual component is represented in Figure 5.6

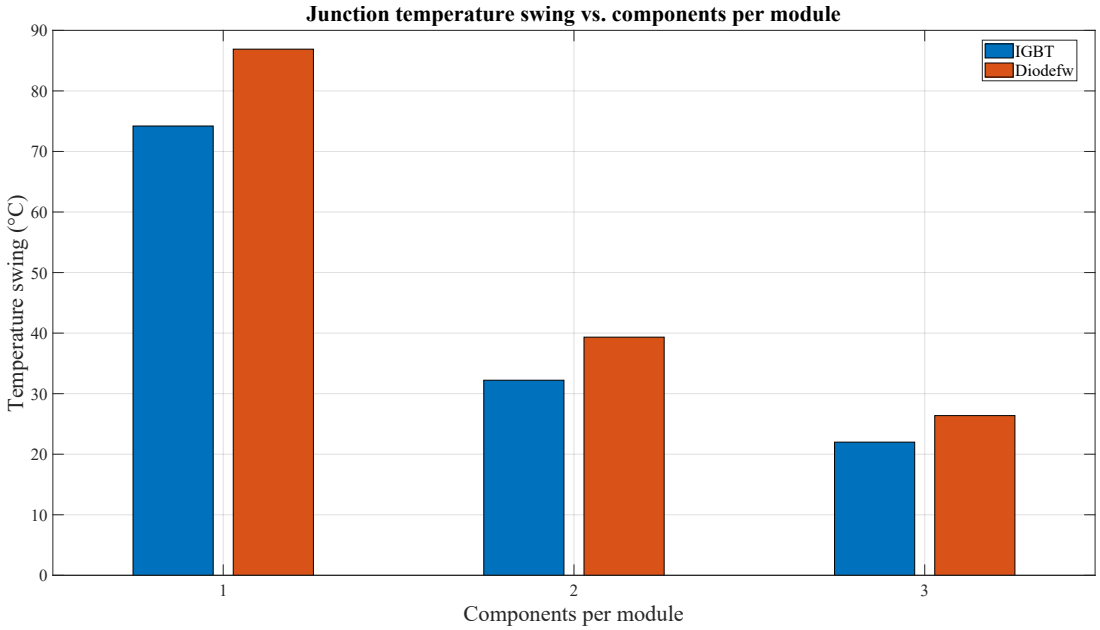

Figure 5.6: The change in junction thermal swing per individual component as a consequence of the load and thus current being shared equally over the other components in the module over the same module heatsink.

However, this comes at the cost of introducing more potential points of failure. Since IGBTs and diodes predominantly fail as a short circuit [54], a single failure can break the SSCB. From a system reliability perspective, this means that the components behave as if they are all arranged in series in a reliability block diagram. For example, with 2 parallel components per module, there would be a total of four forward diodes, four backward diodes and 2 IGBTs. In Table 5.1, this relation between the SSCB lifetime and the number of components per heatsink is shown.

Table 5.1: Increase in SSCB B-10 lifetime as a consequence of additional parallel components to share the load.

Components per module	Nominal B-10 lifetime
1	1
2	31
3	175

Compared to the base case of one single component per heatsink, using a module consisting of two parallel components can increase the lifetime by 31 times. With 3 parallel components, this increases to 175 times, compared to the base case. Nevertheless, this does not imply that increasing the number of parallel components is always beneficial. If the cost of integrating each additional parallel component is a multiple of the component cost, then doubling the number of components effectively doubles the cost per module. Moreover, even though the wear-out failures decrease due to the load sharing between parallel components, the likelihood of failure due to random chance failure mechanisms still persists. With the assumption that each component fails as a short-circuit and is thus essential for the operation of the SSCB, the increase in components can contribute to a higher chance of failure due to the increased amount of failure points.

5.3 Operational parameters sensitivity

The last sort of parameters that can change the lifetime of the SSCB are of the operational type. External factors that are not related to the mission profile of the vessel, nor related to the configuration of the SSCB. One example would be a change in the coolant temperature. Mostly, the cooling system of the ship is a closed-loop system, in which fresh water or a type of liquid coolant is pumped around the devices in need of cooling [55]. After extracting the heat from the devices, this coolant is in turn cooled via a heat exchanger with seawater as the medium. Hence, the minimum coolant temperature depends on the efficiency of the heat exchanger and the seawater temperature. To achieve a lower coolant temperature than the seawater temperature and a more stable coolant temperature required for more sensitive devices such as batteries, an additional cooling system utilising heat pumps to further chill the coolant is needed.

With a difference in the coolant temperature with the designed cooling system in chapter 3, it can be observed that the mean junction temperature of the components changes linearly, as seen in Figure 5.7a. Furthermore, the temperature swing is also noticeably affected by the coolant temperature and the resulting increase in mean temperature. Looking at Figure 5.7b, an increase of 7°C for the IGBT and 5°C for the forward diode between a coolant temperature of 10 and 60 °C is observed. Consequently, the junction temperature of the forward diode reaches its maximum temperature at a coolant temperature around 59°C already, leading to the breakdown of the diode.

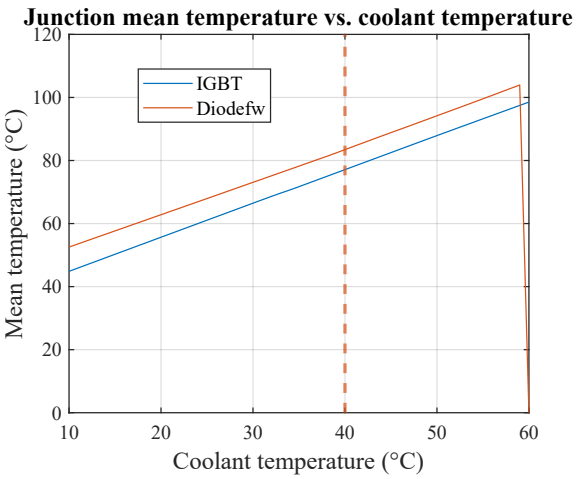

(a) Mean junction temperature of the SSCB components as a function of the coolant temperature.

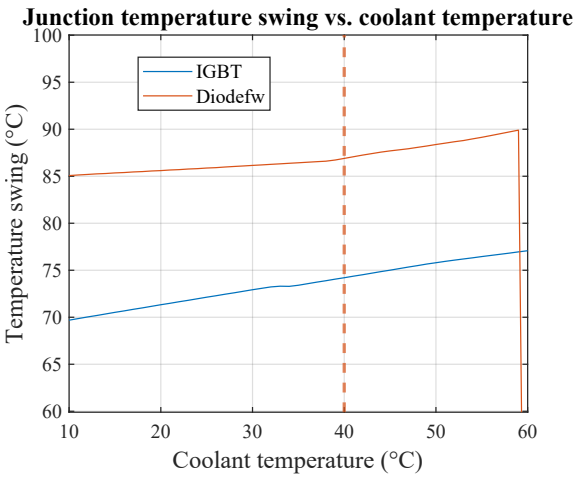

(b) Junction temperature swing of the SSCB components as a function of the coolant temperature.

Figure 5.7: Junction temperature mean and swings of the SSCB components. As the coolant temperature increases, so does the mean temperature and the temperature swing.

The influence of varying coolant temperatures on component lifetime is illustrated in Figure 5.8. A coolant temperature of 20 $°C$, which is half of assumed the base case, results in an approximate 1.4 times increase in lifetime compared to the reference scenario. This highlights the impact that operating conditions, such as ambient seawater temperature, can have on the lifetime of the SSCB. Given the global variability in seawater temperatures, the operating region becomes a marginal factor in SSCB lifetime. While the implementation of active cooling strategies, such as heat pumps, could enable lower coolant temperatures, this would introduce additional energy requirements and operational costs that must be considered.

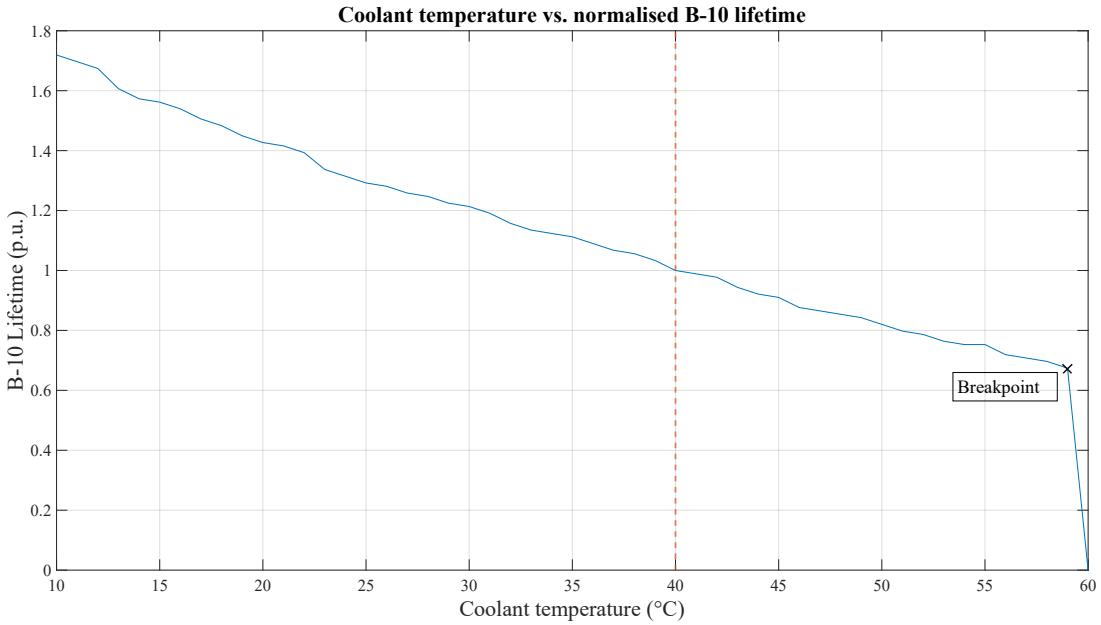

Figure 5.8: Result of the change in SSCB B-10 lifetime due to the coolant temperature. The dashed line indicated the coolant temperature in the base case.

5.4 Summary sensitivity analysis

In summary, each of these changes will have a beneficial effect on the SSCB, either by reducing the thermal swings or by sharing the load and stresses over multiple components. However, each of them also has its respective drawbacks. These are summarised in Table 5.2.

Table 5.2: Summary of the described changes influencing SSCB lifetime

	Benefit	**Drawback**
Bi-directional charging	Maximum of 1.5 times increase lifetime if both sides equally loaded.	Need to have pre-equipped bidirectional charging support on the vessel.
Reduced charging power	Approximate 2 to 3 times increase in lifetime per 100 A reduction in charging current.	Increased charging time inversely proportional to reduction in charging power.
Parallel components	Two components per module for every component in SSCB increase B-10 lifetime already by 31 times.	Expensive; practically second SSCB in parallel.
Reducing coolant temperature	Approximate 1.2 times increase in lifetime per 10°C of coolant temperature decrease.	Coolant temperature dependent on outside water temperature or power of heatpump.

Chapter 6

Electrical Disturbances

In this chapter, the effects of high-frequency noise on the SSCB lifetime compared to the base mission profile are investigated. First, the developed iterative thermal model needs to be altered to a dynamic model, which calculates the junction temperature as a function of time and allows it to follow the small thermal fluctuations as a consequence of short power loss pulses. Secondly, with the obtained dynamic model, the accumulated damage per day is calculated for a range of amplitudes and frequencies.

6.1 Dynamic thermal modelling

In the previous chapters, it was assumed that the power-on duration was adequately long to allow the junction temperature to reach its steady-state value during each power cycle. As a result, it was chosen to calculate the junction temperature via iterative modelling using the capacitor-less Cauer model (Figure 2.5a) as explained in subsubsection 3.4.2 and let the junction temperature rise immediately to its steady state temperature. However, for short transient pulses such as high-frequency sinusoidal noise, due to the thermal inertia (or thermal capacitance) in the device, the junction temperature does not have the time to reach a new steady-state temperature before the noise power cycle has ended. Consequently, dynamic modelling has to be used, which utilises the Foster model. Unlike iterative modelling, dynamic modelling is dependent on the transient thermal impedance characteristics of the component to have a variable thermal impedance based on the on-time of a given power cycle and takes the temperatures of the power device from a previous timestep into account. This enables the model to calculate what the junction temperature should be for each timestep.

6.1.1 Transient thermal impedance

The most significant difference between the iterative model used in chapter 3 and the dynamic model in this chapter is thus the use of transient thermal impedances and the Foster model. In chapter 2, it was explained that the Foster model represents the thermal transient of the whole device, or a part thereof. In this case, only the transient thermal impedance between the junction and case is taken into account, which is given in the datasheets of the selected components [40] [41] as a 4-layer Foster model with the time constant τ and the normalised thermal resistance per layer as seen in Table 6.1.

Table 6.1: Normalised thermal resistances and corresponding time constants of the junction-to-case Foster model for both the IGBT and diode modules.

i	1	2	3	4
$R_\mathrm{i}/R_{\mathrm{th}(j,c)}$	0.0096	0.1893	0.4044	0.3967
$\tau_\mathrm{i}(s)$	0.0001	0.0058	0.0602	0.3512

Using (6.1) the thermal impedance is obtained for the junction-to-case

$$Z_{\mathrm{th(j,\,c)}}(t) = \sum_{i=1}^{n} R_\mathrm{i} \left\{ 1 - \exp\left(\frac{-t}{\tau_\mathrm{i}} \right) \right\} \tag{6.1}$$

This is then plotted as a function of time as shown in Figure 6.1.

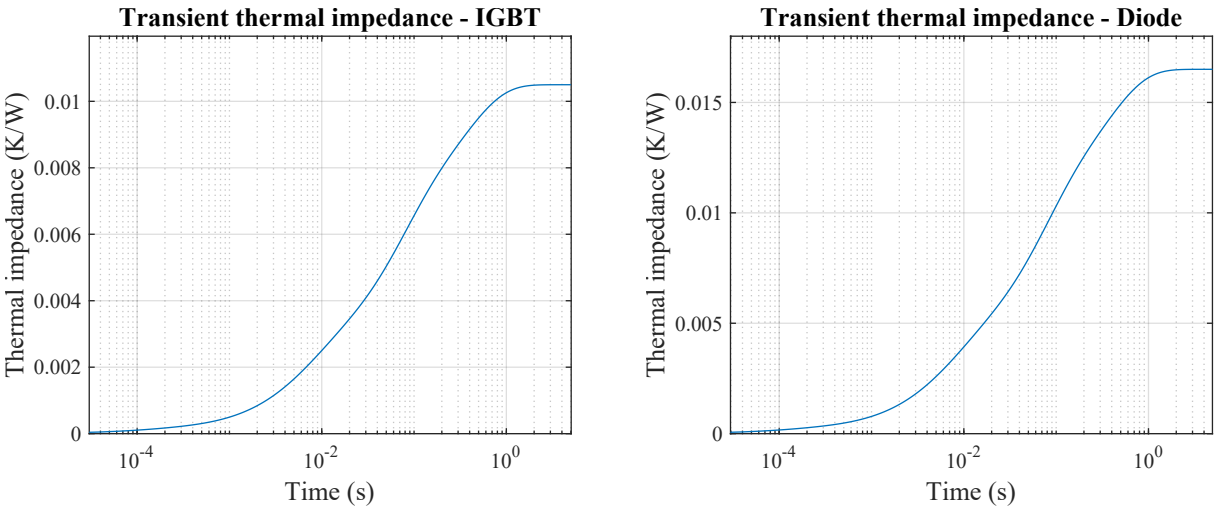

(a) Transient thermal impedance of IGBT [40].

(b) Transient thermal impedance of diode [41].

Figure 6.1: Transient thermal impedances of the IGBT and diode following their respective datasheets.

The sink-to-ambient thermal capacitance, which reflects the thermal inertia of the heatsink, is excluded from the transient thermal model due to the significantly slower time constants involved. The thermal capacitance of a typical heatsink is sufficiently large that its thermal response reaches a steady-state impedance only after approximately 100 seconds [56]. As a result, the heatsink temperature changes due to short thermal fluctuations from the semiconductor junction under a second induced by the noise current, can be assumed to be a negligible amount.

As for the thermal impedance of the case-to-sink, which represents the behaviour of the thermal interface between the case and the heatsink, there is a lack of the thermal capacitance data for it. So, a study such as [57] neglect the thermal capacitance of the interface and model it solely as a thermal resistance. This simplification implies in the Foster model that the thermal interface responds instantaneously to power fluctuations, regardless of their duration, much like the assumption in the iterative model. While such an approach can be acceptable for low-frequency thermal transients, where the junction has sufficient time to heat up to its steady-state value, and the interface temperature is able to track the junction temperature in a coupled manner, it introduces significant errors when applied to high-frequency noise currents. This is due to the junction temperature remaining largely unaffected as a consequence of the limited thermal impedance in such a short time frame (see Figure 6.1). Consequently, this would result in the junction temperature becoming entirely determined by the thermal resistance of the interface, which is an unrealistic scenario [57].

Therefore, it was decided to consider the thermal capacitance of the interface high enough, such that short fluctuations will not influence its temperature, much like the behaviour observed for the heatsink; a method utilised by [29]. While this introduces a degree of error for the junction temperature calculation in the lower range of frequencies, this reduces the calculation errors in the high-frequency noise region. Since the interest in this chapter lies in the high frequencies, this was deemed the better alternative.

In conclusion, the isothermal case temperature that the Foster model of the junction-to-case part sees is the steady-state temperature that is dictated by the thermal resistances of the thermal interface and the heatsink, and the power loss of the noiseless mission profile in chapter 3. Which results in the temperatures in Table 6.2

Table 6.2: Case temperatures that the junction-to-case Foster model experiences.

	Charging	Sailing
IGBT	90.59°C	40°C
Diode	90.13°C	40°C

6.1.2 Noise insertion

To simulate noise, a sinusoidal wave is superimposed over each of the power cycles in a day. With the assumption that the wave is the same for every power cycle at any given moment during the steady-state, only counting the number of thermal cycles in a part of the noise profile would be sufficient to obtain the damage to a component in a day. However, a difference has to be made between the noise during the charging operation and the sailing operation. This is because during the charging operation, the noise oscillates around 1000 A, which causes the noise cycle to oscillate at a higher mean temperature than during the sailing period, wherein the noise oscillates around 0 A, resulting in it oscillating close to the minimum coolant temperature of 40°C. However, that is only if the SSCB were to be closed during the sailing period. If it were open, then there would naturally be no noise current flowing through it.

This oscillation around 0 A gives the implication that the noise current can flow into the "negative" direction. As an example and a starting point from which the dynamic model is developed, a noise of 1000 Hz with an amplitude of 100 A is inserted, as plotted in Figure 6.2 in a 2 ms timeframe.

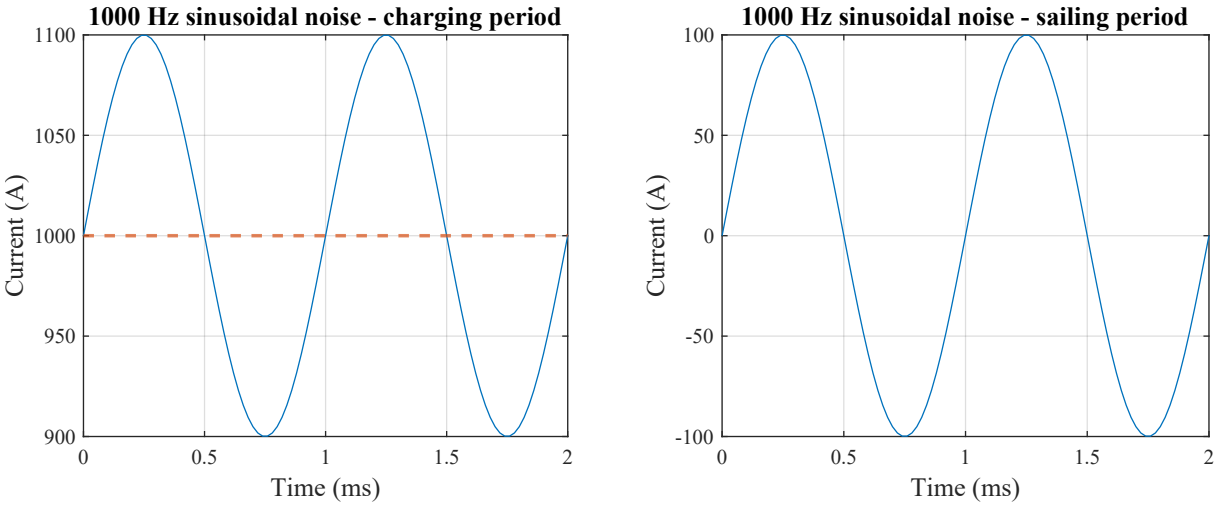

(a) Noise current during the charging period.

(b) Noise current during the sailing period.

Figure 6.2: The resulting current through the SSCB with a 1000 Hz, 100 A noise current added to the base mission profile current during the charging period or the sailing period.

For the IGBT, this means that it will receive half of the amplitude swing but at double the frequency, since the current always flows in one direction. For the diodes, this means that the backward diodes are also utilised during the sailing operation. The currents trough the relevant components are shown in Figure 6.3. It can be seen that due to the alternating and identical pattern at which the forward and backward diode conduct, it can be deduced that the forward and backward diodes will endure the same stresses over a longer period of time. Therefore, for the remainder of the calculations done for the sailing period, only the calculations for the forward-facing diode are shown.

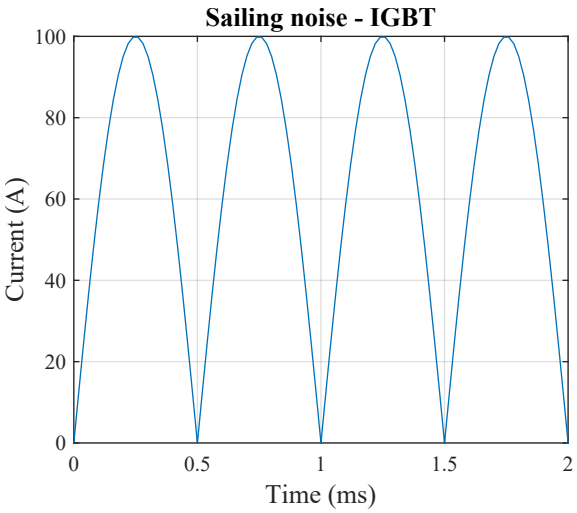

(a) Noise current through IGBT during sailing period.

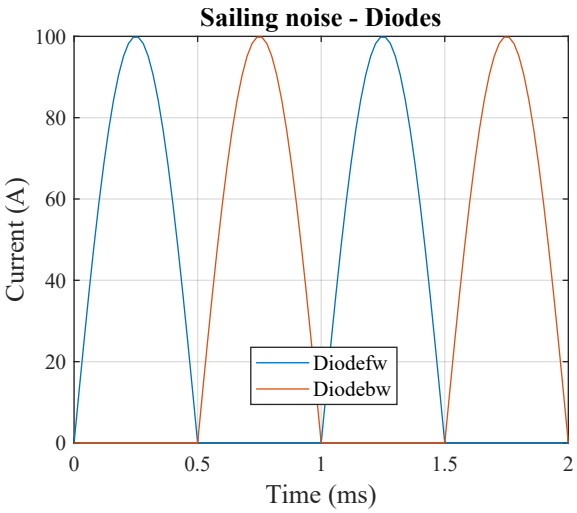

(b) Noise current through diode during sailing period.

Figure 6.3: Noise current through the components during the sailing periods. It is seen that the forward and the backward diode conduct in an alternating pattern from each other.

6.1.3 Power loss with noise

As demonstrated in chapter 3, the junction temperature and power loss are interdependent variables: the power loss is influenced by the junction temperature, while the junction temperature is, in turn, a function of the power loss. Thus, an iterative process was needed to accurately estimate the junction temperature in each instance of time. However, noticeable differences in the estimated junction temperatures between iterations were only observed due to the variation in current during the power cycle was sufficiently large to cause a marginal increase in both the junction temperature and the power loss. This ongoing interaction between the two parameters continued for a few iterations until thermal equilibrium was reached. In the case of the noise cycle, it is to be questioned whether this iterative part of the calculation is needed. The changes in junction temperature as a consequence of solely the noise are namely expected to be too small to have a significant impact on the power loss calculation due to the high frequency of the noise and the transient thermal impedance.

Thus, since the interest lies in the power loss and the temperature fluctuation as a consequence of the noise in the steady-state periods of the base mission profile, the steady-state junction temperatures calculated in Table 3.3 are used to estimate the power losses for now. This results in the following plots in Figure 6.4.

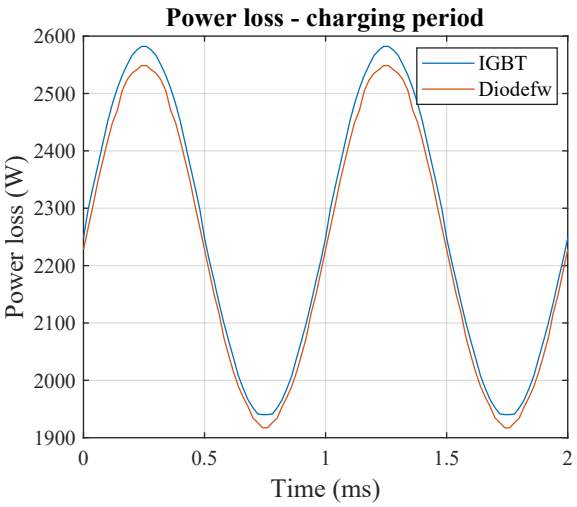

(a) Power losses of the components as a function of time during the charging period.

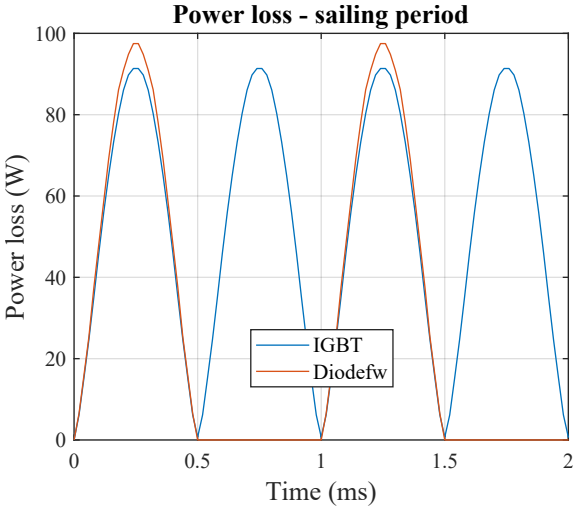

(b) Power losses of the components as a function of time during the sailing period.

Figure 6.4: Power losses of the components as a function of time during the charging period and the sailing period.

These obtained losses are merely the conduction losses. However, with the introduction of changes in the current direction during the sailing period, switching losses have to be considered for the diode, especially at higher frequencies. To see the impact of the switching losses, the simulation model of the SSCB in Figure 3.3 is used with some alterations. Namely, the DC-voltage source is changed with an AC voltage source representing the 1000 Hz noise signal, which in turn generates a current close to 100 A peak-to-peak. Next, the values related to the switching losses of the diode are filled in, which are the reverse recovery time t_{rr}, peak recovery current I_{rrm} and the reverse recovery charge Q_{rr}. These values are summarised in Table 6.3 and obtained from the datasheet of the diode [41].

Table 6.3: Switching loss related values at 25°C junction temperature

	$t_{rr}(\mu s)$	$I_{rrm}(A)$	$Q_{rr}(\mu C)$
Diode	0.95	1800	1200

As a result, the behaviour of a single diode during switch-off is obtained as in Figure 6.5.

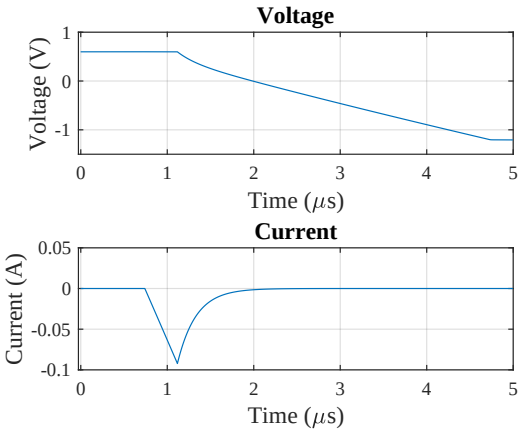

(a) Voltage and current values of the diode at the moment of turn-off.

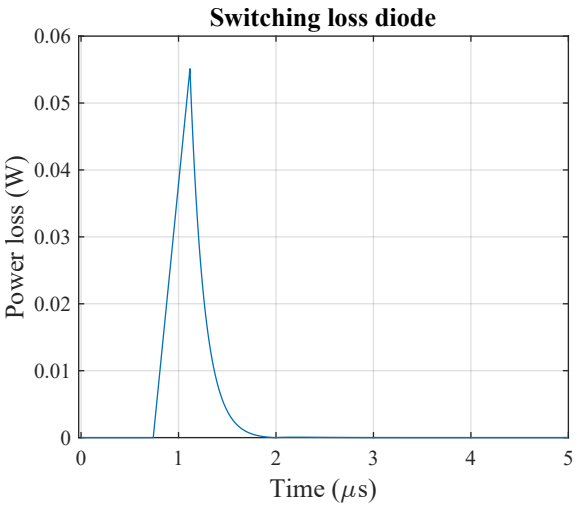

(b) Power loss of the diode at the moment of turn-off.

Figure 6.5: Voltage, current and power loss figures of the diode during the turn-off period.

It is seen that the switching loss per turn-off cycle is only a maximum of 55 mW and only present for about 1.2 μs. In comparison with the conduction losses, which are a maximum of around 90 W to 100 W and present for a much longer period of 0.5 ms, it can be concluded that the switching losses are not of importance. The low switching loss is mainly due to the low voltages at which the diode has to change from forward-bias to reverse-bias. This low voltage can be explained by looking at the configuration of the SSCB (Figure 3.3), when the current reverses, the diode that switches to reverse-bias needs to only endure the forward voltage of the diode and IGBT branch in parallel, which are both 0.6 V, and explains the negative voltage of merely 1.2 V. This in conjunction with the relative low maximum reverse recovery current, yield a low power loss per turn-off.

6.1.4 Thermal model with noise

With the obtained power losses, the temperature fluctuations can be obtained. Unlike in chapter 3, where the junction temperature was simply obtained by multiplying the power losses with the thermal resistances, the junction temperature calculation with a variable thermal impedance is more complex due to the influence of time dependency. As described in chapter 2, it needs to be calculated with a convolution between the power loss and the derivative of the thermal impedance. In this case, where the transient thermal impedance is only applicable for the area between the junction and the case, and with ambient temperature T_a as the fixed temperature T_c, this yields the junction temperature equation in (6.2).

$$T_j(t) = T_c(t) + \left(P_{loss}(t) * \frac{d}{dt} Z_{th(j,\,c)}(t) \right) \tag{6.2}$$

To validate whether the result of this equation is correct, a 5-second-long dummy power profile of the IGBT is made with a 100W power loss for the first 2.5 seconds before falling back to 0 W loss for the remainder of the time. Assuming that $T_c = 100°C$, the results are shown in Figure 6.6

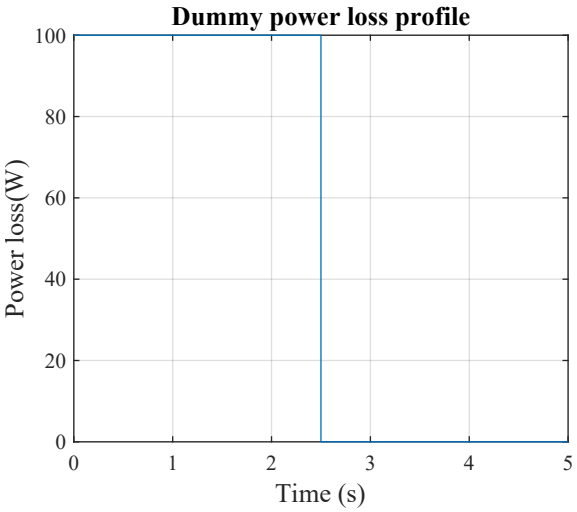

(a) Dummy power profile.

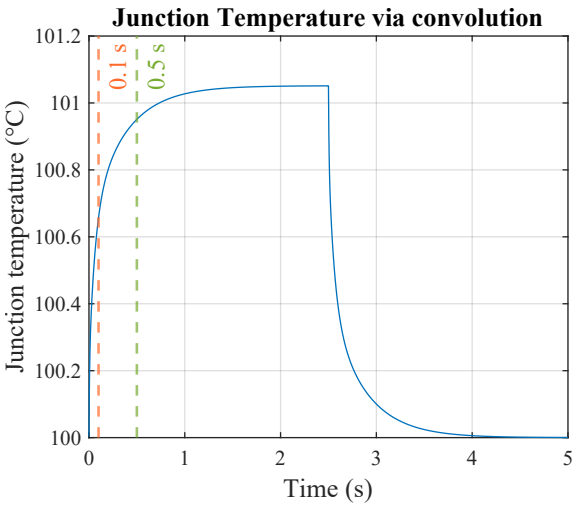

(b) Junction temperature as a consequence of dummy power profile.

Figure 6.6: Validation of the dynamic model using the parameters of the IGBT and a case temperature of $100°C$. Using the dummy power profile as input, it is seen that the resulting junction temperatures match the junction temperature calculations with the time-dependent thermal transient impedance of the IGBT in Figure 6.1a.

It is to be expected that at $0.1\,s$ of the power pulse, the thermal impedance of the IGBT is $Z_{\text{th(j,c)}} = 0.0065K/W$. This would theoretically lead to an increase of $100 \cdot 0.0065 = 0.65°C$ at that moment, which coincides with what is seen in Figure 6.6b. At $0.5\,s$, $Z_{\text{th(j,c)}} \approx 0.009K/W$, which should result in $100 \cdot 0.009 = 0.9°C$ increase in temperature. Again, this coincides with the result in Figure 6.6b. The second part of the dummy profile, where the power drops to 0 W, shows the same behaviour as the first part, but vertically mirrored, representing the gradual cooling of the junction following the thermal impedance. Thus, it can be concluded that the model behaves as it is expected.

Applying the thermal model to the power loss profile in Figure 6.4 with the case temperature described in Table 6.2, results in the plots in Figure 6.7, which represent the output of the junction-to-sink Foster model.

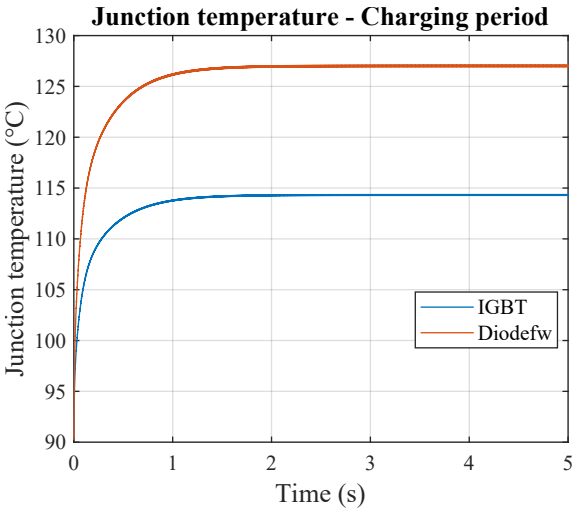

(a) Output of Foster model during the charging period with $T_{\text{c, IGBT}} = 90.59°C$ and $T_{\text{c, diode}} = 90.13°C$

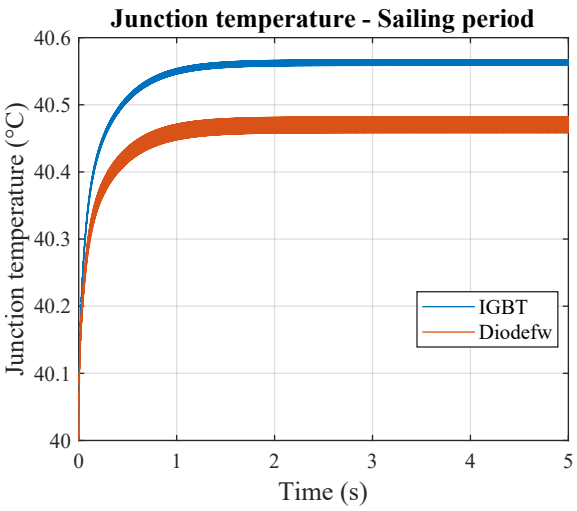

(b) Output of Foster model during the sailing period with $T_{\text{c, IGBT}} = 40$ and $T_{\text{c, diode}} = 40$.

Figure 6.7: Output of the Foster models for both the charging and sailing period.

It is seen that the output of the junction temperature during the charging period coincides with the iteratively calculated junction temperatures in Table 3.3, with the initial rise in temperature from around 90°C due to the main 1000 A current. However, the interest lies only in the changes in temperature due to the power fluctuations during the steady-state period. To observe solely the influence of electrical noise on the junction temperature, the focus is on the time period during which the junction has reached, or is approaching, its maximum thermal impedance. This condition can be assumed to occur at approximately 4 seconds, looking at Figure 6.1. A zoomed-in view from the 4-second mark in Figure 6.7 reveals the temperature fluctuations induced purely by the noise, as illustrated in Figure 6.8.

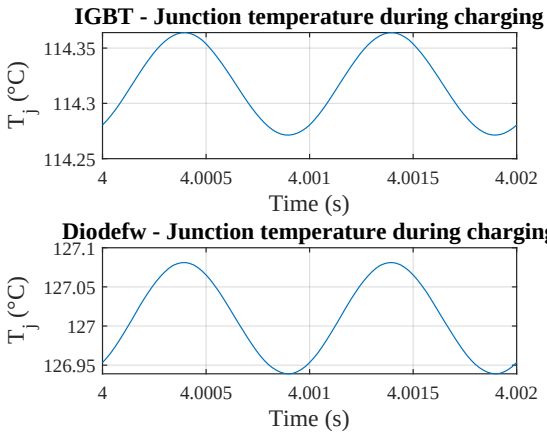

(a) Junction temperature fluctuations during the charging period.

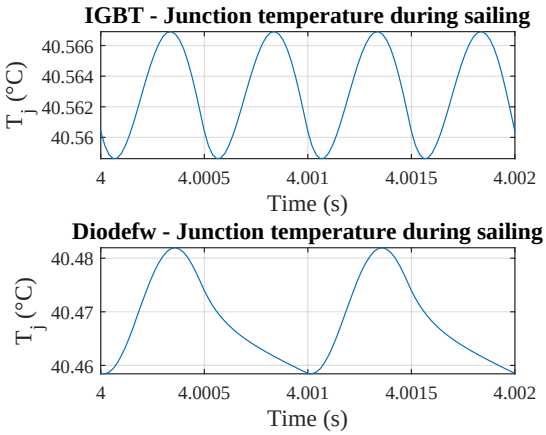

(b) Junction temperature fluctuations during the sailing period.

Figure 6.8: Junction temperature fluctuations as a consequence of the noise current for both the charging period and the sailing period.

From it, the thermal fluctuations as a consequence of the noise can be observed as described in Table 6.4.

Table 6.4: Temperature swing as a consequence of noise current.

	Charging	Sailing
IGBT	0.0927°C	0.00830°C
Diode	0.142°C	0.0235°C

6.1.5 Iterative calculation

The initial assumption that the thermal swing as a consequence of high-frequency noise is too small to noticeably affect the power loss calculation seems to be correct, with the largest temperature swing due to the 1000 Hz, 100 A noise profile belonging to the diode during charging, with a value of 0.142°C. Looking at the zoomed in version of the power loss of the diode in Figure D.1, around 1000 A, a 50°C increase in temperature, would only affect the power loss by around 120 W. Assuming linear scaling, this would mean that the 0.142°C peak-to-peak temperature swing, only affects the power loss by 0.34 W, which in conjunction with the already low thermal impedance of the diode at 1000 Hz, would result in a negligible amount which is not worth the reduction in computational speed due to the iterative calculation process.

6.1.6 Damage contribution

With the obtained thermal swings, the same method as described in chapter 4 is used to obtain the damage per day done to the components. First, a segment of the temperature profile of when the components swing around their steady-state temperature is taken, which was chosen as a one-second period from 4 to

5 seconds in the charging period and the sailing period from Figure 6.7. These one-second temperature fluctuations are then put in the rainflow counting algorithm, and the data in Table 6.5 is obtained.

Table 6.5: Output of the rainflow counting for the 100 A, 1000 Hz noise profile.

	$N_{c,h}$	$\Delta T_{j,h}(°C)$	$T_{jmean,h}(°C)$	$T_{jmin,h}(°C)$	$t_{on,h}(ms)$
IGBT (Charging)	1000	0.0927	114.318	114.225	0.5
IGBT (Sailing)	2000	0.0083	40.563	40.554	0.28
Diode (Charging)	1000	0.142	127.010	126.868	0.5
Diode (Sailing)	1000	0.0235	40.470	40.447	0.24

Then, by filling in these values in the CIPS with the correction lifetime estimation model, the number of cycles until failure is obtained. First, the number of seconds during which the ship is in charging mode is needed, which is roughly $16\,charging\,cycles \cdot 10\,min \cdot 60\,seconds = 9600\,s$. As for the sailing time, that number amounts to 48000 seconds. Calculating the damage per second by dividing the number of cycles in a second by the cycles to failure, as in (4.1), and multiplying it by the number of seconds spent charging or sailing, the results in Table 6.6 are obtained.

Table 6.6: Results from the CIPS with correction per component as an effect of noise. The backward diode receives the same damage per day as the forward diode during sailing operation.

	$N_f(cycles)$	$D_{acc\text{-}day}(-)$
IGBT (Charging)	$1.014 \cdot 10^{18}$	$9.478 \cdot 10^{-12}$
IGBT (Sailing)	$9.402 \cdot 10^{22}$	$1.021 \cdot 10^{-15}$
IGBT (Total)	N/A	$9.479 \cdot 10^{-12}$
Diode (Charging)	$1.384 \cdot 10^{17}$	$6.946 \cdot 10^{-11}$
Diode (Sailing)	$9.465 \cdot 10^{20}$	$5.072 \cdot 10^{-14}$
Diode (Total)	N/A	$6.951 \cdot 10^{-11}$

Comparing the total damages per day received due to noise with the damage per day from the base mission profile, which was $3.210 \cdot 10^{-4}$ for the IGBT and $6.559 \cdot 10^{-4}$ for the diode, the normalised damage become $2.953 \cdot 10^{-8}$ and $1.060 \cdot 10^{-7}$ for the IGBT and diode respectively. The damage inflicted by the noise is thus many magnitudes lower than the damage inflicted by the temperature fluctuations of the base mission profile, meaning that for a noise current of 1000 Hz and an amplitude of 100 A, the damage inflicted is negligible. Moreover, it is observed that the damage received from the sailing period is 3 orders of magnitude lower than the damage received during the charging period, even though the sailing period is a longer period of time, meaning that almost all of the damage received from noise is from the charging period.

It is expected that the damage inflicted by noise can rise as the noise frequency gets lower, since the junction is given more time to heat up or cool down. The damage can also rise when the noise current amplitude gets higher, leading to faster temperature rises and drops. To see the relation of these changes to the damage on the components with respect to the damage from the base mission profile, a plot showcasing the normalised damage from different noise amplitudes vs the frequency is plotted in Figure 6.9.

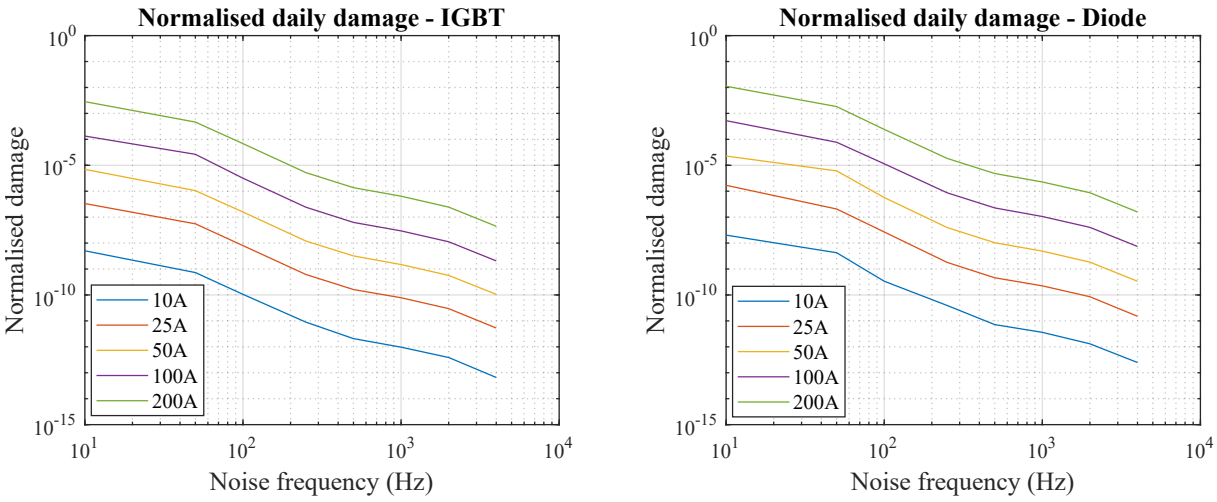

(a) Normalised daily damage of the IGBT.

(b) Normalised daily damage of the forward diode.

Figure 6.9: Normalised daily damage of the relevant components compared to the daily damage.

It can be observed that the normalised damage is inversely proportional to the noise frequency, with approximately a two-order-of-magnitude reduction for every one-order-of-magnitude increase in noise frequency. On the other hand, an increase in noise current amplitude is proportional to the increase in damage, with about a 4.5 order-of-magnitude increase for each one-order-of-magnitude increase, as seen between 10 A and 100 A.

The maximum additional damage that the IGBT and (forward) diode can receive from the testing parameters is thus at a noise frequency of 10 Hz, with a 200 A amplitude. This resulted in a normalised daily damage of $2.841 \cdot 10^{-3}$ times for the IGBT and $1.11 \cdot 10^{-2}$ times for the forward diode. The backwards diode is, as stated before, only active during the sailing period and will thus only receive damage during that period. From the output of the model, this resulted in a daily damage of $5.172 \cdot 10^{-8}$. Since the backwards diode was not active in the entire base mission profile from chapter 4, it is not possible to give a normalised damage compared to the backwards diode. However, to give a perspective of how much impact this has, by normalising it with the forward diode damage, this would amount to a normalised damage contribution of $7.885 \cdot 10^{-5}$, which is about a 100 times smaller than the damage received during the charging, in line with the ratio described at a higher frequency of 1000 Hz in Table 6.5.

From Figure D.2 and Figure D.3, it is seen that for both components the biggest thermal swing across all frequencies, noise amplitudes and operational periods, is still below a $30°C$ swing, in the region at which the CIPS model is known to start to overestimate the damage to components [50]. Consequently, the relatively small normalised damage values presented in Figure 6.9a and Figure 6.9b already represent the maximum ratio between the noise damage and the base mission profile damage.

Applying this knowledge to DC bus systems in marine applications, which are subjected to differential noise currents from converters in the system or the shore charger from the charging input, it is seen that the amplitude of these noises should be a maximum of 0.75% of the nominal current on the DC-bus at 10 Hz or 3% at 5 kHz following the IEC 61851-23-3 standard [58], which amounts only to a 7.5 A or 30 A amplitude in noise current through the SSCB. Furthermore, these ripples are in the kHz range following the switching frequency of the converters in the SPS, which, from measurements on a practical vessel in Figure 2.7 or Figure 2.6, are roughly multiples of 4 to 5 kHz. In conclusion, by observing the results in Figure 6.9, the additional damage from the electrical disturbances on the DC-bus to the SSCB components compared to the main mission profile is negligible.

Chapter 7

Conclusion and future work

This Master's thesis has investigated the influence of various mission profiles related stresses within the shipboard power system on the lifetime of an SSCB intended for use as a bus tie in a radial ship power system configuration. The results provide a basis for quantifying how modifications in the mission profile, SSCB configuration, or operational parameters affect the expected lifetime relative to a designed base case scenario, which is to utilise the SSCB to transfer 1000 A from one charging input to the battery on the other side of the vessel 16 times a day, while no power is transferred during the sailing period. By establishing these relationships, the findings can provide assistance in design and operational decisions which indirectly influence SSCB reliability in practical marine applications. The answers to the four research questions in chapter 1 are given to conclude this thesis.

1. *Which considerations should be taken into account when designing the SSCB?*

   To design an SSCB model representing a practical SSCB that could be used in the pre-defined use-case, the first consideration was the selection of the SSCB topology. For the base case, optimally, the RB-IGCT topology is selected to minimise power losses and the consequent heat generation. However, it was found that due to the novelty of the device, a topology which utilises more common and mature components, such as the IGBT, and which reflects commercially available SSCBs, was preferred to obtain more reference data and selection in available voltage and current ratings. The second consideration is based on the nominal voltage and current ratings, which are recommended to be at least 54% and 10% above their respective operational values to ensure a safe blocking margin after the SSCB has opened. The next consideration concerns limiting the peak current through the current interrupter during fault interruption. This peak current is dictated by the selected switch its turn-off time and the power system inductance. If the power system inductance is insufficient to prevent the current from exceeding the peak current rating (mostly defined as twice the nominal rating) of the components, additional inductance must be inserted in the current path of the current interrupter of the SSCB to limit the current rise, which was 10μH in this design. The following consideration is the design of the voltage clamping circuit, whose purpose is to protect the switch from overvoltages. The MOV circuit was selected as a suitable component for this protection, mainly due to its simplicity and bi-directionality. Lastly, the cooling of the components in the SSCB should be based on the amount of power losses from the components and their respective safe operating temperatures. For the base case, it was found that forced air cooling was not enough to keep the junction temperatures of the selected components under their respective maximum temperatures. Thus, a water cooling solution was selected with a 7.5 K/kW thermal resistance.

2. *How to obtain a lifetime estimation of the SSCB as a consequence of thermal fatigue?*

   To model the SSCB lifetime solely as a consequence of thermal-mechanical fatigue, mission profile analysis is used. First, a power loss model needs to be made from the VI-curve given in the datasheets of the chosen components. Since the SSCB is not expected to switch often due to its functionality as an emergency circuit breaker, only the conduction losses are taken into account. Then, assuming the mission profile power-on-time is large enough such that the junction temperatures of the components always reach their steady-state temperature, the Cauer model without

the thermal capacitance representing thermal inertia is sufficient to obtain the junction temperature profile over the course of a day. Next, the component reliability of a single component is obtained via multiple steps. The first of which is the cycle counting, which utilises the rainflow counting algorithm to differentiate different classes of thermal cycles in the temperature profile. The output of this algorithm provides information regarding the cycle count, temperature swing, mean temperature, minimum temperature and the power-on-time per class, all of which are used in the lifetime estimation models. It was concluded that the CIPS model was the preferred lifetime model compared to the LESIT and "Zhou" model in this sensitivity analysis due to its relatively low cycle-to-failure prediction and low sensitivity to temperature swings in the defined mission profile with a fixed minimum temperature, giving results reflecting the minimum sensitivity. However, a correction factor is applied to the CIPS model to reduce the unrealistic impact of long (>60 s) and short (<0.1) power-on times. This cycle-to-failure estimation is then repeated with varying model parameters β following a 5% deviation with a Monte Carlo analysis to simulate estimation uncertainties of the lifetime model. After transforming them from cycle-to-failure to lifetime in years, this results in a probability mass function which, once fitted into a Weibull curve and subtracted from 1, results in the reliability curve representing the percentage of the number of components operational in the given sample size at an instance of time. Having repeated this process for all the components in the SSCB and assuming that all components are crucial for the operation of the SSCB, the reliability curves are multiplied with each other, resulting in the reliability curve of the SSCB in the defined base case as a consequence of thermal fatigue. The B-10 lifetime, which ideally reflects the time at which 10% of the components have failed due solely to wear-out failures, is noted to help interpret the results. These are obtained as 4.78 years for the IGBT, 2.29 years for the forward diode and 1.78 years for the SSCB.

3. *What is the sensitivity of SSCB lifetime due to changes in the mission profile, SSCB configuration and operational parameters?*

   Four changes that impact the SSCB lifetime are investigated, which are: Making use of bidirectional charging, changing the charging power while increasing the charging time, load sharing by parallel components, and the coolant temperature used. By normalising the obtained lifetime with the lifetime from the base case, the focus lies on the sensitivity of the lifetime to the aforementioned changes. For the bi-directional charging change, it was found that by equally charging the vessel from both sides instead of only from one side during the daily mission profile, an increase of 1.5 times in SSCB lifetime could be achieved. Next, the change in the amount of power flowing through the SSCB during the charging operation has a significant effect on the junction temperature swings. Each 100 A difference would result in roughly a $12°C$ difference in temperature swing. Consequently, this results in a change in lifetime difference growing exponentially 2 to 3 times per 100 A as seen in Figure 5.4. Sharing the current load between identical components on the same heatsink reduced the thermal swings, with a reduction almost inversely proportional to the number of components in parallel. By assuming that each component fails as a short-circuit and is thus essential for the operation of the SSCB, a lifetime increase of 31 times and 175 times is present when 2 and 3 identical components, respectively, are placed in parallel. Lastly, it was concluded that changes in coolant temperature amount to almost a linear relation with the lifetime, with a $10°C$ reduction in coolant temperature, resulting in a 10% increase in lifetime per $5°C$. Each of these changes influencing the SSCB lifetime has its own drawbacks though, meaning that implementing changes beneficial for the SSCB potentially has other implications on the system-level operation.

4. *To what extent does electrical noise have an impact on the solid state circuit breaker reliability compared to the mission profile?*

   To estimate the impact on the lifetime of the electrical noise through the SSCB in comparison to

the mission profile, a dynamic model was designed to take thermal capacitance into account, which causes the thermal impedance of a component to be a function of time. By overlaying a 1000 Hz, 100 A sine wave into the base mission profile, an exaggerated common-mode or differential mode noise current through the SSCB is simulated. During the sailing period, the noise currents will also fluctuate in the negative direction, which will frequently turn the diodes on and off and induce switching losses. However, it was found that these switching losses are negligible compared to the conduction losses. To isolate the influence of noise on the lifetime, a one-second period during the charging or sailing operation in which the steady-state temperature is reached as a consequence of the mission profile is taken for analysis. It was found that during the charging operation, the noise would only amount to $0.0927°C$ and $0.142°C$ of junction temperature swing for the IGBT and diode, respectively. During sailing operation, it amounts to $0.0083°C$ and $0.0235°C$ for the IGBT and diode, respectively. These temperature swings eventually amount to additional damage to the components, which are 7 to 8 orders of magnitude lower than the damage done due to the mission profile. By increasing the noise amplitude to 200 A and decreasing the frequency to 10 Hz, the components will have a higher junction temperature swing. However, it is seen that the damage contribution only increased to about a hundredth of the mission profile damage, meaning that the contribution of noise on the wear-out failure mechanisms due to thermo-mechanical fatigue is negligible for the considered use case.

What is the impact of changes in mission profile and CM/DM noise on the lifetime of a solid-state circuit breaker as a bus tie in a DC ship power system?

In line with the previous results, variations in the charging current, corresponding to changes in the maximum stress within the mission profile, have the most significant impact on the SSCB lifetime, while having a relatively minor drawback of a varying charging period. The bi-directional charging and changes in the coolant temperature were shown to have a relatively low impact on the lifetime. Load sharing between parallel components in a module significantly increased the lifetime, but at a cost of basically investing in a second SSCB. Concerning the impact of noise on SSCB lifetime with respect to the damage done by the mission profile, it can be concluded that high-frequency noise, such as the common-mode and differential-mode noise, has a negligible effect on the lifetime of the SSCB when solely focusing on wear-out mechanisms due to thermal-mechanical fatigue.

7.1 Future work

Given the numerous design choices made in the SSCB model and the reliability model, there remains a considerable number of alternative scenarios, each influencing the SSCB lifetime differently. Future research on SSCB lifetime sensitivity could therefore focus on the following topics:

- In chapter 3, the rectifier-assisted topology was selected due to the availability of data concerning the components in the device to ensure a reliable modelling process. However, a more optimal topology would have been the topology utilising two anti-parallel RB-IGCTs, since these are specifically designed to have lower conduction losses and to have inherent reverse current blocking capabilities without the need for additional diodes. Furthermore, since it only uses two components, there are fewer points of failure, meaning a potential increase in reliability. However, further research should be done on a suitable lifetime estimation model specifically for this component, since the mentioned lifetime models in this thesis were derived from testing data with standard power IGBT and diodes.
- In chapter 5, it was always assumed that during the sailing period, there is no current through the SSCB, leading to it dropping to the coolant temperature in between the charging periods and causing relatively big temperature swings. To reduce these temperature swings, the SSCB could be kept warm by sending some power through it during the sailing period. In the fully electric

ship power system of this thesis, to obtain consistent power sharing during sailing, one of the batteries would have to be drained more quickly, which generates more heat. Furthermore, one of the batteries would also need to store more energy per cycle, increasing the swing in state-of-charge, severely affecting its own lifetime [59]. Consequently, these changes to improve SSCB are not feasible in this particular system configuration. However, in a hybrid configuration where a generator is supplying power to the DC grid via a converter, this can be a positive change with respect to SSCB lifetime at a lower cost.

- In chapter 5, load sharing between identical components was discussed. These components were assumed to fail in a short circuit, such that if one component fails, the entire SSCB fails. However, by selecting components that fail in an open circuit, redundancy can be applied to the component module. Then, when one of the components in parallel fails, the remaining functioning components in the module will take over the load of the failed component. This application of redundancy results in a need for a model, in which a variable Weibull fit needs to be applied to accommodate the change in α and β parameters sometime during the operational lifetime of the SSCB.
- In chapter 6, it was concluded that the noise current, as a consequence of CM and DM noise, has no impact on the lifetime of the components inside the current interrupter (IGBT, diode) of the SSCB as a consequence of thermal fatigue. However, no parasitic resistances were modelled inside the components of the SSCB, meaning that in practice, there could be some CM current flowing through the more sensitive parts of the SSCB, such as the gate drivers. By investigating the impact on the lifetime of these more sensitive control parts of the SSCB, whether as a consequence of wear-out failures or random chance failures, a better understanding could be obtained about the impact of noise on the SSCB lifetime.

References

[1] R. Rodrigues, Y. Du, A. Antoniazzi, and P. Cairoli, "A Review of Solid-State Circuit Breakers," *IEEE Trans. Power Electron.*, vol. 36, pp. 364–377, Jan. 2021.

[2] Damen Research, Development and Innovation B.V., *Damen shipyards internal measurement*, Jan. 2025.

[3] S. Peyghami, H. Wang, P. Davari, and F. Blaabjerg, "Mission-Profile-Based System-Level Reliability Analysis in DC Microgrids," *IEEE Transactions on Industry Applications*, vol. 55, pp. 5055–5067, Sept. 2019. Conference Name: IEEE Transactions on Industry Applications.

[4] X. Zhou, Z. Xin, Z. Wu, and K. Sheng, "Statistical Analysis of Power Semiconductor Devices Lifetime Test and Lifetime Prediction," *IEEE Journal of Emerging and Selected Topics in Power Electronics*, vol. 13, pp. 348–357, Feb. 2025.

[5] S. Peyghami, P. Palensky, M. Fotuhi-Firuzabad, and F. Blaabjerg, "System-level design for reliability and maintenance scheduling in modern power electronic-based power systems," *IEEE Open Access Journal of Power and Energy*, vol. 7, 11 2020.

[6] MathWorks, "rainflow - matlab." `https://nl.mathworks.com/help/signal/ref/rainflow.html`, 2024.

[7] R. Amro, J. Lutz, and A. Lindemann, "Power cycling with high temperature swing of discrete components based on different technologies," in *2004 IEEE 35th Annual Power Electronics Specialists Conference*, vol. 4, pp. 2593–2598 Vol.4, June 2004. ISSN: 0275-9306.

[8] R. Bayerer, T. Herrmann, T. Licht, J. Lutz, and M. Feller, "Model for Power Cycling lifetime of IGBT Modules - various factors influencing lifetime," in *5th International Conference on Integrated Power Electronics Systems*, pp. 1–6, Mar. 2008.

[9] S. Yang, D. Xiang, A. Bryant, P. Mawby, L. Ran, and P. Tavner, "Condition Monitoring for Device Reliability in Power Electronic Converters: A Review," *IEEE Transactions on Power Electronics*, vol. 25, pp. 2734–2752, Nov. 2010.

[10] C. Xu, Z. Yu, Z. Chen, B. Zhao, Z. Wang, C. Ren, and R. Zeng, "Comprehensive Analysis and Experiments of RB-IGCT, IGCT With Fast Recovery Diode and Standard Recovery Diode in Hybrid Line-Commutated Converter for Commutation Failure Mitigation," *IEEE Transactions on Industrial Electronics*, vol. 70, pp. 1126–1139, Feb. 2023.

[11] R. Rodrigues, T. Jiang, Y. Du, P. Cairoli, and H. Zheng, "Solid state circuit breakers for shipboard distribution systems," in *2017 IEEE Electric Ship Technologies Symposium (ESTS)*, pp. 406–413, Aug. 2017.

[12] F. Agostini, U. Vemulapati, D. Torresin, M. Arnold, M. Rahimo, A. Antoniazzi, L. Raciti, D. Pessina, and H. Suryanarayana, "1MW bi-directional DC solid state circuit breaker based on air cooled reverse blocking-IGCT," in *2015 IEEE Electric Ship Technologies Symposium (ESTS)*, (Old Town Alexandria, VA, USA), pp. 287–292, IEEE, June 2015.

[13] P. Cairoli, R. Rodrigues, U. Raheja, Y. Zhang, L. Raciti, and A. Antoniazzi, "High Current Solid-State Circuit Breaker for safe, high efficiency DC systems in marine applications," in *2020 IEEE Transportation Electrification Conference & Expo (ITEC)*, pp. 936–941, June 2020. ISSN: 2377-5483.

[14] U. Vemulapati, M. Rahimo, M. Arnold, T. Wikstrom, J. Vobecky, B. Backlund, and T. Stiasny, "Recent advancements in IGCT technologies for high power electronics applications," in *2015 17th European Conference on Power Electronics and Applications (EPE'15 ECCE-Europe)*, (Geneva), pp. 1–10, IEEE, Sept. 2015.

[15] J. Zhu, Q. Zeng, X. Yang, M. Zhou, and T. Wei, "A Bidirectional MVDC Solid-State Circuit Breaker Based on Mixture Device," *IEEE Transactions on Power Electronics*, vol. 37, pp. 11486–11490, Oct. 2022. Conference Name: IEEE Transactions on Power Electronics.

[16] E. Haugan, H. Rygg, A. Skjellnes, and L. Barstad, "Discrimination in offshore and marine dc distribution systems," in *2016 IEEE 17th Workshop on Control and Modeling for Power Electronics (COMPEL)*, pp. 1–7, June 2016.

[17] L. M. Levinson and H. R. Philipp, "The physics of metal oxide varistors," *Journal of Applied Physics*, vol. 46, pp. 1332–1341, Mar. 1975.

[18] Shaoyong Yang, A. Bryant, P. Mawby, Dawei Xiang, Li Ran, and P. Tavner, "An Industry-Based Survey of Reliability in Power Electronic Converters," *IEEE Transactions on Industry Applications*, vol. 47, pp. 1441–1451, May 2011.

[19] R. Wu, F. Blaabjerg, H. Wang, M. Liserre, and F. Iannuzzo, "Catastrophic failure and fault-tolerant design of IGBT power electronic converters - an overview," in *IECON 2013 - 39th Annual Conference of the IEEE Industrial Electronics Society*, pp. 507–513, Nov. 2013. ISSN: 1553-572X.

[20] H. Wang and F. Blaabjerg, "Reliability of Capacitors for DC-Link Applications in Power Electronic Converters—An Overview," *IEEE Transactions on Industry Applications*, vol. 50, pp. 3569–3578, Sept. 2014.

[21] Nia, Amsc, *Reliability prediction of electronic equipment*, 1995.

[22] M. Ahmadi, F. Kardan, A. Shekhar, and P. Bauer, "Reliability Assessment of Modular Multilevel Converters: A Comparative Study of MIL and Mission Profile Methods," in *CIPS 2024; 13th International Conference on Integrated Power Electronics Systems*, pp. 476–482, Mar. 2024.

[23] D. Butnicu, "Comparative Study for DC-DC Converter Output Bank's Reliability Evaluation Using Prediction Standards MIL-HDBK-217F vs. Telcordia SR-332," *Energies*, vol. 17, p. 3957, Aug. 2024. Publisher: MDPI AG.

[24] D. Butnicu, "POL DC-DC Converter Output Capacitor Bank's Reliability Comparison using Prediction Standard MIL-HDBK-217F and SN 29500," in *2021 IEEE 27th International Symposium for Design and Technology in Electronic Packaging (SIITME)*, pp. 169–172, Oct. 2021. ISSN: 2642-7036.

[25] S. Peyghami, Z. Wang, and F. Blaabjerg, "A Guideline for Reliability Prediction in Power Electronic Converters," *IEEE Transactions on Power Electronics*, vol. 35, pp. 10958–10968, Oct. 2020.

[26] IEC, *Electric components - Reliability - Reference conditions for failure rates and stress models for conversion (IEC 61709:2017,IDT)*, 05 2017.

[27] IMdR, *FIDES Guide 2022 - Reliability Methodology for Electronic Systems*, 07 2023. Edition A.

[28] A. Gaonkar, R. B. Patil, D. Das, M. H. Azarian, B. Sood, and M. G. Pecht, "Assessment of the FIDES Guide 2022 electrical, electronic, and electromechanical reliability prediction methodology," *e-Prime - Advances in Electrical Engineering, Electronics and Energy*, vol. 6, p. 100353, Dec. 2023.

[29] Nexperia, "RC Thermal Models," Application Note AN11261, Nexperia B.V., Netherlands, May 2020. Rev. 4.0.

[30] Infineon Technologies AG, "Transient thermal measurements and thermal equivalent circuit models," Application Note AN2015-10, Infineon Technologies AG, April 2020. Version 1.2.

[31] M. Held, P. Jacob, G. Nicoletti, P. Scacco, and M.-H. Poech, "Fast power cycling test of IGBT modules in traction application," in *Proceedings of Second International Conference on Power Electronics and Drive Systems*, vol. 1, pp. 425–430 vol.1, May 1997.

[32] F. Kardan, A. Shekhar, and P. Bauer, "Quantitative Comparison of the Empirical Lifetime Models for Power Electronic Devices in EV Fast Charging Application," in *2023 11th International Conference on Power Electronics and ECCE Asia (ICPE 2023 - ECCE Asia)*, pp. 3239–3244, May 2023. ISSN: 2150-6086.

[33] J. Lutz, H. Schlangenotto, U. Scheuermann, and R. De Doncker, *Semiconductor Power Devices*. Cham: Springer International Publishing, 2018.

[34] T. Schutze, H. Berg, and M. Hierholzer, "Further improvements in the reliability of IGBT modules," in *Conference Record of 1998 IEEE Industry Applications Conference. Thirty-Third IAS Annual Meeting (Cat. No.98CH36242)*, vol. 2, pp. 1022–1025 vol.2, Oct. 1998. ISSN: 0197-2618.

[35] E. Deng, J. Chen, Y. Zhao, Z. Zhao, and Y. Huang, "Power Cycling Capability of High Power IGBT Modules for Flexible HVDC System," in *PCIM Europe digital days 2020; International Exhibition and Conference for Power Electronics, Intelligent Motion, Renewable Energy and Energy Management*, pp. 1–8, July 2020.

[36] C. Qian, A. M. Gheitaghy, J. Fan, H. Tang, B. Sun, H. Ye, and G. Zhang, "Thermal Management on IGBT Power Electronic Devices and Modules," *IEEE Access*, vol. 6, pp. 12868–12884, 2018. Conference Name: IEEE Access.

[37] M. Turzyński and P. Musznicki, "A Review of Reduction Methods of Impact of Common-Mode Voltage on Electric Drives," *Energies*, vol. 14, p. 4003, Jan. 2021. Publisher: Multidisciplinary Digital Publishing Institute.

[38] Bureau Veritas, *Rules for the classification of steel ships - part c - machinery, electricity, automation and fire protection*, Jan 2025.

[39] R. Alvarez, M. Wahle, H. Gambach, and J. Dorn, "Optimum semiconductor voltage level for MMC submodules in HVDC applications," in *2016 18th European Conference on Power Electronics and Applications (EPE'16 ECCE Europe)*, pp. 1–9, Sept. 2016.

[40] Mitsubishi Electric Corporation, "CM1200HC-66X: High Power Switching Use Insulated Type HVIGBT Module," 2022.

[41] Mitsubishi Electric Corporation, "RM1200DC-66X: High Power Switching Use Insulated Type High Voltage Diode Module," 2022.

[42] Infineon Technologies AG, "Fz1200r17he4p igbt module datasheet, version 3.0," Oct. 2016.

[43] MeccAL heatsinks, "Air cooled technologies," Okt. 2020.

[44] Advanced Thermal Solutions Inc., "Ats liquid cooling ebook," Jun. 2018.

[45] Advanced Thermal Solutions, Inc., "Ats-cp-1002 igbt cold plates high performance, r3," Apr. 2019.

[46] Siemens Digital Industries Software, "Rainflow counting." `https://community.sw.siemens.com/s/article/rainflow-counting`, Aug 2019.

[47] E08 Committee, "Practices for Cycle Counting in Fatigue Analysis."

[48] U. Scheuermann and M. Junghaenel, "Limitation of Power Module Lifetime Derived from Active Power Cycling Tests," in *CIPS 2018; 10th International Conference on Integrated Power Electronics Systems*, pp. 1–10, Mar. 2018.

[49] U. Scheuermann, R. Schmidt, and P. Newman, "Power cycling testing with different load pulse durations," in *7th IET International Conference on Power Electronics, Machines and Drives (PEMD 2014)*, pp. 1–6, Apr. 2014.

[50] J. Lutz, C. Schwabe, G. Zeng, and L. Hein, "Validity of power cycling lifetime models for modules and extension to low temperature swings," in *2020 22nd European Conference on Power Electronics and Applications (EPE'20 ECCE Europe)*, pp. P.1–P.9, Sept. 2020.

[51] M. Novak, A. Sangwongwanich, and F. Blaabjerg, "Monte Carlo-Based Reliability Estimation Methods for Power Devices in Power Electronics Systems," *IEEE Open Journal of Power Electronics*, vol. 2, pp. 523–534, 2021. Conference Name: IEEE Open Journal of Power Electronics.

[52] J. Xu, L. Wang, Y. Li, Z. Zhang, G. Wang, and C. Hong, "A unified mmc reliability evaluation based on physics-of-failure and sm lifetime correlation," *International Journal of Electrical Power & Energy Systems*, vol. 106, pp. 158–168, 2019.

[53] H. Rinne, *The Weibull Distribution: A Handbook*. Chapman and Hall/CRC, 1st ed., 2008.

[54] A. Abuelnaga, M. Narimani, and A. S. Bahman, "A Review on IGBT Module Failure Modes and Lifetime Testing," *IEEE Access*, vol. 9, pp. 9643–9663, 2021. Conference Name: IEEE Access.

[55] Anish, "General Overview of Central Cooling System on Ships," July 2019.

[56] Semikron Danfoss International, *Estimation of Liquid Cooled Heat Sink Performance at Different Operation Conditions*, Sep 2024. Rev. 1.2.

[57] K. Ma, N. He, M. Liserre, and F. Blaabjerg, "Frequency-Domain Thermal Modeling and Characterization of Power Semiconductor Devices," *IEEE Transactions on Power Electronics*, vol. 31, pp. 7183–7193, Oct 2016.

[58] IEC, *Electric vehicle conductive charging system – Part 23: DC electric vehicle supply equipment*, 12 2023. Rev. 1.

[59] B. Xu, A. Oudalov, A. Ulbig, and G. Andersson, "Modeling of Lithium-Ion Battery Degradation for Cell Life Assessment," *IEEE Transactions on Smart Grid*, vol. 99, pp. 1–1, June 2016.

Appendix A

Literature Review

A.1 Reliability

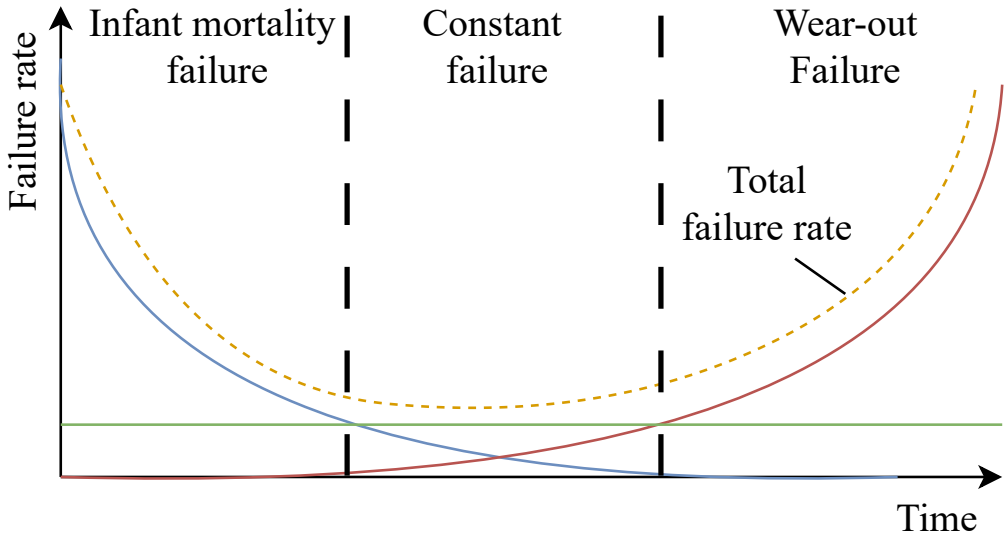

Figure A.1: Generic bathtub curve to represent the failure rate of three types of failures [5]

Table A.1: Failures types of semiconductor devices

Device	Failure type	Failure mode	Failure mechanisms	Critical stressors
Semiconductors [9] [19]	Catastrophic failures	Open circuit	Device failure in gate driver, Driver board short-, open-circuit	Overcurrent/voltage
			Bond wire lift-off, Bond wire rupture after IGBT short-circuit	Overcurrent
		Short circuit	High voltage breakdown	Overvoltage
			Dynamic latch-up	High dV/dt
			Second breakdown	Overcurrent
			Impact ionization	Overvoltage
			High temperature due to power dissipation	Overcurrent
	Wear-out failures	Parameter drift	Chip solder joint cracking	Thermal fluctuations
			Baseplate solder joints cracking	Thermal fluctuations
			Wire bonds lift-off/cracking	Thermal fluctuations

Table A.2: LESIT parameters [7]

A	α	$E_a(J)$	$k_B(J/K)$
$3.025 \cdot 10^5$	-5.039	$9.890 \cdot 10^{-20}$	$1.380 \cdot 10^{-23}$

Table A.3: CIPS parameters [8]

A	β_1	β_2	β_3	β_4	β_5	β_6
$9.3 \cdot 10^{14}$	-4.416	1285	-0.463	-0.716	-0.761	-0.5

Table A.4: Comparison of model parameters for lifetime estimation in [4]

Parameter	Normal model	Model 1	Model 2
A	$1.3824 \cdot 10^{11}$	$1.9164 \cdot 10^{13}$	$2.7583 \cdot 10^{19}$
β_1	-5.9236	-4.6222	-6.6559
β_2	4392.5	1037.8	N/A
β_3	-0.4939	-0.4341	N/A
β_4	-0.0305	-0.0087	-0.0076
β_5	1.2114	1.0371	-0.6557

Appendix B

SSCB model

B.1 Voltage clamping circuits

B.1.1 RC snubber

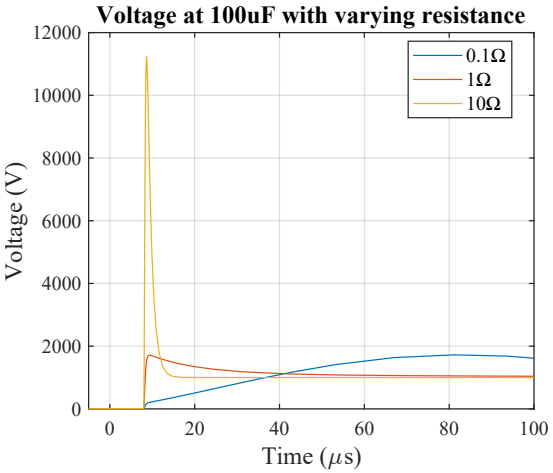

(a) Voltage over SSCB with 100uF and varying resistance

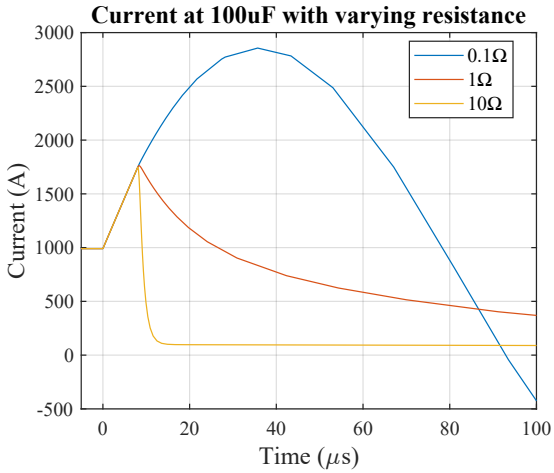

(b) Current over SSCB with 100uF and varying resistance

Figure B.1: Simulation results of SSCB voltage and current with an RC-snubber type voltage clamping circuit - variable resistance

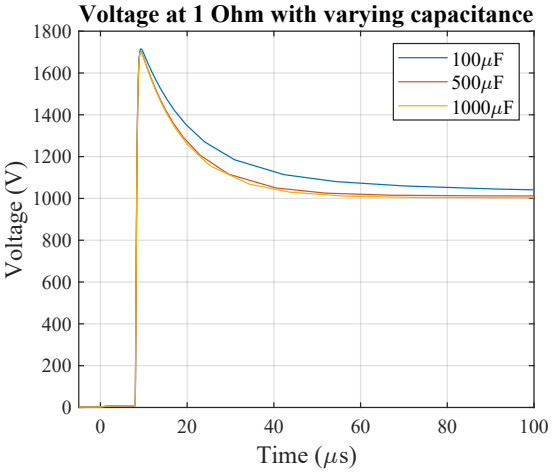

(a) Voltage over SSCB with 1 Ohm and varying capacitance

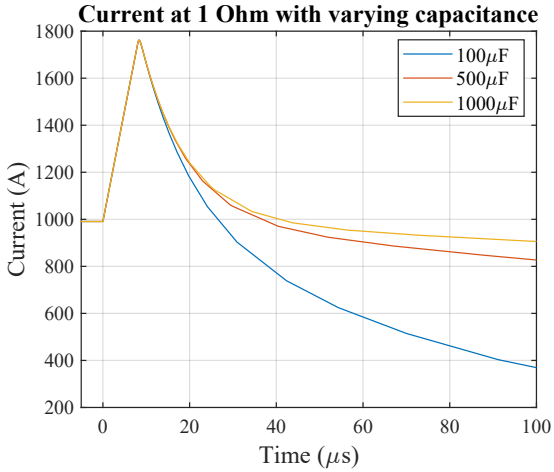

(b) Current over SSCB with 1 Ohm and varying capacitance

Figure B.2: Simulation results of SSCB voltage and current with an RC-snubber type voltage clamping circuit - variable capacitance

B.1.2 RCD snubber

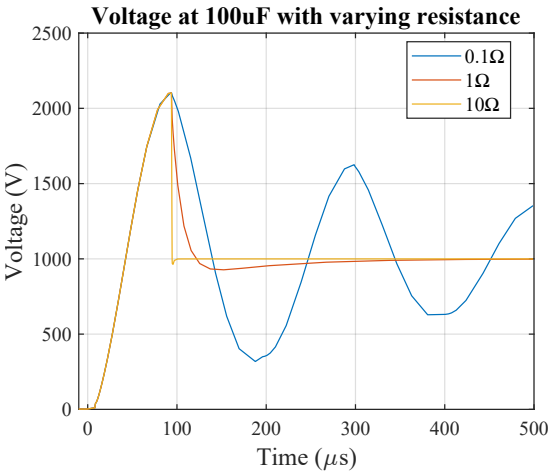

(a) Voltage over SSCB with 100uF and varying resistance

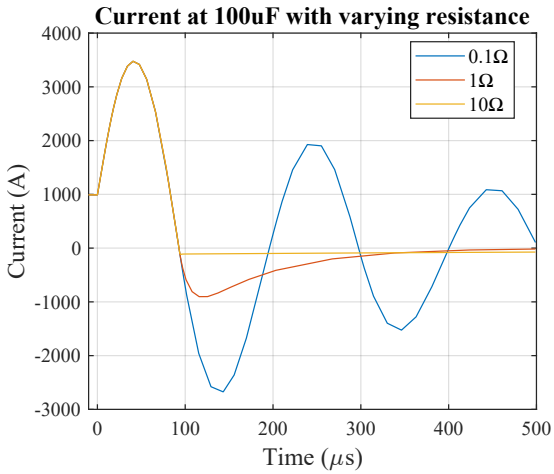

(b) Current over SSCB with 100uF and varying resistance

Figure B.3: Simulation results of SSCB voltage and current with an RCD-snubber type voltage clamping circuit - variable resistance

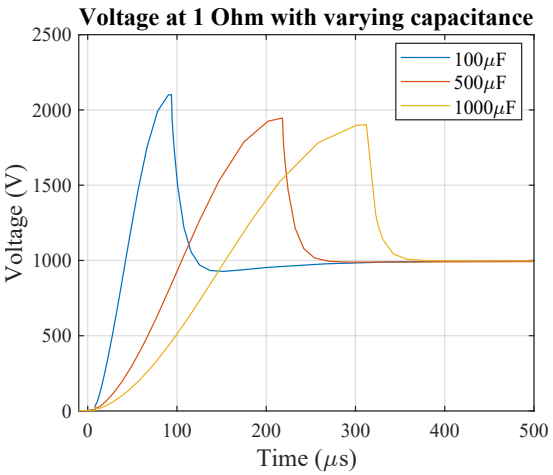

(a) Voltage over SSCB with 1 Ohm and varying capacitance

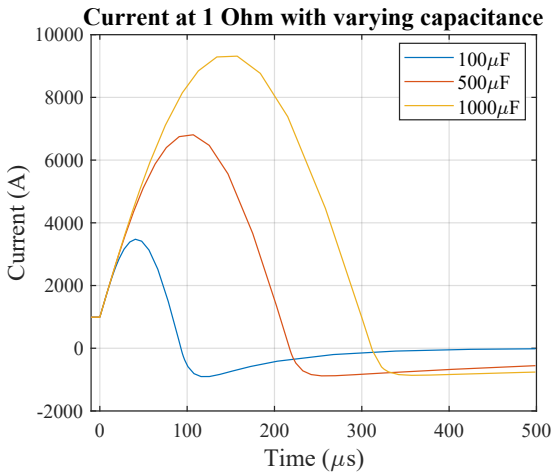

(b) Current over SSCB with 1 Ohm and varying capacitance

Figure B.4: Simulation results of SSCB voltage and current with an RCD-snubber type voltage clamping circuit - variable capacitance

B.2 Power loss

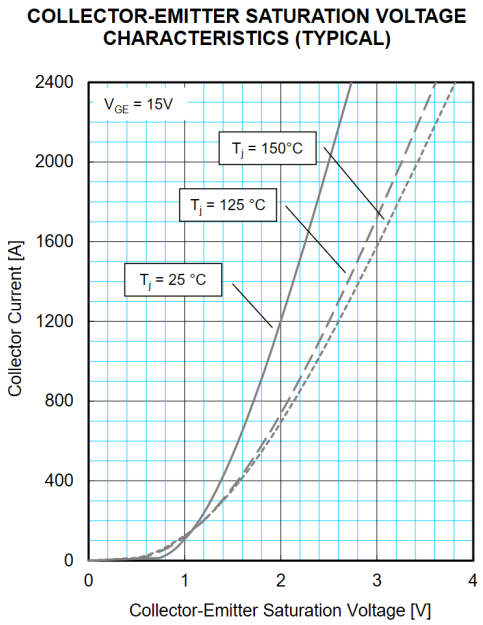

(a) V-I curve of CM1200HC-66X IGBT [40]

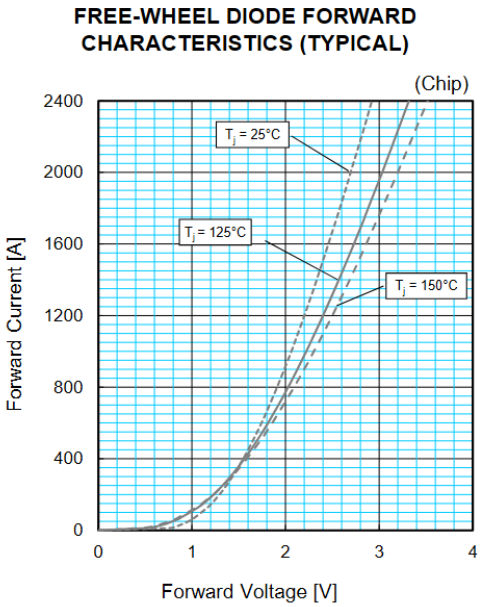

(b) V-I curve of RM1200DC-66X diode [41]

Figure B.5: V-I curves of the selected IGBT and diodes

Appendix C

Reliability model

C.1 Rainflow counting algorithm

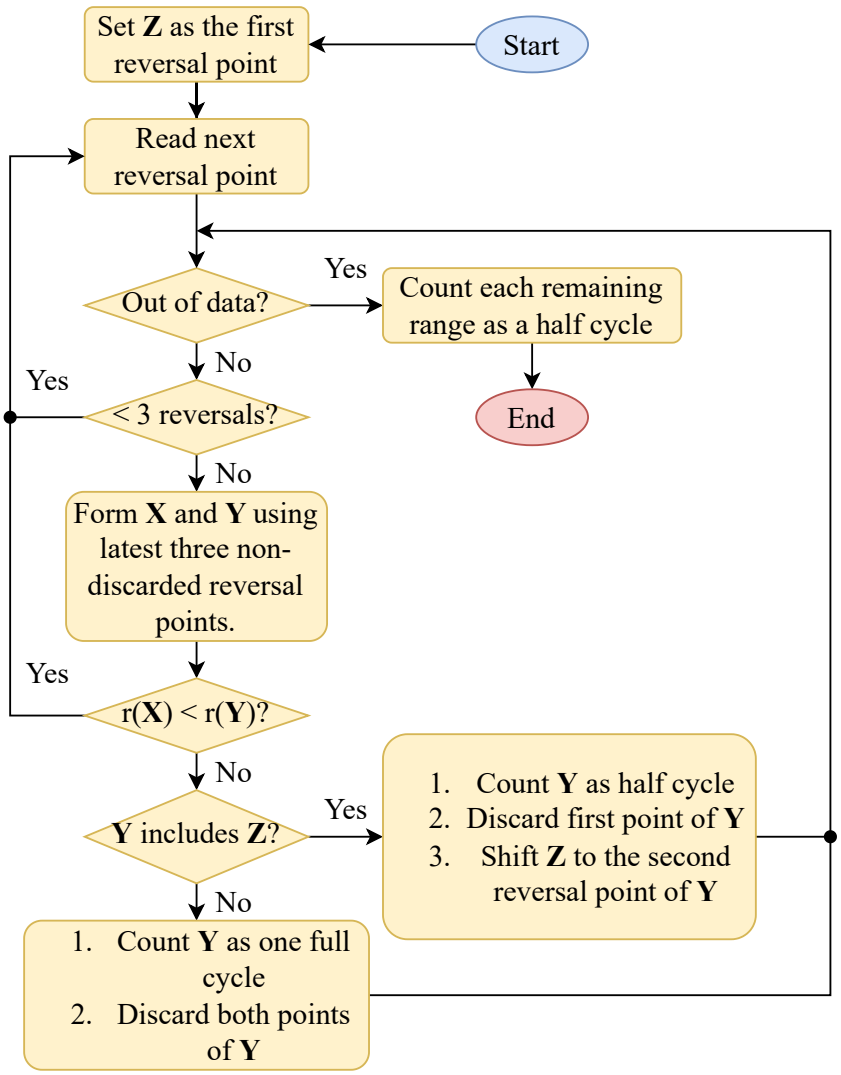

Figure C.1: Counting algorithm for the rainflow counting method in MATLAB as described by Mathworks [6]

C.2 Lifetime model validation

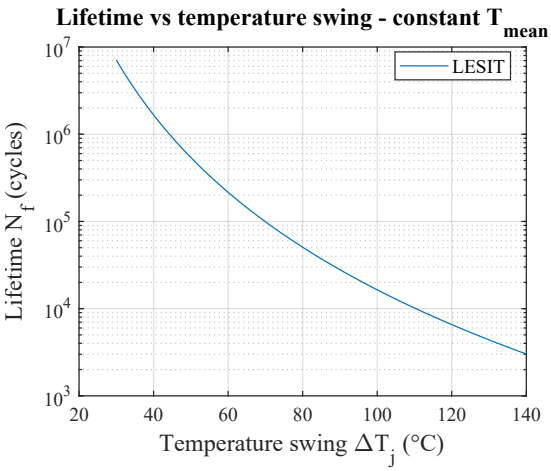

(a) LESIT output with a constant T_{mean} of $80°C$ [7] [31].

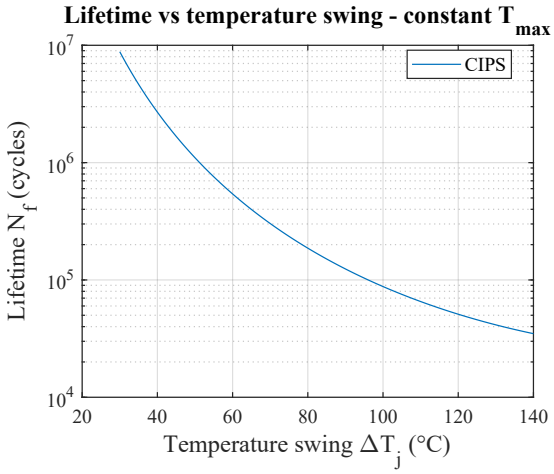

(b) CIPS output with $T_{\text{max}} = 150°C$, $t_{\text{on}} = 1.5s$, $V_{class} = 12V$, $I = 10A$, $D = 400\,\mu m$ [8].

Figure C.2: Output of the lifetime models in MATLAB with the lifetime parameters given from their related papers.

C.3 Beta values distribution

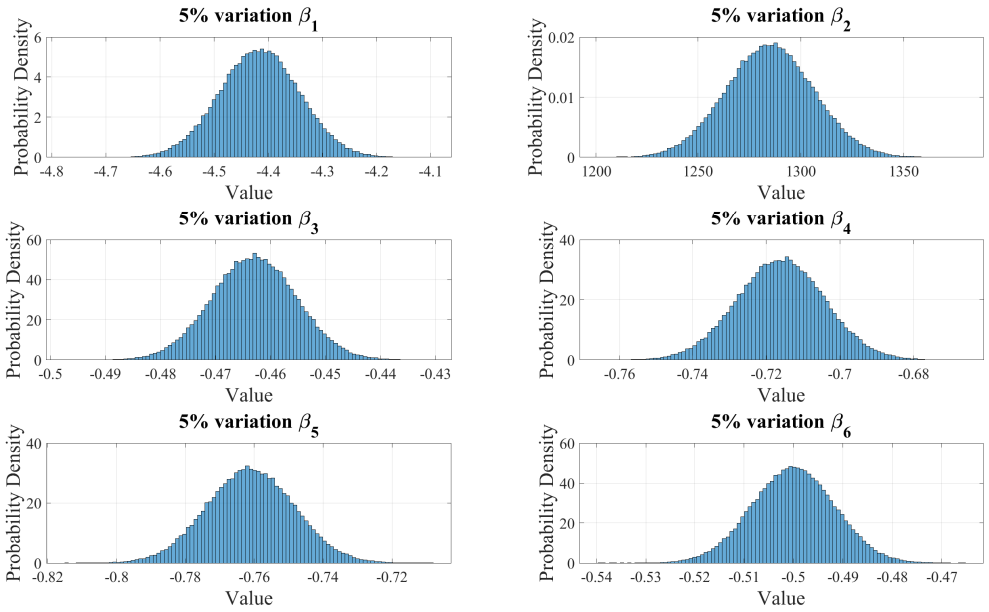

Figure C.3: Beta values following normal distribution with a standard deviation σ of $\frac{0.05}{3}$

Appendix D

Noise model

D.1 Power loss - effect of junction temperature

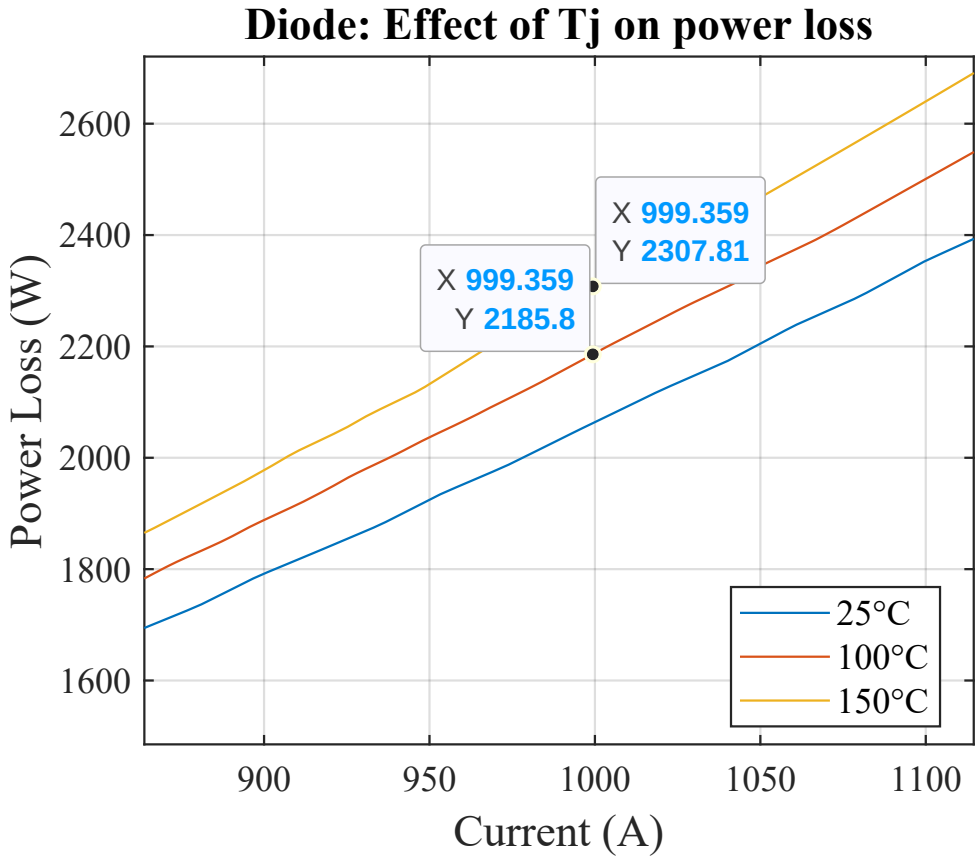

Figure D.1: Zoomed in plot of power loss in the diode as a consequence of difference in junction temperature.

D.2 Impact frequency on ΔT_j - Charging

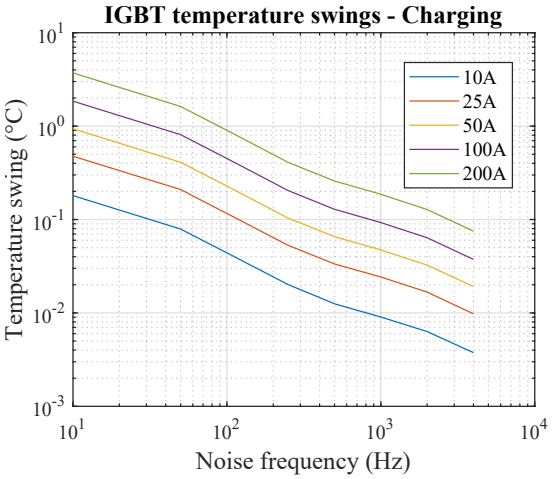

(a) IGBT temperature swings as a function of noise frequency.

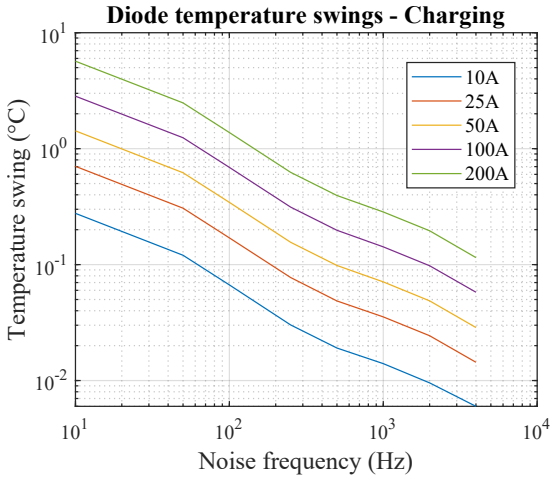

(b) Diode temperature swings as a function of noise frequency.

Figure D.2: Component junction temperature swings as a function of noise frequency during the charging period for noise current amplitudes of 10 A, 25 A, 50 A, 100 A, 200 A.

D.3 Impact frequency on ΔT_j - Sailing

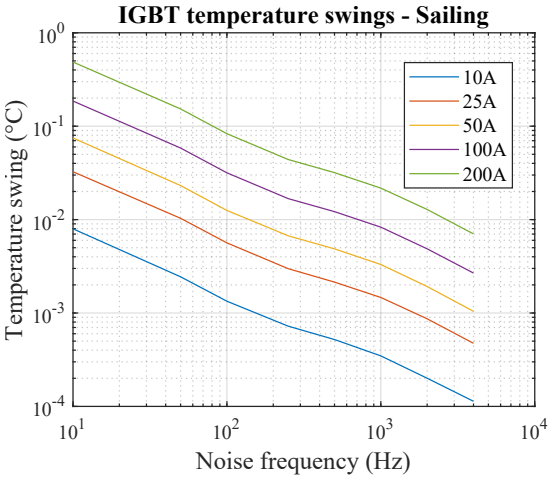

(a) IGBT temperature swings as a function of noise frequency.

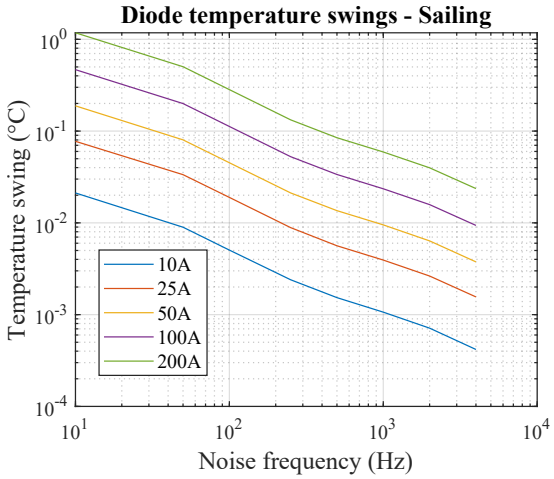

(b) Diode temperature swings as a function of noise frequency.

Figure D.3: Component junction temperature swings as a function of noise frequency during the sailing period for noise current amplitudes of 10 A, 25 A, 50 A, 100 A, 200 A.